

AFIT/GE/ENG/95D-06

VELOCITY DETERMINATION
FOR AN INVERTED PSEUDOLITE
NAVIGATION REFERENCE SYSTEM

THESIS
Jeffrey M. Hebert
Captain, USAF

AFIT/GE/ENG/95D-06

19960327 035

Approved for public release; distribution unlimited

The views expressed in this thesis are those of the author and do not reflect the official policy or position of the Department of Defense or the U. S. Government.

AFIT/GE/ENG/95D-06

VELOCITY DETERMINATION FOR AN INVERTED PSEUDOLITE
NAVIGATION REFERENCE SYSTEM

THESIS

Presented to the Faculty of the School of Engineering
of the Air Force Institute of Technology

Air University

In Partial Fulfillment of the
Requirements for the Degree of
Master of Science in Electrical Engineering

Jeffrey M. Hebert, B.S. (Electrical Engineering)

Captain, USAF

December, 1995

Approved for public release; distribution unlimited

Acknowledgements

While this thesis has only one author, the work of many people made it possible. I am indebted to my classmates in the Guidance and Control section of class GE-95D. Thank you all, for everything.

I would like to thank my committee members for their help in this thesis effort. I would especially like to thank LtCol Bob Riggins, my advisor, for his support and enthusiasm throughout this project. Also, thanks to Mr. Donald Smith who kept the computers running in spite of the users' attempts otherwise. I would like to thank Mr. Stan Musick of Wright Laboratory's Avionics Directorate for his help with the PROFGEN software package.

This thesis is sponsored by the 746th Test Squadron, Holloman AFB, NM. Many thanks go out to Capt. John Raquet, Capt. Tony Nash and Lt. Brian Bohenek who provided me with this topic and answered my many questions.

Finally I would like to thank my wife, Cathy, for her love and support during these long months at AFIT.

Jeffrey M. Hebert

Table of Contents

	Page
Acknowledgements	ii
List of Figures	vii
List of Tables	ix
List of Abbreviations	xi
Abstract	xii
I. Introduction	1-1
1.1 Background	1-1
1.2 Problem	1-3
1.3 Summary of Current Knowledge	1-4
1.3.1 Terminology	1-4
1.3.2 Literature Review	1-5
1.3.3 Concept of Operation	1-6
1.4 Assumptions	1-7
1.5 Scope	1-8
1.6 Approach/Methodology	1-9
1.6.1 Digital Filtering with Numeric Differentiation	1-9
1.6.2 Kalman Filtering	1-9
1.7 Materials, Data and Equipment	1-11
1.7.1 Simulation Software	1-11
1.8 Overview of Thesis	1-12

	Page
II. Theory	2-1
2.1 Overview	2-1
2.2 Approximating Velocity	2-1
2.2.1 Taylor's Series Approximation to the Derivative . .	2-1
2.2.2 Extrapolating the Central Difference Approximation	2-2
2.2.3 Error Analysis of the Velocity Approximation	2-3
2.3 Global Positioning System Measurements	2-5
2.3.1 Pseudorange	2-5
2.3.2 Carrier-Phase	2-7
2.3.3 Deltarange	2-9
2.4 Kalman Filtering/Smoothing	2-12
2.5 Digital Filtering	2-15
2.5.1 FIR Filter	2-15
2.5.2 IIR Filter	2-16
2.6 Summary	2-17
III. Models	3-1
3.1 Overview	3-1
3.2 Kinematic Models	3-1
3.2.1 Constant Velocity	3-2
3.2.2 Constant Acceleration	3-4
3.2.3 Constant Acceleration, Noise 1st Order Gauss-Markov	3-5
3.3 Noise Models	3-6
3.3.1 Tropospheric Delay	3-7
3.3.2 Receiver Noise and Multipath Error	3-8
3.3.3 Noise Model Implementation	3-9
3.4 Digital Filter Design	3-11

	Page
IV. Results	4-1
4.1 Overview	4-1
4.2 Aircraft Trajectory	4-1
4.3 Digital Filtering with Numeric Differentiation	4-7
4.3.1 Analysis of Sampling Rates for Alias Effects	4-8
4.3.2 Numerical Differentiation Algorithm Performance . .	4-10
4.3.3 Digital Filter Results	4-17
4.3.4 Post-Filter Design	4-19
4.3.5 Overall Results	4-20
4.4 Kalman Filtering/Smoothing	4-21
4.4.1 Constant Velocity Model	4-22
4.4.2 Constant Acceleration Model	4-22
4.4.3 Constant Acceleration with Markov Process Model .	4-24
4.5 Summary	4-25
V. Conclusions and Recommendations	5-1
5.1 Overview	5-1
5.2 Conclusions	5-1
5.2.1 Digital Filtering and Numerical Methods	5-1
5.2.2 Kalman Filtering/Smoothing	5-2
5.3 Recommendations	5-3
5.3.1 Receiver Geometry	5-3
5.3.2 Flight Profiles	5-4
5.3.3 Error Modeling	5-4
5.3.4 Adaptive Kalman Filtering	5-4
Appendix A. Calculation of RMS Error	A-1
Appendix B. Constant Velocity Kalman Filter Results	B-1

	Page
Appendix C. Constant Acceleration Kalman Filter Results	C-1
Appendix D. Constant Acceleration, 1st Order Markov Kalman Filter Results	D-1
Bibliography	BIB-1
Vita	VITA-1

List of Figures

Figure	Page
1.1. Concept of Operation	1-7
1.2. Typical NRS Error-State Model Formulation	1-10
2.1. Illustration of Between Receivers/Pseudolites Double Difference	2-9
2.2. Structure of FIR Filter	2-16
2.3. Structure of IIR Filter (Canonic Form)	2-17
3.1. Location of Troposphere and Stratosphere	3-7
3.2. Multipath Signal Reflection	3-9
3.3. Block Diagram of Noise Model	3-10
3.4. Parameters for Filter Design	3-12
4.1. 2-D View of Flight Profile	4-1
4.2. Time History of "Gees"	4-2
4.3. 3-D View of Flight Profile	4-2
4.4. Top View of Flight Profile and Receiver Locations	4-3
4.5. Range and Elevation Angles Between Aircraft and Receivers	4-4
4.6. GDOP for Entire Flight Profile with Given Receiver Locations	4-6
4.7. Plan View of Flight Profile and GDOP for Truncated Flight Segment	4-6
4.8. Plan View of Receiver Locations Ensuring $GDOP < 10$	4-7
4.9. GDOP for Entire Flight Profile Using Receiver Locations in Figure 4.8	4-8
4.10. Frequency Spectra for Highly Dynamic Flight Trajectory at 1000 Hz	4-9
4.11. Frequency Spectra for Highly Dynamic Flight Trajectory at 10 Hz	4-9
4.12. Error in Central Difference Approximations in the Absence of Noise	4-11
4.13. Error in 3rd Order Numerical Derivative Using Flight Profile at 10 Hz	4-13
4.14. Error in Cubic Spline Derivative in the Absence of Noise	4-15

Figure	Page
4.15. Error in Cubic Spline Derivative Using Flight Profile at 10 Hz	4-16
4.16. Overall Block Diagram for Digital Filtering Approach	4-20
4.17. X, Y, and, Z Velocities for Benign Flight Trajectory	4-21
 B.1. Colored Noise at 1 Hz, Proper Model	 B-2
B.2. White Noise at 1 Hz, Proper Model	B-3
B.3. Colored Noise at 10 Hz, Proper Model	B-4
B.4. White Noise at 10 Hz, Proper Model	B-5
B.5. Colored Noise at 1 Hz, Improper Model	B-6
B.6. White Noise at 1 Hz, Improper Model	B-7
B.7. Colored Noise at 10 Hz, Improper Model	B-8
B.8. White Noise at 10 Hz, Improper Model	B-9
 C.1. Colored Noise at 1 Hz, Proper Model	 C-2
C.2. White Noise at 1 Hz, Proper Model	C-3
C.3. Colored Noise at 10 Hz, Proper Model	C-4
C.4. White Noise at 10 Hz, Proper Model	C-5
C.5. Colored Noise at 1 Hz, Improper Model	C-6
C.6. White Noise at 1 Hz, Improper Model	C-7
C.7. Colored Noise at 10 Hz, Improper Model	C-8
C.8. White Noise at 10 Hz, Improper Model	C-9
 D.1. Colored Noise at 1 Hz, Proper Model	 D-2
D.2. White Noise at 1 Hz, Proper Model	D-3
D.3. Colored Noise at 10 Hz, Proper Model	D-4
D.4. White Noise at 10 Hz, Proper Model	D-5
D.5. Colored Noise at 1 Hz, Improper Model	D-6
D.6. White Noise at 1 Hz, Improper Model	D-7
D.7. Colored Noise at 10 Hz, Improper Model	D-8
D.8. White Noise at 10 Hz, Improper Model	D-9

List of Tables

Table	Page
1.1. Comparison of Modern Navigation Reference Systems	1-2
4.1. Pseudolite Receiver Locations for NRS Simulation	4-3
4.2. Performance of Numeric Differentiators Using Flight Profile	4-12
4.3. Performance of Numeric Differentiators Using Benign Flight Profile	4-13
4.4. Performance of Numeric Differentiators in the Presence of Noise Using Benign Flight Profile	4-14
4.5. Performance of Cubic Spline Differentiator in the Absence of Noise	4-16
4.6. Performance of Cubic Smoothing Spline Differentiators in the Presence of Noise Using Benign Flight Profile	4-17
4.7. IIR Filter Design Parameters and Resulting Filter Order	4-18
4.8. Performance of IIR Filters in the Absence of Noise	4-18
4.9. Performance of IIR Filters in the Presence of Noise	4-19
4.10. FIR Filter Design Parameters and Resulting Filter Order	4-19
4.11. IIR Post-Filter Design Parameters and Resulting Filter Order	4-20
4.12. Overall Performance in the Presence of Noise Using Benign Flight Profile	4-20
4.13. Constant Velocity Model Using Truncated Flight Profile	4-22
4.14. Constant Velocity Model Using Entire Benign Flight Profile	4-23
4.15. Constant Acceleration Model Using Truncated Flight Profile	4-23
4.16. Constant Acceleration Model Using Entire Flight Profile	4-23
4.17. Constant Acceleration Model with Markov Process Using Truncated Flight Profile	4-24
4.18. Constant Acceleration Model with Markov Process Using Entire Flight Profile	4-24
B.1. Legend for Filter Tuning Plots	B-1

Table	Page
C.1. Legend for Filter Tuning Plots	C-1
D.1. Legend for Filter Tuning Plots	D-1

List of Abbreviations

Abbreviation	Page
CIGTF Central Inertial Guidance Test Facility	1-1
NRS Navigation Reference System	1-1
INS Inertial Navigation System	1-1
CIRIS Completely Integrated Reference Instrumentation System	1-1
RRS Range/Range-Rate System	1-1
GPS Global Positioning System	1-1
CHAPS CIGTF High Accuracy Post-Processing Reference System	1-1
CEP Circular Error Probable	1-2
RMS Root Mean Square	1-2
SARS Sub-meter Accuracy Reference System	1-2
ECEF Earth Centered Earth Fixed	2-1
SA Selective Availability	3-6
GDOP Geometric Dilution of Precision	4-4

Abstract

As navigation systems continue to improve in performance and features, the Air Force must develop better Navigation Reference Systems (NRS) to keep pace with technology. Specifically, with the advent of enhanced, integrated Global Positioning System (GPS) and Inertial Navigation System (INS) navigators, emphasis is placed on the measuring performance in the presence of GPS jamming. To meet these needs, a new NRS, dubbed the Sub-Meter Accuracy Reference System (SARS), is being developed by the 746th Test Squadron, Holloman AFB, New Mexico. SARS uses a unique, inverted GPS pseudolite positioning system to determine a reference trajectory. This research investigates two post-processing methods of determining velocity from a discrete position data at a constant data rate. The first method employs numerical differentiation along with digital filters to provide noise reduction. The second method uses kinematic model-based Kalman filtering and smoothing to determine the reference velocity.

VELOCITY DETERMINATION FOR AN INVERTED PSEUDOLITE NAVIGATION REFERENCE SYSTEM

I. Introduction

1.1 Background

The 746th Guidance Test Squadron, Holloman AFB, NM, is the principal test organization for developmental testing of military aircraft navigation systems [39]. As part of the 746th, the Central Inertial Guidance Test Facility (CIGTF) maintains a Navigation Reference System (NRS) used in the test and evaluation of navigation systems.

From 1965 to the present, many different technologies have been used in the development of an NRS. These include radar tracking, high-precision ground-based camera tracking and the development of an aircraft transponder/ground receiver system. In 1975, with the advent of microprocessor technology, advances in mathematics (Kalman filtering) and Inertial Navigation Systems (INS), the "modern-era" NRS was conceived. The Completely Integrated Reference Instrumentation System (CIRIS) combined an INS, barometric altimeter and a Range/Range-Rate System (RRS) of ground transponder/interrogators. Over the years, CIRIS was updated with new inertial navigators as well as Global Positioning System (GPS) receivers. These upgrades continually improved the overall accuracy of the system.

In 1993, development began on a replacement for CIRIS called the CIGTF High Accuracy Post-Processing Reference System (CHAPS). CHAPS combined an INS, Differential GPS and the RRS transponder measurements in a Kalman filter, in a manner similar to CIRIS. CHAPS, however, had to be significantly more accurate than CIRIS in order to effectively test GPS systems, inertial systems and GPS-aided inertial navigation systems. As an NRS, CHAPS has shown performance in position accuracy of 1.2 *m* and velocity accuracy of 0.03 *m/s* [39]. In early 1995, an upgraded version of CHAPS, called CHAPS II, began validation testing at CIGTF. CHAPS II is a more compact version of CHAPS with an enhanced GPS receiver capable of carrier-phase positioning.

To be an effective reference, the NRS must demonstrate an accuracy at least one order of magnitude better than the system under test [2]. Advances in navigation technology have made maintaining the accuracy advantage of the NRS difficult. Today, technology continues to improve the accuracy of navigation systems. Embedded GPS/INS systems, designed for enhanced performance in routine flight, high dynamics, antenna shaded and jamming environments, are coming to market. One such system, the Honeywell H-764G, has demonstrated position accuracy of 0.8 *nmi/hr* circular error probable (CEP) and velocity accuracy of 0.06 *m/s* root mean square (RMS), using P-code GPS [12]. While a pre-production version of the H-764G has been evaluated at CIGTF [30], the increased position and velocity accuracy of such systems, along with claimed anti-jamming capabilities necessitates a performance enhancement of the current NRS, CHAPS. A comparison of recent reference systems developed at CIGTF is given in Table 1.1. A summary of earlier reference system development can be found in [41].

Table 1.1 Comparison of Modern Navigation Reference Systems

Reference System	Measurements	Position Accuracy	Velocity Accuracy
CIRIS [41]	INS RRS GPS	4.0 <i>m</i>	0.03 <i>m/s</i>
CHAPS [36]	INS RRS Differential GPS	1.2 <i>m</i>	0.03 <i>m/s</i>
CHAPS II [36]	INS RRS Carrier-Phase GPS	0.1 <i>m</i>	0.03 <i>m/s</i>
SARS	Pseudolites	0.1 <i>m</i>	0.005 <i>m/s</i> ¹
Holloman High Speed Test Track [36]	Instrumented track	0.0008 <i>m</i>	0.0004 <i>m/s</i>

To meet the requirements for the NRS, CIGTF is developing a Sub-meter Accuracy Reference System (SARS). SARS is being designed for accuracies on the order of 0.1 *m* in position, and 0.005 *m/s* in velocity [13]. SARS is expected to operate in the most dynamic environments experienced by manned fighter aircraft, up to 9 *gees* and 10 *m/s*³

¹Desired accuracies.

jerk. CHAPS, on the other-hand, was designed to fly on cargo or large bomber aircraft [39]. CHAPS II, while one-half the size of CHAPS, is unable to fly aboard operational fighter aircraft due to it's size. Additionally, SARS intends to operate without degradation under narrow-band GPS jamming conditions.

To accomplish these objectives, SARS departs radically from the NRS designs of CIRIS and CHAPS². SARS will depend solely on GPS-style measurements derived from the carrier-phase observable [34]. Instead of using GPS receivers on-board the aircraft, the aircraft will be fitted with a GPS pseudolite transmitter, which is explained in Section 1.3.3. This dramatically decreases the power and space requirements of the reference system aboard the test aircraft, allowing for a broader range of aircraft to be tested. Furthermore, the use of customizable GPS pseudolites allows the user to change the carrier frequency of the transmitters. This may allow testing under narrow-band GPS jamming conditions, without adversely effecting the reference system.

1.2 Problem

In previous NRS designs, an error-state Kalman filter combines the available measurements from navigation aids such as GPS, to estimate INS errors. The INS measures specific force. Acceleration of the aircraft is obtained by subtracting the gravity component from measured specific force. Integrating once yields velocity; integrating twice yields position. SARS, on the other-hand, will obtain position information from GPS data only, via the GPS observation equations. One might approximate velocity by numerical differentiation, however at the expense that noise present in the position measurements is amplified by the differentiation procedure.

In this effort we will compare two different approaches to determining the velocity of an aircraft along a trajectory given GPS measurements of position. The first approach uses a combination of digital filtering techniques and numerical methods. The second approach uses simple kinematic models in a Kalman filter to provide estimates of velocity. We will compare the performance of these two methods against the desired performance

²Conceptually, the SARS design is similar to the transponder portion of the RRS, which is part of CHAPS and CIRIS. The RRS was originally developed for CIGTF by the Cubic Corporation, in 1973 [41].

specification of 0.005 m/s and determine the sensitivity of each algorithm to different parameters such as measurement rates and noise characteristics. A simulated environment will be used for this research.

1.3 Summary of Current Knowledge

1.3.1 Terminology. Due to redundant and sometimes inconsistent terms found in the open literature, it is necessary to untangle the terminology used in discussing GPS measurements.³ Three “raw” measurements are obtainable in high performance GPS receivers: pseudorange, deltarange and the carrier-phase observable. Pseudorange, also known as the code phase observable, is the traditional GPS measurement used to determine position. Using a code correlation technique, pseudorange is a measure of the time of transmission between the GPS satellite and receiver, expressed in terms of distance. A minimum of four unique pseudorange measurements are required to compute a 3-D solution for user position and time.

The carrier-phase observable is also employed to determine position. Carrier-phase is a measurement of the number of integer and fractional cycles of the GPS carrier signal between the transmitter and receiver, expressed in terms of distance. Using carrier-phase to resolve position with centimeter accuracy was first developed for static applications, such as surveying. Recently, the ability to resolve the carrier-phase ambiguity problem in real-time has been demonstrated [14, 18, 19], leading the way for the use of carrier-phase in dynamic environments.

Deltarange, also known as Doppler, differs from pseudorange and carrier-phase, as it is a measure of range-rate rather than position. Deltarange approximates the true line-of-sight range-rate between a GPS satellite and receiver. Deltarange is formed in the receiver when cycles of the carrier-phase are counted over a small time interval divided by that time interval. This time interval is receiver dependent, typically kept small compared to the measurement output rate. For the Ashtech P-XII GPS receiver, deltarange is calculated over a 1 millisecond interval, while the measurements are available four times

³For further reference on GPS measurements and applications see [10, 19].

every second [19]. Since carrier-phase and deltarange measurements are observations of the same signal, they are highly correlated.

Occasionally, one sees another approximation to range-rate, called pseudo-deltarange or pseudorange deltarange. Unlike deltarange, pseudo-deltarange is not a measurement available from a GPS receiver. Instead, pseudo-deltarange is formed by subtracting successive pseudoranges and dividing over the time interval. Time intervals of pseudo-deltarange calculations are typically on the order of 1 second. Because pseudo-deltarange uses such a long time interval in differentiating position information into velocity, the approximation to range-rate becomes erroneous. This problem can be exacerbated in the case of high dynamics, when the time constant of the dynamics falls close to or below the Nyquist rate. Since the deltarange measurement comes from the receiver's carrier loop, it is independent of the pseudorange measurement, which comes from the code loop. Pseudo-deltarange, however, is clearly correlated with pseudorange measurements.

1.3.2 Literature Review. Many sources of information were drawn upon in the preparation of this research including numerous papers from the open literature, thesis reports, textbooks, course notes and personal interviews. While not all of the sources are referenced in this work, the referenced sources in this section and throughout the work provide an excellent background for further studies in this area.

As of this writing, the only paper in the open literature describing the concept of SARS is by Raquet, et al [36]. This paper also presents the results of an initial test of a prototype system conducted at Holloman AFB, N.M. Their results demonstrated the feasibility of the SARS concept in determining an accurate position solution. While SARS is unique in its inverted pseudolite mode of operation, there are other trajectory determination systems that use GPS methods (carrier-phase and differential C/A code) for kinematic positioning. These are described by Tang, et al, [44], Mahmood and Simpson [21], Dougherty, et al [8], Robbins [37] and Galijan and Gilkey [9].

The GPS system has its own measure of velocity (deltarange), as discussed earlier. One of the first papers to quantify GPS velocity accuracy was by McGowan [28]. May, et al, [23] describe the properties of GPS velocity accuracy as well as applications using GPS

to determine velocities. Methods and general guidance for proper treatment of deltarange measurement in a positioning system are given in Bach, et al [1] and Brown and McBurney [3].

The previous CIGTF-sponsored thesis work of Bohenek [2], Hansen [11], Mosle [29], Negast [35], Solomon [41], Snodgrass [40], Stacey [43] and Vasquez [47], provide great insight into the characterization and development of an NRS, as well as the background theory on inertial navigation systems, error-state extended Kalman filters, GPS, differential GPS and carrier-phase GPS. Also of interest, Tobin [46], Chang [5], Schwartz [42] and Roecker [38] address issues concerning adaptive Kalman filtering and target tracking.

1.3.3 Concept of Operation. As stated previously, the design of SARS departs radically from its modern predecessors, CHAPS and CIRIS. Unlike these reference systems, SARS does not use an INS. Nor will SARS require aircraft to carry a large payload of sensors and measuring devices. Instead, the sensors and measuring devices will be located on the ground, in the form of movable, self-surveying GPS receivers. Before a flight test, engineers will be able to lay out the desired locations of the receivers along the range, ensuring adequate receiver geometry and coverage during the flight.

The aircraft will be outfitted with a lightweight, low power GPS pseudolite, designed to be mounted on aircraft hard-points. An additional GPS pseudolite will broadcast from a known position on a mountain-top, within view of the ground receivers. This additional pseudolite will be used to perform a between receiver/pseudolite double difference of the carrier-phase measurement. This double differencing method eliminates the receiver and pseudolite clock bias as well as reduces errors due to tropospheric delay. While the theory of this unique carrier-phase differencing technique is still under development [36], this thesis work assumes that the carrier-phase measurements will yield a position solution with an accuracy of $0.1\text{ m } 1\sigma$ 3-D RMS. The general concept of operation is depicted in Figure 1.1.

After a flight test, carrier-phase position data will be collected from all receivers. This data will be processed to resolve the receiver clock bias, carrier-phase ambiguities and cycle slips. In general, a cycle slip is caused by a loss of lock of the carrier signal between the GPS transmitter and receiver. Cycle slips may be caused by an obstruction,

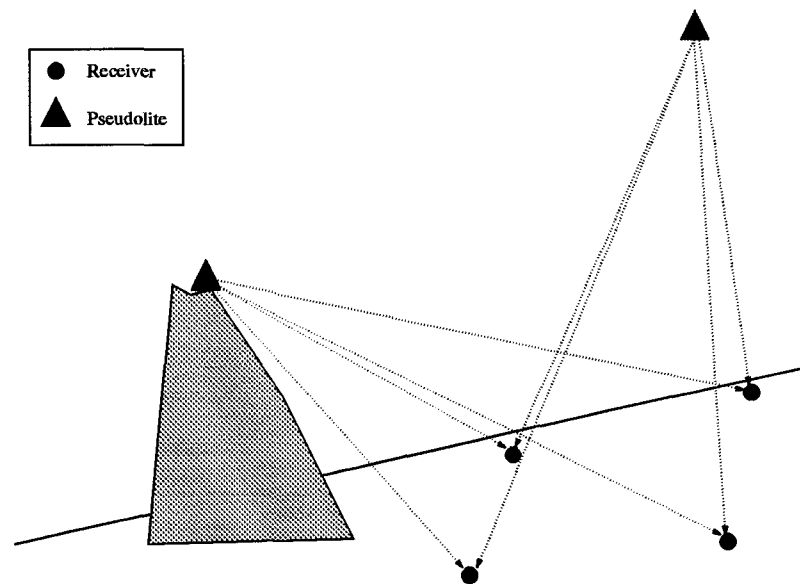


Figure 1.1 Concept of Operation

intense ionospheric activity or receiver power problems [19]. Since SARS is limited to use in the troposphere, no cycle slips due to ionospheric activity are anticipated.

Cycle slips essentially corrupt the future time-history of the carrier-phase ambiguity term. In dynamic applications, cycle slips are more difficult to predict due to the additional Doppler shift created by the aircraft's motion [19]. Previous AFIT thesis work [2,11,29,47], has addressed the problem of detecting and correcting for cycle slips in highly dynamic environments. For this effort it is assumed that the carrier-phase processing will correct the position solution for any cycle slips.

1.4 Assumptions

This section lists the assumptions used in this thesis research. These assumptions are defined to aid the reader in making a proper evaluation of this effort.

1. It is assumed that the carrier-phase data has been processed to remove ambiguities and cycle slips. It is assumed that the relevant residual carrier-phase errors include receiver noise, tropospheric delay and multipath.

2. It is assumed that the processed carrier-phase solution for position is expected to yield errors of $0.1\text{ m } 1\sigma$ 3-D RMS. This position error is assumed to include the error due to imprecise knowledge of the receiver and transmitter (stationary pseudolite) locations.
3. It is assumed that the maximum measurement rate of the GPS/pseudolite receivers to be used for SARS is 10 Hz.
4. It is assumed differentially-corrected C/A-code pseudorange and deltarange measurements are available.
5. It is assumed that all GPS/pseudolite receivers are perfectly synchronized in time and that all measurements are available simultaneously.
6. Flight trajectories will contain a range of dynamic conditions with profiles not exceeding 9 *gees* and 10 m/s^3 jerk. These profiles are assumed to be representative of the dynamic environment of modern fighter aircraft.
7. The flight profiles used in this thesis effort will come from PROFGEN [32]. MATLAB [27] will be used for simulation, data reduction and visualization. Explanations of these software tools can be found in Section 1.7.1.
8. Any Monte Carlo analyses to be conducted will be the results of 50-run simulations. Although a larger number of Monte Carlo runs would produce sample statistics that more closely reflect the true underlying error statistics, with statistical error asymptotically approaching zero as the number of runs approaches infinity, fifty was decided upon to keep the total computation time within reasonable limits.

1.5 Scope

The models developed in this effort are based upon information obtained from the open literature and from sources given by the sponsor, CIGTF. The velocity algorithm target specification is $0.005\text{ m/s } 1\sigma$ 3-D RMS, at a measurement rate no greater than 10 Hz. Several different filtering techniques will be considered in simulation, and recommendations made concerning the feasibility of a real world implementation of these techniques.

1.6 Approach/Methodology

Overall, two distinct approaches to the problem will be investigated. One method involves the use of digital filters and numerical methods techniques to evaluate velocity as the derivative of discrete, noisy position information. The second technique uses the structure of the Kalman filter to estimate velocity given a simple kinematic model and GPS measurements of position and velocity.

1.6.1 Digital Filtering with Numeric Differentiation. The digital filtering with numeric differentiation effort is a straight-forward approach to the problem. Given noise corrupted, discrete position measurements, a numerical derivative is computed. Two techniques for implementing a numerical derivative are explored. First, a standard central difference approximation to the derivative is derived from a Taylor's series expansion. Second, a curve fitting algorithm based upon cubic splines is employed to fit a curve to the noise corrupted position data. An analytical derivative of the fitted curve will be evaluated to determine velocity. The performance of the two techniques will be compared. Furthermore, digital filtering methods, in the form of low pass filters, are used for noise reduction both before and after the derivative operation.

1.6.2 Kalman Filtering. The Kalman filtering effort will devise an algorithm for velocity determination for two different measurement strategies. The first involves using carrier-phase data that has been processed to remove ambiguities and the effects of cycle slips. The second strategy involves combining unprocessed pseudorange and deltarange measurements to determine velocity. Simulations will be used to carry out this research, and simple models will be constructed.

In the CHAPS NRS, an error-state extended Kalman filter [2,11,39] provides estimates of the reference system errors. Figure 1.2 depicts such a system. The estimated errors are subtracted from the indicated trajectory, producing the estimated reference position, velocity and acceleration. This error-state model is generated from higher order truth models and is validated for performance.

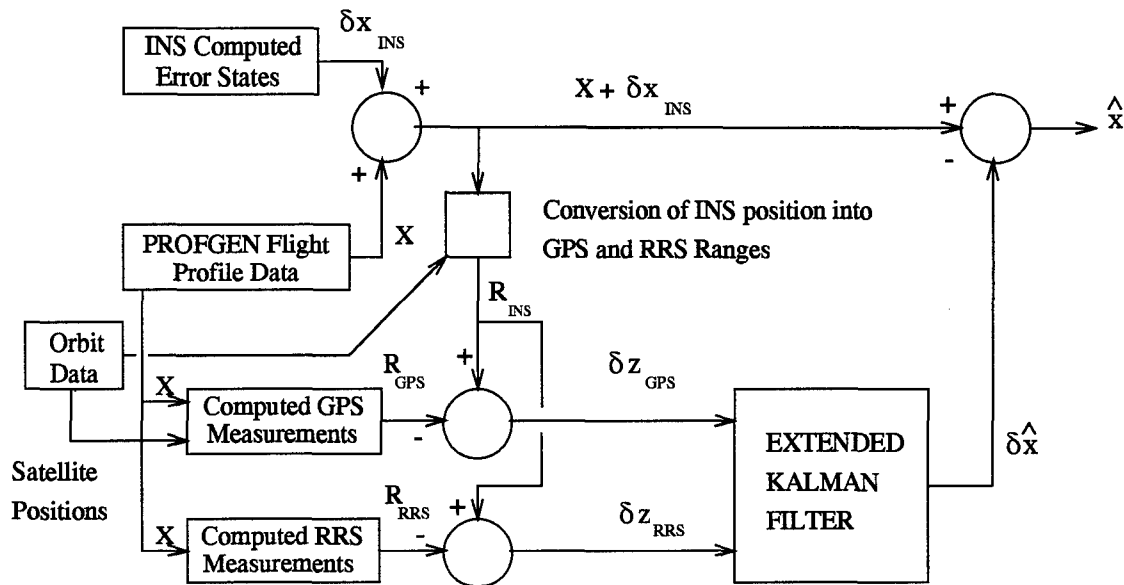


Figure 1.2 Typical NRS Error-State Model Formulation

In order to create a proper error-state model for SARS, a truth model needs to be developed. One option would be to create a truth model based upon what is known about carrier-phase GPS measurements and apply it to this “inverted” GPS problem. Such truth models, however, are based upon a mathematical description of the device, and should be validated by empirical data obtained from the “real world.” Since SARS is still in development, it is unlikely that any such empirical data can be collected at this point to validate such a model.

It is possible to generate an error-state model based upon previous carrier-phase models. Such a model would need to be modified based upon our assumptions of the operating environment. After the model is modified, it should be validated. This validation would require significant resources [39] beyond the scope of this thesis effort.

Even without formal validation it is possible to use a model; for example, one modification might involve removing model states corresponding to ionospheric errors, since the GPS signal will not be traveling through the ionosphere. In this case, it appears that our assumptions about the operating environment will improve the accuracy of our results. On the other-hand, new sources of error may exist and should be introduced to the model.

Multipath error, while not considered in past AFIT carrier-phase research [2,11], may be a significant source of error for SARS. If so, what effect does altitude have on multipath error? Does the multipath portion of the model need to be adjusted for altitude changes, and if so, how? While it may be prudent to consider the modeling of multipath as a function of altitude, it is difficult to predict the impact an altitude change should have. Hence, without real world validation, model confidence is quickly lost.

A heuristic approach to the model formulation is suggested. If one assumes that a valid error-state model cannot be confidently constructed, then the only information remaining to be exploited, aside from the carrier-phase data itself, is the fact that the aircraft will be in controlled flight, along some trajectory. If an aircraft trajectory can be broken down into distinct phases, the kinematics can be represented by simple models, such as:

- Constant Velocity, Acceleration modeled as a white Gaussian noise
- Constant Acceleration, Jerk modeled as a white Gaussian noise
- Constant Acceleration, Jerk modeled as a 1st order Markov process

It is possible that one of these models may be generic enough to provide an adequate velocity estimate over the entire flight, or, each model may be valid only during a particular segment of a flight. In this case, an adaptive filter could be devised that changes in response to flight conditions.

1.7 Materials, Data and Equipment

No special provisions are required for this research. The Sun SPARC network in the AFIT Guidance and Navigation Laboratory as well as the XR5M 6-channel and 12-channel GPS receivers will be used for experimentation during this thesis.

1.7.1 Simulation Software.

1.7.1.1 PROFGEN. The Avionics Directorate of Wright Laboratory develops and maintains a software package called PROFGEN (PROFile GENERator). PROF-

GEN allows for the creation of flight trajectories of a vehicle under continuous control over the Earth's surface. This is accomplished by solving the equations of motion of a zero-mass body responding to maneuver commands specified by the user. These maneuvers can consist of vertical turns, horizontal turns, rolls, straight flights and sinusoidal heading changes. More detailed information is available in the PROFGEN documentation [32].

1.7.1.2 MATLAB. MATLAB [27] is a technical computing environment for high performance numeric computation and visualization. MATLAB, which stands for *matrix laboratory*, is useful for conducting simulation and analysis of linear (and non-linear) systems. MATLAB features a powerful matrix interpreter, a user-friendly environment, a variety of reliable numerical integration algorithms and a graphical simulation environment called SIMULINK. MATLAB, SIMULINK and several "toolboxes" were used in the construction of the simulations and their analysis.

1.8 Overview of Thesis

The methodology in this chapter is meant to motivate the development of algorithms to determine the velocity of an aircraft flying in a trajectory. CIGTIF's performance objective for SARS is a velocity accuracy of 0.005 m/s 3-D RMS 1σ at a maximum measurement rate of 10Hz. Two approaches will be considered: a digital filtering with numeric differentiation approach and a kinematic model-based Kalman filter approach.

This thesis consists of five chapters. Chapter I has presented the problem to be solved and the approach to be taken in solving it. Chapter II covers the theory involved in this thesis. Topics covered in Chapter II include an overview of numerical differentiation, GPS measurement equations, digital filtering and Kalman filter theory. The theory involved with GPS measurements includes how the measurement equations are derived, in light of the inverted pseudolite concept. Chapter III presents the noise models and Kalman filter models implemented in this thesis. The results of the data evaluations and simulations are presented in Chapter IV and Chapter V gives conclusions and recommendations for future research.

II. Theory

2.1 Overview

This chapter describes the general theory pertaining to this research. The first section outlines the implications of noise corrupted discrete-time position measurements in velocity determination. The GPS measurement section presents the equations involved with the three basic GPS measurements: pseudorange, carrier-phase and deltarange; further information on GPS theory is available in [10]. The Kalman filtering section provides an overview of Kalman filtering/smoothing. Readers unfamiliar with these Kalman filtering topics are referred to [24,25]. Finally, the last section presents the types of digital filters used in this research.

2.2 Approximating Velocity

GPS measurements of the aircraft position will be available at discrete time intervals. These measurements can be solved in Earth Centered Earth Fixed (ECEF) coordinates and expressed as follows:

$$\mathbf{r}(t_i) = \begin{bmatrix} x(t_i) \\ y(t_i) \\ z(t_i) \end{bmatrix} \quad (2.1)$$

The velocity of the aircraft can then be defined as the derivative of position:

$$\dot{\mathbf{r}}(t_i) \equiv \lim_{h \rightarrow 0} \frac{\mathbf{r}(t_i + h) - \mathbf{r}(t_i)}{h}. \quad (2.2)$$

Unfortunately, this equation cannot be properly evaluated as h is limited to the sampling rate of SARS.

2.2.1 Taylor's Series Approximation to the Derivative. One method used to obtain the numerical derivative approximation and maintain stability is a truncated Taylor's series expansion. The Taylor's series for a function $\mathbf{r}(x)$ at $(x + h)$ expanded about x is:

$$\mathbf{r}(x + h) = \mathbf{r}(x) + \mathbf{r}'(x)h + \frac{\mathbf{r}''(x)h^2}{2!} + \frac{\mathbf{r}'''(x)h^3}{3!} + h.o.t. \quad (2.3)$$

Similarly for $\mathbf{r}(x)$ at $(x - h)$ we have

$$\mathbf{r}(x - h) = \mathbf{r}(x) - \mathbf{r}'(x)h + \frac{\mathbf{r}''(x)h^2}{2!} - \frac{\mathbf{r}'''(x)h^3}{3!} + h.o.t. \quad (2.4)$$

Combining (2.3) and (2.4) we have:

$$[\mathbf{r}(x + h) - \mathbf{r}(x - h)] = 2\mathbf{r}'(x) + 2\frac{\mathbf{r}'''(x)h^3}{3!} + 2\frac{\mathbf{r}^{(5)}(x)h^5}{5!} + h.o.t. \quad (2.5)$$

Notice that the even numbered derivative terms are eliminated. Truncating (2.5) to first order and rearranging yields the classic central difference approximation of the first derivative:

$$\mathbf{r}'(x) \cong \frac{\mathbf{r}(x + h) - \mathbf{r}(x - h)}{2h}. \quad (2.6)$$

2.2.2 Extrapolating the Central Difference Approximation. In (2.5), the even order derivatives in the Taylor's series cancel out fortuitously. It is possible to combine additional equations to cancel out additional higher order terms. Consider the following equation:

$$[\mathbf{r}(x + 2h) - \mathbf{r}(x - 2h)] = 4\mathbf{r}'(x) + 2 \cdot 2^3 \frac{\mathbf{r}'''(x)h^3}{3!} + 2 \cdot 2^5 \frac{\mathbf{r}^{(5)}(x)h^5}{5!} + h.o.t. \quad (2.7)$$

which can be combined with a scaled version of (2.5) to remove the third order derivative:

$$2^3[\mathbf{r}(x + h) - \mathbf{r}(x - h)] - [\mathbf{r}(x + 2h) - \mathbf{r}(x - 2h)] = 12\mathbf{r}'(x) + 2 \cdot (2^4 - 2^6) \frac{\mathbf{r}^{(5)}(x)h^5}{5!} + h.o.t. \quad (2.8)$$

Neglecting the fifth order and higher derivatives, we can rearrange (2.8) to solve for the following central difference equation:

$$\mathbf{r}'(x) \cong 8 \frac{\mathbf{r}(x + h) - \mathbf{r}(x - h)}{12h} - \frac{\mathbf{r}(x + 2h) - \mathbf{r}(x - 2h)}{12h} \quad (2.9)$$

This extrapolation method can be pursued further to generate approximations to derivatives with better residual error characteristics, at the expense of requiring additional data points. The central difference equation approximation for the first derivative is well documented [6,15,22,45] in numerical methods texts. Equations (2.10), (2.11) and, (2.12) show

the algorithms tested in this research.

$$\mathbf{r}'(x) \cong \frac{\mathbf{r}(x+h) - \mathbf{r}(x-h)}{2h} \quad (2.10)$$

$$\mathbf{r}'(x) \cong 8 \frac{\mathbf{r}(x+h) - \mathbf{r}(x-h)}{12h} - \frac{\mathbf{r}(x+2h) - \mathbf{r}(x-2h)}{12h} \quad (2.11)$$

$$\begin{aligned} \mathbf{r}'(x) \cong & 45 \frac{\mathbf{r}(x+h) - \mathbf{r}(x-h)}{60h} - 9 \frac{\mathbf{r}(x+2h) - \mathbf{r}(x-2h)}{60h} \\ & + \frac{\mathbf{r}(x+3h) - \mathbf{r}(x-3h)}{60h} \end{aligned} \quad (2.12)$$

For best precision, the numerical differentiation algorithm would be extrapolated as far as higher order derivatives exist for the function in question. Due to the sampled data nature of the system under consideration in this research, there is no guarantee that the function is continuous, especially in areas of high dynamics.

2.2.3 Error Analysis of the Velocity Approximation. There are many contributing factors in the overall error of the velocity approximation algorithms. Three sources of error in the velocity approximation are considered: error due to digital sampling, error due to truncation of the Taylor's series and error due to corrupted position data. This section is concerned with evaluating the extent of these errors.

2.2.3.1 Error Due to Digital Sampling. If we treat the position measurements as digital sampling of a continuous time signal, one must be concerned with the phenomena of aliasing. In the frequency domain, aliasing results in higher frequencies of a signal impersonating lower frequencies. In the time domain, aliasing results in corruption of the discrete-time signal. In order to avoid aliasing, it is necessary to sample at a rate at least two times higher than the highest frequency of the input signal. This is known as the Nyquist rate.

To determine the highest frequency component that the input signal may contain, we examine the case of a high performance fighter aircraft in a demanding flight profile. In Section 4.3.1, analysis confirms that Nyquist criterion is met for the sampling rates of interest in this research.

2.2.3.2 Error Due to Truncation. Neglecting higher order terms in the Taylor's series will cause errors of magnitude h^n where h is the sampling interval and n is the order of the derivative of the first neglected term [6,15,22]. For example, the neglected terms in (2.10) are:

$$2 \cdot 2^3 \frac{\mathbf{r}'''(x)h^3}{3!} + 2 \cdot 2^5 \frac{\mathbf{r}^{(5)}(x)h^5}{5!} + h.o.t. \quad (2.13)$$

and the order of the error is h^3 . Similarly, (2.11) and (2.12) are of order h^5 and h^7 respectively.

2.2.3.3 Implications of Noisy Position Data. Now consider errors in the position information. Each coordinate is corrupted by some error δ :

$$\mathbf{r}(t_i) = \begin{bmatrix} x(t_i) + \delta x(t_i) \\ y(t_i) + \delta y(t_i) \\ z(t_i) + \delta z(t_i) \end{bmatrix} \quad (2.14)$$

where $x(t_i)$, $y(t_i)$ and $z(t_i)$ represent true position. Using (2.6) the velocity equation for the x direction becomes:

$$\begin{aligned} \frac{dx(t_i)}{dt} &= \frac{[x(t_{i+1}) + \delta x(t_{i+1})] - [x(t_{i-1}) + \delta x(t_{i-1})]}{2\Delta t} \\ &= \frac{x(t_{i+1}) - x(t_{i-1})}{2\Delta t} + \frac{\delta x(t_{i+1}) - \delta x(t_{i-1})}{2\Delta t} \end{aligned} \quad (2.15)$$

The velocity equation can be expressed as a sum of two terms: the computed double sided velocity approximation and the error in computed velocity. In order to generate accurate velocity estimates, it is important to minimize the effect of the error term in Equation 2.15. One way to make this term approach zero is to make the sampling period very large compared to the magnitude of the difference in the error. This solution is not practical since large sampling periods invalidates the difference equation as an approximation to velocity.

Another way to reduce the effect of the error term is to make the numerator much smaller than the denominator. If the errors $\delta x(t_{i+1})$ and $\delta x(t_{i-1})$ are time correlated, they may cancel each other out, depending on the sampling rate and the time constant of the

errors. Unfortunately there are practical limits to the sampling rate. If there is a white component to the noise, or if the error terms are not exactly correlated, there will be a non-zero remainder. As the sampling rate is increased, this remainder becomes amplified by the denominator term.

Care must be taken when choosing a sampling rate; a trade-off between the accuracy of the velocity approximation and the amount of noise amplification must be made. In many applications, such as navigation, it is prudent to eliminate as much noise as possible from the position measurements before using the differencing equation to approximate velocity.

2.3 Global Positioning System Measurements

2.3.1 Pseudorange. The basic pseudorange observable is a difference between the time of transmission of the GPS signal and the time of arrival, based upon a code correlation technique. The pseudorange observation equation given by [10] is:

$$p = \| R_j - R_i \| + c \cdot (\delta_{pc} - \delta_{rc}) + \delta_{trop} + \delta_{mpath} + \delta_{ion}$$

where:

- p = is the measured pseudorange
- $\| R_j - R_i \|$ = the true, but unknown, range
- R_i = ECEF coordinates of the i^{th} receiver
- R_j = ECEF coordinates of the j^{th} pseudolite
- δ_{pc} = the pseudolite clock offset from true GPS time
- δ_{rc} = the receiver clock offset from true GPS time
- c = speed of light
- δ_{ion} = the range equivalent ionospheric delay term
- δ_{trop} = the range equivalent tropospheric delay term
- δ_{mpath} = the error due to multipath effects

Since the pseudolites used for this application will not transmit signals through the ionosphere, the error term δ_{ion} may be eliminated. The resulting pseudorange equation is:

$$p = \| R_j - R_i \| + c \cdot (\delta_{pc} - \delta_{rc}) + \delta_{trop} + \delta_{mpath} \quad (2.16)$$

which is valid for both the airborne and ground-based pseudolites. The receiver location, R_i , is known *a priori* since the ground receivers use carrier phase surveying techniques to determine precisely their position. Similarly, the ground-based pseudolite position is also known *a priori*. Thus, a good estimate of the range between the ground-based pseudolite and receiver is known. The true range can be expressed as a sum of two terms, the surveyed or estimated range, $\| \hat{R}_j - \hat{R}_i \|$, and the error in the survey, δ_R .

$$\| R_j - R_i \| = \| \hat{R}_j - \hat{R}_i \| + \delta_R \quad (2.17)$$

By subtracting the known quantity $\| \hat{R}_j - \hat{R}_i \|$ from both sides of the ground-based pseudorange observation (2.16), we define a differential correction term Δp :

$$\begin{aligned} \Delta p &= p_{gnd} - \| \hat{R}_j - \hat{R}_i \| \\ &= [c \cdot (\delta_{pc} - \delta_{rc}) + \delta_{trop} + \delta_{mpath}]_{gnd} + \delta_R \end{aligned} \quad (2.18)$$

where the subscript *gnd* denotes terms corresponding to the ground-based pseudolite.

The quantity expressed in (2.18) can be subtracted from the pseudorange observation equation for the airborne pseudolite, providing a differentially corrected pseudorange, p^* .

$$\begin{aligned} p^* &= p_{air} - \Delta p \\ &= \| R_j - R_i \| + [c \cdot (\delta_{pc} - \delta_{rc}) + \delta_{trop} + \delta_{mpath}]_{air} \\ &\quad - [c \cdot (\delta_{pc} - \delta_{rc}) + \delta_{trop} + \delta_{mpath}]_{gnd} - \delta_R \\ &= \| R_j - R_i \| + [c \cdot \delta_{pc} + \delta_{trop} + \delta_{mpath}]_{air} \\ &\quad - [c \cdot \delta_{pc} + \delta_{trop} + \delta_{mpath}]_{gnd} - \delta_R \end{aligned} \quad (2.19)$$

where the subscript *air* denotes terms corresponding to the airborne pseudolite. This eliminates the common receiver clock bias since $[\delta_{rc}]_{gnd} = [\delta_{rc}]_{air}$, and may reduce the tropospheric delay effect.

To further reduce the error in (2.19), a tropospheric error correction can be calculated. In GPS applications, the tropospheric delay is considered a function of humidity,

temperature and altitude at the receiver. The implications of modeling the tropospheric delay term is developed in Section 3.3.1.

2.3.2 Carrier-Phase. This section develops the essential pseudolite-based carrier-phase equations required for this effort. For the reader unfamiliar with carrier-phase methods, a more general derivation of the GPS carrier-phase equations is presented in [2, 11].

A carrier-phase measurement is derived from the phase shift between the transmitter-generated signal and receiver-generated signal. In GPS applications, the transmitter is a satellite; in this application, the transmitter is one of two pseudolites. One pseudolite is located at a surveyed location on the Earth's surface, in view of all the receivers. The second pseudolite is mounted on an aircraft, flying in a trajectory over the range.

The carrier-phase observation equation [2] for GPS pseudolites is given by:

$$\Phi = -f \cdot (\delta_{pc} - \delta_{rc}) - \frac{f}{c} \cdot (\|R_j - R_i\| - \delta_{ion} + \delta_{trop} + \delta_{mpath}) \quad (2.20)$$

where: Φ = the phase-range in cycles between pseudolite and receiver
 f = the frequency of transmission
 δ_{pc} = the pseudolite clock offset from true GPS time
 δ_{rc} = the user clock offset from true GPS time
 c = speed of light
 $\|R_j - R_i\|$ = the true, but unknown, range
 δ_{ion} = the range equivalent ionospheric delay term
 δ_{trop} = the range equivalent tropospheric delay term
 δ_{mpath} = the error due to multipath effects

Since the pseudolite signals do not pass through the ionosphere, the term δ_{ion} can be eliminated from (2.20). The resulting carrier-phase observation equation for pseudolites is:

$$\Phi = -f \cdot (\delta_{pc} - \delta_{rc}) - \frac{f}{c} \cdot (\|R_j - R_i\| + \delta_{trop} + \delta_{mpath}) \quad (2.21)$$

Because the carrier-phase measurement is a phase shift, it represents only a fraction of a wavelength of the carrier. The phase-range measurement at some time epoch, t , is

represented by the following equation:

$$\Phi(t) = \Phi_{frac}(t) + \Phi_{int}(t_o, t) + N(t_o) \quad (2.22)$$

where $\Phi_{frac}(t)$ is the fractional part of the total wavelength, $\Phi_{int}(t_o, t)$ is an integer number of phase cycles from an initial epoch, t_o , to the current epoch, t , and $N(t_o)$ is an integer phase ambiguity term. The phase ambiguity term is also known as the *cycle ambiguity* and it represents the difference between the true integer count at time t_o , and the current integer count at t_o measured or calculated by the receiver [11].

The carrier phase measurement, $\Phi_{measured}(t)$, is equal to the sum of the fraction observation at time epoch, t , and the integer count at the same time epoch, t , and can be represented by:

$$\Phi_{measured}(t) = \Phi_{frac}(t) + \Phi_{int}(t_o, t) \quad (2.23)$$

The total phase range at time epoch, t , from (2.22) can now be written as:

$$\Phi(t) = \Phi_{measured}(t) + N(t) \quad (2.24)$$

Substituting (2.21) into (2.24) produces the measured range for the pseudolite carrier-phase observable:

$$\begin{aligned} \Phi_{measured}(t) &= \Phi(t) - N(t) \\ &= -f \cdot (\delta_{pc} - \delta_{rc}) - \frac{f}{c} \cdot (\|R_j - R_i\| + \delta_{trop} + \delta_{mpath}) - N(t) \end{aligned} \quad (2.25)$$

Multiplying (2.25) by the negative of the cycle wavelength, $-\lambda$, converts from cycle units to distance units:

$$\begin{aligned} \Phi(t) &= -\lambda \cdot \Phi_{measured}(t) \\ &= \|R_j - R_i\| + c \cdot (\delta_{pc} - \delta_{rc}) + \delta_{trop} + \delta_{mpath} + \lambda \cdot N(t) \end{aligned} \quad (2.26)$$

2.3.2.1 Carrier Phase Double Differencing. The between-receiver/satellites double differencing method described in [2,36] is the method to be implemented in this

research. It is modified slightly to a between-receiver/between-pseudolites method and is depicted in Figure 2.1. This method subtracts a between-receiver single difference with

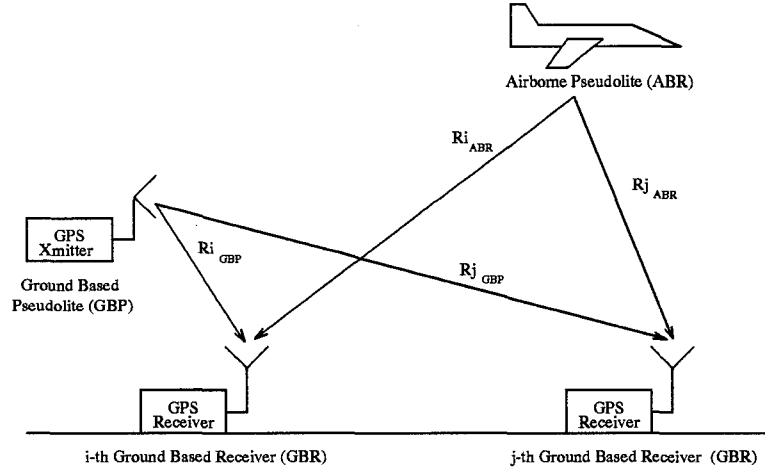


Figure 2.1 Illustration of Between Receivers/Pseudolites Double Difference

another between-receiver single difference using the same receivers and the ground-based reference pseudolite. Additionally, the integer ambiguity term must be estimated. In [36], preliminary results using this double differencing method with conventional integer ambiguity resolution techniques are presented. The result of this double differencing method is the elimination of pseudolite and receiver clock error biases. An atmospheric error term reduction is dependent upon the relative magnitudes and directions of the ranges between the transmitters and receivers as well as the homogeneity of the atmosphere, and subsequently, is highly application specific.

2.3.3 Deltarange. By differentiating the carrier-phase measurement equation (2.26), we can derive an approximation to the range rate:

$$\frac{d\Phi}{dt} \cong \lim_{\Delta t \rightarrow 0} \left\{ \frac{\Delta \|R_j - R_i\| + c \cdot \Delta(\delta_{pc} - \delta_{rc}) + \Delta\delta_{trop} + \delta_{mpath} + \lambda \cdot \Delta N(t)}{\Delta t} \right\} \quad (2.27)$$

which approaches the true range rate as Δt approaches zero. The true range rate equation is given by:

$$\frac{d\Phi}{dt} = \frac{d \|R_j - R_i\|}{dt} + c \frac{d\delta_{trop}}{dt} + c \frac{d\delta_{mpath}}{dt} + c \frac{d\delta_{pc}}{dt} - c \frac{d\delta_{rc}}{dt}$$

$$= \frac{d \| R_j - R_i \|}{dt} + c \frac{d\delta_{error}}{dt} \quad (2.28)$$

where $\delta_{error} = \delta_{trop} + \delta_{mpath} + \delta_{pc} - \delta_{rc}$. This assumes that the integer phase ambiguity term, $N(t)$, remains constant over the time interval such that $\Delta N(t) = 0$.

2.3.3.1 Solving the Range Rate Equation for User Velocity. User velocity is embedded in the first term of (2.28). Evaluating this term we have:

$$\begin{aligned} \frac{d \| R_j - R_i \|}{dt} &= \frac{d}{dt} \sqrt{(x_j - x_i)^2 + (y_j - y_i)^2 + (z_j - z_i)^2} \\ &= \frac{(x_j - x_i)(\dot{x}_j - \dot{x}_i) + (y_j - y_i)(\dot{y}_j - \dot{y}_i) + (z_j - z_i)(\dot{z}_j - \dot{z}_i)}{\sqrt{(x_j - x_i)^2 + (y_j - y_i)^2 + (z_j - z_i)^2}} \quad (2.29) \end{aligned}$$

where i denotes the i^{th} pseudolite and j , the j^{th} receiver. Letting α_1 , α_2 , and α_3 be the directional derivatives:

$$\begin{aligned} \alpha_1 &= \frac{(x_j - x_i)}{\sqrt{(x_j - x_i)^2 + (y_j - y_i)^2 + (z_j - z_i)^2}} \\ \alpha_2 &= \frac{(y_j - y_i)}{\sqrt{(x_j - x_i)^2 + (y_j - y_i)^2 + (z_j - z_i)^2}} \\ \alpha_3 &= \frac{(z_j - z_i)}{\sqrt{(x_j - x_i)^2 + (y_j - y_i)^2 + (z_j - z_i)^2}} \end{aligned}$$

Equation (2.29) can be expressed as:

$$\frac{d \| R_j - R_i \|}{dt} = \alpha_1(\dot{x}_j - \dot{x}_i) + \alpha_2(\dot{y}_j - \dot{y}_i) + \alpha_3(\dot{z}_j - \dot{z}_i) \quad (2.30)$$

Substituting (2.30) into (2.28) yields:

$$\frac{d\Phi}{dt} = \alpha_1(\dot{x}_j - \dot{x}_i) + \alpha_2(\dot{y}_j - \dot{y}_i) + \alpha_3(\dot{z}_j - \dot{z}_i) + c \frac{d\delta_{error}}{dt} \quad (2.31)$$

Rearranging this equation to separate pseudolite velocity from user velocity:

$$\frac{d\Phi}{dt} + \alpha_1\dot{x}_i + \alpha_2\dot{y}_i + \alpha_3\dot{z}_i = \alpha_1\dot{x}_j + \alpha_2\dot{y}_j + \alpha_3\dot{z}_j + c \frac{d\delta_{error}}{dt} \quad (2.32)$$

For the roving pseudolite on-board the aircraft, the velocities of the receivers are zero with respect to the ECEF frame. Equation (2.32) for the airborne pseudolite becomes:

$$\frac{d\Phi}{dt}_{air} = \alpha_1 \dot{x}_j + \alpha_2 \dot{y}_j + \alpha_3 \dot{z}_j + c \frac{d\delta_{error}}{dt}_{air} \quad (2.33)$$

For the ground-based pseudolite, not only are the velocities of the receivers zero, but also the velocity of the pseudolite itself is zero. Equation (2.32) for the ground-based pseudolite becomes:

$$\begin{aligned} \frac{d\Phi}{dt}_{gnd} &= c \frac{d\delta_{error}}{dt}_{gnd} \\ &= c \frac{d\delta_{trop}}{dt} + c \frac{d\delta_{mpath}}{dt} + c \frac{d\delta_{pc}}{dt}_{gnd} - c \frac{d\delta_{rc}}{dt}_{gnd} \end{aligned} \quad (2.34)$$

If we assume that simultaneous measurements of the pseudolites is possible, the ground-based pseudolite can be used as a differential correction to the airborne pseudolite. Since the same receiver is used to detect both pseudolite signals, the quantities $\frac{d\delta_{rc}}{dt}_{gnd}$ and $\frac{d\delta_{rc}}{dt}_{air}$ are equal. For the remaining error terms, $\frac{d\delta_{pc}}{dt}$, $c \frac{d\delta_{trop}}{dt}$ and $c \frac{d\delta_{mpath}}{dt}$, it is not known what benefit differential corrections will have. Assuming the pseudolites are of the same make and model, they should use the same clock device and have similar drift characteristics, $\frac{d\delta_{pc}}{dt}$. However, the airborne clock will be subjected to higher g-forces and may suffer from the effects of g-induced disturbances to the oscillator [20].

Nonetheless, the tropospheric error rate, $\frac{d\delta_{trop}}{dt}$, may be small enough over such a short period of time to neglect entirely. This assumes that there is a high correlation in tropospheric error between subsequent measurements, which is likely given that sequential signals are passing through (relatively) the same atmosphere. While the pseudolite signals are travelling through essentially the same atmosphere (wet and dry refractivities), the tropospheric error terms are also dependent on user altitude, range and elevation angle [17]. Experimentation may be useful in determining the usefulness of such a differential correction. The differentially corrected range rate equation is:

$$\begin{aligned}
\frac{d\Phi}{dt}_{diff} &= \frac{d\Phi}{dt}_{air} - \frac{d\Phi}{dt}_{gnd} \\
&= \alpha_1 \dot{x}_j + \alpha_2 \dot{y}_j + \alpha_3 \dot{z}_j + c \frac{d\delta_{error}}{dt}_{air} - c \frac{d\delta_{error}}{dt}_{gnd} \\
&= \alpha_1 \dot{x}_j + \alpha_2 \dot{y}_j + \alpha_3 \dot{z}_j + c \frac{d\delta_{trop}}{dt}_{air-gnd} + c \frac{d\delta_{mpath}}{dt}_{air-gnd} + c \frac{d\delta_{pc}}{dt}_{air-gnd} \\
&= \alpha_1 \dot{x}_j + \alpha_2 \dot{y}_j + \alpha_3 \dot{z}_j + c \frac{d\delta_{error}}{dt}_{air-gnd} \tag{2.35}
\end{aligned}$$

2.4 Kalman Filtering/Smoothing

Although solutions to the GPS ranging equations are non-linear, in this exploratory research, the Kalman filter measurement models were kept linear. This is accomplished by solving the ranging equations before presenting them to the Kalman filter. This was done to keep the analysis focused on assessing the performance and suitability of the Kalman filter algorithm itself. If the desired level of performance can be achieved with the standard Kalman filter, and possibly exceeded, the study of the effects of compensation for non-linear measurement equations is warranted.

While the Kalman filter lends itself to use in real-time applications, it is also useful in non-real time estimation problems. In fact, by taking advantage of information contained in “future” measurements, a better state estimate can be provided in most cases [25]. This use of “future” measurements in a Kalman filter structure describes the optimal smoothing problem.

While many different smoother formulations exist, the *fixed-interval smoother* as described in [25], is most applicable to this research. The fixed-interval smoother is especially useful for post-mission data analysis as it allows all measurement data collected to be used to generate the state estimates at a given time, t_i .

Considering a discrete-time model of states $\mathbf{x}(t_i)$, and measurements $\mathbf{z}(t_i)$:

$$\mathbf{x}(t_{i+1}) = \Phi(t_{i+1}, t_i)\mathbf{x}(t_i) + \mathbf{B}_d(t_i)\mathbf{u}(t_i) + \mathbf{G}_d(t_i)\mathbf{w}_d(t_i) \tag{2.36}$$

$$\mathbf{z}(t_i) = \mathbf{H}(t_i)\mathbf{x}(t_i) + \mathbf{v}(t_i) \tag{2.37}$$

where the initial conditions $\mathbf{x}(t_0)$ have a mean $\hat{\mathbf{x}}_0$ and covariance \mathbf{P}_0 . States are propagated by a discrete-time state transition matrix $\Phi(t_{i+1}, t_i)$. Also, $\mathbf{w}_d(t_i)$ is a discrete-time white Gaussian noise with covariance:

$$E \{ \mathbf{w}_d(t_i) \mathbf{w}_d^T(t_j) \} = \begin{cases} \mathbf{Q}_d(t_i) & t_i = t_j \\ \mathbf{0} & t_i \neq t_j \end{cases} \quad (2.38)$$

and is independent of the measurement noise vector, $\mathbf{v}(t_i)$, which also is described as zero-mean white Gaussian, with noise covariance, $\mathbf{R}(t_i)$:

$$E \{ \mathbf{v}(t_i) \mathbf{v}^T(t_j) \} = \begin{cases} \mathbf{R}(t_i) & t_i = t_j \\ \mathbf{0} & t_i \neq t_j \end{cases} \quad (2.39)$$

The smoothing procedure can be thought of as having three steps. First a conventional forward running Kalman filter generates state estimates, denoted $\hat{\mathbf{x}}(t_i^+)$, where the (+) superscript indicates the state estimate after a measurement update at time t_i . Second, a backward running Kalman filter, independent of the forward running filter, computes state estimates $\hat{\mathbf{x}}_b(t_i^-)$, where the (-) superscript indicates the state estimate before a measurement update at time t_i . Third, the state estimates are combined optimally to produce $\hat{\mathbf{x}}(t_i/t_f)$, by considering them as two separate observations of $\mathbf{x}(t_i)$, weighting each by factors related to the covariances $\mathbf{P}(t_i^+)$ and $\mathbf{P}_b(t_i^-)$. Computationally, it is more efficient to run and store the results of the backward filter first, then combine steps one and three into a single algorithm that computes the forward filter estimate and the smoothed estimate simultaneously.

The fixed-interval smoothing algorithm, as presented in [25], is shown below. A conventional forward running Kalman filter with propagation equations:

$$\hat{\mathbf{x}}(t_{k+1}^-) = \Phi(t_{k+1}, t_k) \hat{\mathbf{x}}(t_k^+) + \mathbf{B}_d(t_k) \mathbf{u}(t_k) \quad (2.40)$$

$$\hat{\mathbf{P}}(t_{k+1}^-) = \Phi(t_{k+1}, t_k) \mathbf{P}(t_k^+) \Phi^T(t_{k+1}, t_k) + \mathbf{G}_d(t_k) \mathbf{Q}_d(t_k) \mathbf{G}_d^T(t_k) \quad (2.41)$$

and measurement update equations:

$$\mathbf{K}(t_k) = \mathbf{P}(t_k^-) \mathbf{H}^T(t_k) [\mathbf{H}(t_k) \mathbf{P}(t_k^-) \mathbf{H}^T(t_k) + \mathbf{R}(t_k)]^{-1} \quad (2.42)$$

$$\hat{\mathbf{x}}(t_k^+) = \hat{\mathbf{x}}(t_k^-) + \mathbf{K}(t_k) [\mathbf{z}_k - \mathbf{H}(t_k) \hat{\mathbf{x}}(t_k^-)] \quad (2.43)$$

$$\mathbf{P}(t_k^+) = \mathbf{P}(t_k^-) - \mathbf{K}(t_k) \mathbf{H}(t_k) \mathbf{P}(t_k^-) \quad (2.44)$$

and initial conditions:

$$\hat{\mathbf{x}}(t_0) = \hat{\mathbf{x}}_0 \quad (2.45)$$

$$\mathbf{P}(t_0) = \mathbf{P}_0 \quad (2.46)$$

are used to generate a state estimate and covariance for each time. A backwards running Kalman filter is implemented in inverse-covariance form since no *a priori* statistical information is known about the initial conditions. Measurement updates are given by:

$$\hat{\mathbf{y}}_b(t_k^+) = \hat{\mathbf{y}}_b(t_k^-) + \mathbf{H}^T(t_k) \mathbf{R}^{-1}(t_k) \mathbf{z}_k \quad (2.47)$$

$$\mathbf{P}_b^{-1}(t_k^+) = \mathbf{P}_b^{-1}(t_k^-) + \mathbf{H}^T(t_k) \mathbf{R}^{-1}(t_k) \mathbf{H}(t_k) \quad (2.48)$$

The states are propagated backwards in time by:

$$\mathbf{J}(t_k) = \mathbf{P}_b^{-1}(t_k^+) \mathbf{G}_d(t_{k-1}) [\mathbf{G}_d^T(t_{k-1}) \mathbf{P}_b^{-1}(t_k^+) \mathbf{G}_d(t_{k-1}) + \mathbf{Q}_d^{-1}(t_{k-1})]^{-1}$$

$$\mathbf{L}(t_k) = \mathbf{I} - \mathbf{J}(t_k) \mathbf{G}_d^T(t_{k-1})$$

$$\hat{\mathbf{y}}_b(t_{k-1}^-) = \Phi^T(t_k, t_{k+1}) \mathbf{L}(t_k) [\hat{\mathbf{y}}_b(t_k^+) - \mathbf{P}_b^{-1}(t_k^+) \mathbf{B}_d(t_{k-1}) \mathbf{u}(t_{k-1})] \quad (2.49)$$

$$\begin{aligned} \mathbf{P}_b^{-1}(t_{k-1}^-) &= \Phi^T(t_k, t_{k+1}) \{ \mathbf{L}(t_k) \mathbf{P}_b^{-1}(t_k^+) \mathbf{L}^T(t_k) \\ &+ \mathbf{J}(t_k) \mathbf{Q}_d^{-1}(t_{k-1}) \mathbf{J}^T(t_k) \} \Phi(t_k, t_{k+1}) \end{aligned} \quad (2.50)$$

with initial conditions:

$$\hat{\mathbf{y}}_b(t_f^-) = 0 \quad (2.51)$$

$$\mathbf{P}_b^{-1}(t_f^-) = 0 \quad (2.52)$$

The smoothed estimate is generated by combining $\hat{\mathbf{x}}(t_i^+)$, $\mathbf{P}(t_i^+)$, $\hat{\mathbf{y}}_b(t_i^-)$, and $\mathbf{P}_b^{-1}(t_i^-)$ in:

$$\begin{aligned}\mathbf{X}(t_i) &= [\mathbf{I} + \mathbf{P}(t_i^+) \mathbf{P}_b^{-1}(t_i^-)]^{-1} \\ \mathbf{W}(t_i) &= \mathbf{P}(t_i^+) \mathbf{X}^T(t_i) \\ \mathbf{Y}(t_i) &= \mathbf{I} - \mathbf{W}(t_i) \mathbf{P}_b^{-1}(t_i^-) \mathbf{W}^T(t_i) \\ \mathbf{P}(t_i/t_f) &= \mathbf{Y}(t_i) \mathbf{P}(t_i^+) \mathbf{Y}^T(t_i) + \mathbf{W}(t_i) \mathbf{P}_b^{-1}(t_i^-) \mathbf{W}^T(t_i) \quad (2.53)\end{aligned}$$

$$\hat{\mathbf{x}}(t_i/t_f) = \mathbf{X}(t_i) \hat{\mathbf{x}}(t_i^+) + \mathbf{P}(t_i/t_f) \hat{\mathbf{y}}_b(t_i^-) \quad (2.54)$$

where $\mathbf{X}(t_i)$, $\mathbf{W}(t_i)$, and $\mathbf{Y}(t_i)$ are defined as intermediate terms used to evaluate the smoothed state estimate, $\hat{\mathbf{x}}(t_i/t_f)$, and associated covariance, $\mathbf{P}(t_i/t_f)$. The notation (t_i/t_f) stands for "at time, t_i , based on measurements through time t_i and on measurements from time t_f ".

A metric has been developed to determine the relative benefit of Kalman smoothing over Kalman filtering alone. This metric, the *Fraser smoothability criterion* [25], is based upon an eigenvalue decomposition of the stochastic controllability matrix:

$$U_k(t_i) = \begin{bmatrix} \mathbf{Q}_d(t_i) & \Phi(t_{i+1}, t_i) \mathbf{Q}_d(t_i) & \Phi^2(t_{i+1}, t_i) \mathbf{Q}_d(t_i) & \cdots & \Phi^{k-1}(t_{i+1}, t_i) \mathbf{Q}_d(t_i) \end{bmatrix} \quad (2.55)$$

As the eigenvalues of the stochastic controllability matrix become large, the greater the relative benefit of smoothing.

2.5 Digital Filtering

This section describes the types of digital filters considered in this research: Finite Impulse Response (FIR) filters and Infinite Impulse Response (IIR) filters.

2.5.1 FIR Filter. The causal FIR filter, shown in Figure 2.2, is a non-recursive discrete-time filter that depends only on the present and past input signals. The transfer function of an FIR filter is given as:

$$H(z) = \sum_{n=0}^{N-1} h(n) z^{-n}, \quad (2.56)$$

where $h(n)$ is the filter impulse response of length N .

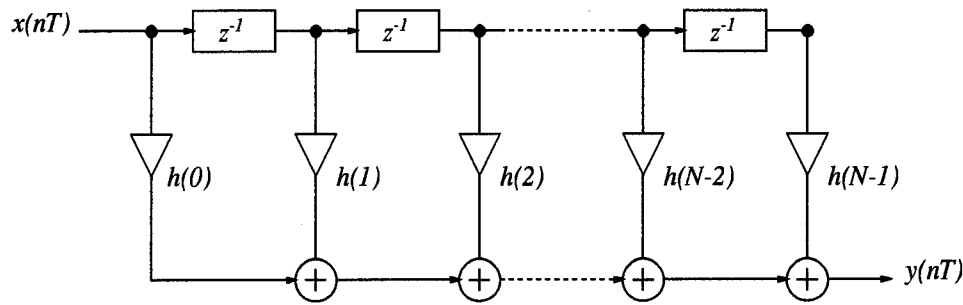


Figure 2.2 Structure of FIR Filter

The FIR filter has several interesting properties:

Linear Phase An FIR filter can be designed with linear phase, wherein we assume that there will be no phase distortion of the filtered signal.

Stability FIR filters are non-recursive and inherently stable.

Numerics FIR filters are less sensitive to coefficient accuracy and quantization noise problems than IIR filters.

Filter Order To achieve the same magnitude response as an IIR filter, FIR filters are of a much higher order than IIR filters.

2.5.2 IIR Filter. The IIR filter, shown in Figure 2.3, is a recursive discrete-time filter that uses past and present outputs as well as inputs. The transfer function of an IIR filter is given as:

$$H(z) = \frac{\sum_{i=0}^M A_i z^{-i}}{1 + \sum_{i=1}^N B_i z^{-i}} \quad (2.57)$$

The use of past and present outputs in the IIR filter formulation, also known as feedback, results in some interesting properties:

Non-Linear Phase A casual IIR filter has a non-linear phase response. The implementations of a non-causal and causal IIR filter can be combined, however, to produce a zero phase response.

Stability IIR filters employ feedback and can be unstable.

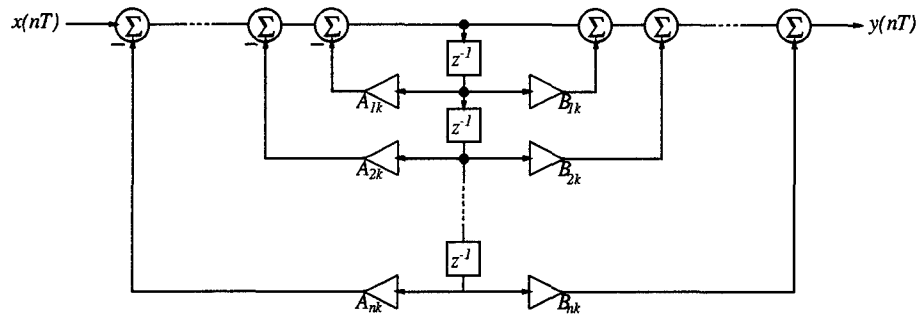


Figure 2.3 Structure of IIR Filter (Canonic Form)

Numerics IIR filters are sensitive to coefficient accuracy and quantization noise problems.

Filter Order IIR filters are typically of much lower order than a corresponding FIR filter.

Having a lower order also gives the IIR filter a better (shorter) transient response, requiring fewer sample periods to reach steady-state operation.

There are four classic IIR filters: Butterworth, Chebyshev, inverse Chebyshev (or Chebyshev II) and Elliptic. These four filter types can be classified under two error approximation measures. One measure involves a Taylor's series expansion, equating as many of the derivatives of the desired response to actual response as possible. The other measure attempts to minimize the maximum difference between the desired and actual responses over a frequency range. These IIR filters are often designed as analog filters and transformed to digital filters using the bilinear transformation. Good discussions of IIR filter design can be found in digital signal processing textbooks, such as [7,31].

2.6 Summary

This chapter has given a brief introduction to calculating an approximation to velocity from discrete position data. Also given is theory relating to the "raw" GPS measurements: pseudorange, deltarange and carrier-phase. The Kalman filter/smoothen is presented as a means to model the trajectory of an aircraft in controlled flight. Finally, the FIR and IIR digital filter architectures are outlined and proposed for this research. The material presented in this chapter forms a base of information, essential for understanding the results to be presented later.

III. Models

3.1 Overview

This chapter begins by presenting the simple kinematic models describing the trajectory of an aircraft in controlled flight. Next, the tropospheric estimation error, receiver noise and multipath error models are developed for use in both the Kalman filter/smoothen and discrete-time filtering and numerical methods approaches. Finally, a computer-assisted design methodology for the FIR and IIR discrete-time filters is presented.

3.2 Kinematic Models

The kinematic models developed in this section are intended to adequately describe the motion of an aircraft along a trajectory segment. A trajectory segment is defined as a continuous portion of the overall trajectory.

Kinematic modeling describes motion by defining a kinematic position vector

$$\mathbf{r}(t) = \{x(t), y(t), z(t)\}, \quad (3.1)$$

a kinematic velocity vector,

$$\mathbf{v}(t) = \frac{d\mathbf{r}(t)}{dt} = \left\{ \frac{dx(t)}{dt}, \frac{dy(t)}{dt}, \frac{dz(t)}{dt} \right\}, \quad (3.2)$$

a kinematic acceleration vector,

$$\mathbf{a}(t) = \frac{d^2\mathbf{r}(t)}{dt^2} = \left\{ \frac{d^2x(t)}{dt^2}, \frac{d^2y(t)}{dt^2}, \frac{d^2z(t)}{dt^2} \right\}, \quad (3.3)$$

and so on:

$$\frac{d^n\mathbf{r}(t)}{dt^n} = \left\{ \frac{d^nx(t)}{dt^n}, \frac{d^ny(t)}{dt^n}, \frac{d^nz(t)}{dt^n} \right\}. \quad (3.4)$$

These representations of motion are each equivalent if the appropriate initial conditions are known and the function $r(t)$ is continuously differentiable. In practice, these assumptions generally do not hold and the closest representation to the measurement is chosen. In this way, position information can be used to determine an approximation to velocity.

For this effort, the initial conditions are not precisely known, the time history is discretized and the position measurements are noise corrupted. The technique of pseudo-noise addition [25] is used in an attempt to compensate for these shortcomings. The models can be expressed as a system of stochastic difference equations of the form:

$$\mathbf{x}(t_i) = \Phi(t_i, t_{i-1})\mathbf{x}(t_{i-1}) + \mathbf{G}_d(t_i)\mathbf{w}_d(t_{i-1}) \quad (3.5)$$

$$\mathbf{z}(t_i) = \mathbf{H}(t_i)\mathbf{x}(t_i) + \mathbf{v}(t_i), \quad (3.6)$$

where: $\mathbf{x}(t_i)$ = n-dimensional system state vector
 $\Phi(t_i, t_{i-1})$ = state transition matrix
 $\mathbf{G}_d(t_i)$ = noise distribution matrix
 $\mathbf{w}_d(t_{i-1})$ = white Gaussian dynamics noise vector of covariance, $\mathbf{Q}(t)$
 $\mathbf{z}(t_i)$ = m-dimensional measurement vector
 $\mathbf{H}(t_i)$ = measurement matrix
 $\mathbf{v}(t_i)$ = white Gaussian measurement noise vector of covariance, $\mathbf{R}(t)$.

Three simple kinematic models are used in this research: a constant velocity with white noise added, constant acceleration with white noise added, and constant acceleration with noise modeled as a first order Markov process.

3.2.1 Constant Velocity. The constant velocity model assumes that the aircraft's acceleration is well described by a zero mean white Gaussian noise, \mathbf{w}_a , of strength \mathbf{Q}_a . The constant velocity model is given by:

$$\mathbf{x} = \begin{bmatrix} p_x & v_x & p_y & v_y & p_z & v_z \end{bmatrix}^T \quad (3.7)$$

and

$$\Phi(t_i, t_{i-1}) = \begin{bmatrix} 1 & T_s & 0 & 0 & 0 & 0 \\ 0 & 1 & 0 & 0 & 0 & 0 \\ 0 & 0 & 1 & T_s & 0 & 0 \\ 0 & 0 & 0 & 1 & 0 & 0 \\ 0 & 0 & 0 & 0 & 1 & T_s \\ 0 & 0 & 0 & 0 & 0 & 1 \end{bmatrix} \quad (3.8)$$

where T_s is the sampling time of the discrete system, and \mathbf{Q}_d is the equivalent discrete time noise approximated by:

$$\mathbf{Q}_d(t_i) \approx \frac{1}{2} [\Phi(t_i, t_{i-1}) \mathbf{G}(t) \mathbf{Q}(t) \mathbf{G}^T(t) \Phi^T(t_i, t_{i-1}) + \mathbf{G}(t) \mathbf{Q}(t) \mathbf{G}^T(t_{i-1})] \cdot T_s \quad (3.9)$$

and $\mathbf{Q}(t)$ is given by:

$$\mathbf{Q}(t) = \begin{bmatrix} \mathbf{q}_x & 0 & 0 \\ 0 & \mathbf{q}_y & 0 \\ 0 & 0 & \mathbf{q}_z \end{bmatrix} \quad (3.10)$$

where \mathbf{q}_x , \mathbf{q}_y , and \mathbf{q}_z are tunable parameters. The noise distribution matrix is given by:

$$\mathbf{G}(t) = \begin{bmatrix} 0 & 0 & 0 \\ 1 & 0 & 0 \\ 0 & 0 & 0 \\ 0 & 1 & 0 \\ 0 & 0 & 0 \\ 0 & 0 & 1 \end{bmatrix}. \quad (3.11)$$

The measurement matrix \mathbf{H} is given by:

$$\mathbf{H} = \begin{bmatrix} 1 & 0 & 0 & 0 & 0 & 0 \\ 0 & 0 & 1 & 0 & 0 & 0 \\ 0 & 0 & 0 & 0 & 1 & 0 \end{bmatrix} \quad (3.12)$$

with a measurement noise covariance of:

$$\mathbf{R} = \begin{bmatrix} \mathbf{r}_x & 0 & 0 \\ 0 & \mathbf{r}_y & 0 \\ 0 & 0 & \mathbf{r}_z \end{bmatrix} \quad (3.13)$$

where \mathbf{r}_x , \mathbf{r}_y , and \mathbf{r}_z are tunable parameters.

3.2.2 *Constant Acceleration.* Similarly the constant acceleration model assumes jerk is modeled as a zero mean white Gaussian noise and is given by:

$$\mathbf{x} = \begin{bmatrix} p_x & v_x & a_x & p_y & v_y & a_y & p_z & v_z & a_z \end{bmatrix}^T \quad (3.14)$$

with a state transition matrix:

$$\Phi(t_i, t_{i-1}) = \begin{bmatrix} 1 & T_s & \frac{T_s^2}{2} & 0 & 0 & 0 & 0 & 0 & 0 \\ 0 & 1 & T_s & 0 & 0 & 0 & 0 & 0 & 0 \\ 0 & 0 & 1 & 0 & 0 & 0 & 0 & 0 & 0 \\ 0 & 0 & 0 & 1 & T_s & \frac{T_s^2}{2} & 0 & 0 & 0 \\ 0 & 0 & 0 & 0 & 1 & T_s & 0 & 0 & 0 \\ 0 & 0 & 0 & 0 & 0 & 1 & 0 & 0 & 0 \\ 0 & 0 & 0 & 0 & 0 & 0 & 1 & T_s & \frac{T_s^2}{2} \\ 0 & 0 & 0 & 0 & 0 & 0 & 0 & 1 & T_s \\ 0 & 0 & 0 & 0 & 0 & 0 & 0 & 0 & 1 \end{bmatrix} \quad (3.15)$$

where T_s is the sampling time of the discrete system, and \mathbf{Q}_d is the equivalent discrete time noise given by (3.9) and (3.10). The noise distribution matrix is:

$$\mathbf{G}(t) = \begin{bmatrix} 0 & 0 & 0 \\ 0 & 0 & 0 \\ 1 & 0 & 0 \\ 0 & 0 & 0 \\ 0 & 0 & 0 \\ 0 & 1 & 0 \\ 0 & 0 & 0 \\ 0 & 0 & 0 \\ 0 & 0 & 1 \end{bmatrix}. \quad (3.16)$$

The measurement matrix \mathbf{H} is given by:

$$\mathbf{H} = \begin{bmatrix} 1 & 0 & 0 & 0 & 0 & 0 & 0 & 0 & 0 \\ 0 & 0 & 0 & 1 & 0 & 0 & 0 & 0 & 0 \\ 0 & 0 & 0 & 0 & 0 & 0 & 0 & 1 & 0 \end{bmatrix} \quad (3.17)$$

with a measurement noise covariance of:

$$\mathbf{R} = \begin{bmatrix} r_x & 0 & 0 \\ 0 & r_y & 0 \\ 0 & 0 & r_z \end{bmatrix} \quad (3.18)$$

where r_x , r_y , and r_z are tunable parameters.

3.2.3 Constant Acceleration, Noise 1st Order Gauss-Markov. In this section, the constant acceleration model developed in Section 3.2.2 is augmented with additional shaping filter states. This model is used to describe the jerk of the aircraft as a zero mean, first order Gauss-Markov process. This type of model is very useful for approximating a variety of empirically observed band-limited noises [24] and is popular in the open literature [5,42,46]. The model is described by:

$$\dot{\mathbf{x}}(t) = -(1/T)\mathbf{x}(t) + \mathbf{w}(t) \quad (3.19)$$

Also known as a first-order lag, driven by white Gaussian noise of strength $Q = 2\sigma^2/T$, this process produces an output with an autocorrelation described by

$$\Psi(\tau) = E\{\mathbf{x}(t)\mathbf{x}(t+\tau)\} = \sigma^2 e^{-|\tau|/T} \quad (3.20)$$

where T is the correlation time and σ^2 is the mean squared value. The first-order Gauss-Markov process is an exponentially time-correlated process.

The model structure is identical to the model presented in Section 3.2.2 with the exception of the state transition matrix:

$$\Phi(t_i, t_{i-1}) = \begin{bmatrix} 1 & T_s & f_{1,3} & 0 & 0 & 0 & 0 & 0 & 0 \\ 0 & 1 & f_{2,3} & 0 & 0 & 0 & 0 & 0 & 0 \\ 0 & 0 & f_{3,3} & 0 & 0 & 0 & 0 & 0 & 0 \\ 0 & 0 & 0 & 1 & T_s & f_{4,6} & 0 & 0 & 0 \\ 0 & 0 & 0 & 0 & 1 & f_{5,6} & 0 & 0 & 0 \\ 0 & 0 & 0 & 0 & 0 & f_{6,6} & 0 & 0 & 0 \\ 0 & 0 & 0 & 0 & 0 & 0 & 1 & T_s & f_{7,9} \\ 0 & 0 & 0 & 0 & 0 & 0 & 0 & 1 & f_{8,9} \\ 0 & 0 & 0 & 0 & 0 & 0 & 0 & 0 & f_{9,9} \end{bmatrix} \quad (3.21)$$

where

$$\begin{aligned} f_{1,3} = f_{4,6} = f_{7,9} &= T_s \cdot T + T^2 \cdot (e^{(\frac{-1}{T} \cdot T_s)} - 1) \\ f_{2,3} = f_{5,6} = f_{8,9} &= T \cdot (1 - e^{(\frac{-1}{T} \cdot T_s)}) \\ f_{3,3} = f_{6,6} = f_{9,9} &= e^{(\frac{-1}{T} \cdot T_s)} \end{aligned} \quad (3.22)$$

3.3 Noise Models

The major GPS error sources can be broken down into three categories: Transmitter Errors, Propagation Errors, and Receiver Errors. Traditional GPS transmission errors include orbital estimation errors, clock errors and the effects of Selective Availability (SA). Propagation errors include the effects of the ionosphere and troposphere on the GPS signal, as well as multipath at the receiver site. Receiver error can be attributed to multipath effects and a generic receiver noise (Phase Locked Loop, clock).

For the pseudolite-based positioning system used in this research, orbital estimation and SA effects are not applicable sources of error. Similarly, since the pseudolite signals do not travel through the ionosphere, this source of error is neglected. For carrier-phase signals the pseudolite clock error is assumed to be eliminated by the differencing approach in Section 2.3.2.1.

3.3.1 Tropospheric Delay. The tropospheric delay effect most commonly presented in GPS literature actually reflects the combined effect of the troposphere and stratosphere. The troposphere is defined as the first 10 km above the Earth's surface. The stratosphere is defined as the region just above the troposphere and extends to 60 km [19]. Figure 3.1 portrays the separation of the troposphere and stratosphere.

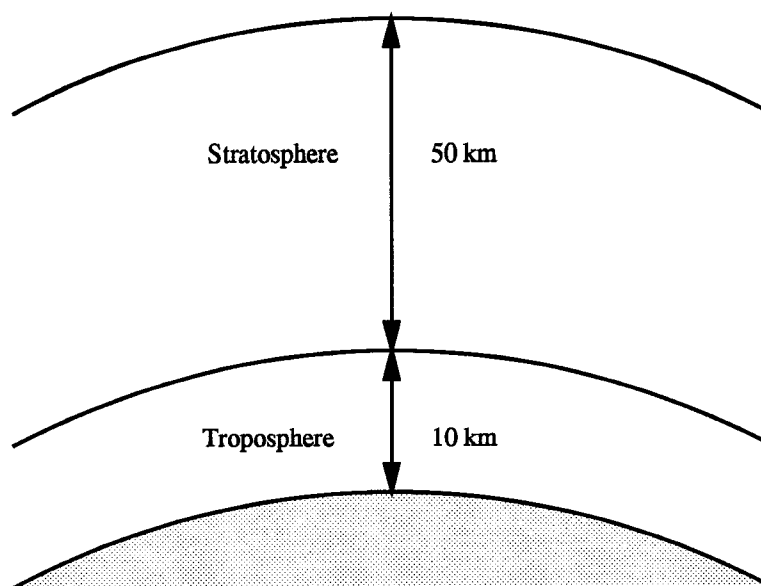


Figure 3.1 Location of Troposphere and Stratosphere

Since most of the water vapor is concentrated in the lower atmosphere, below 10 km, most tropospheric models essentially divide the tropospheric effect into wet and dry effects [16]. The dry component accounts for 80-90% of the total tropospheric delay effect and is predictable within 1% at the zenith point, while the wet component makes up 10-20% of the total tropospheric delay effect and is predictable within 10-20% at the zenith point [19].

There are several tropospheric models used in GPS research [16], including the Saastamoinen, Davis, Goad and Goodman, Yionoulis, Black, Chou, Marini, and others. Difficulties arise in using the traditional GPS tropospheric models in this research, due to the inverted nature of the pseudolite positioning concept. First, the GPS tropospheric models assume that the GPS signal is transmitted from satellites in high orbits. The tro-

ospheric delay is then calculated from the top of the stratosphere to the receiver; in this case, an aircraft flying somewhere in the troposphere. However, the delay term that we are concerned with is between the aircraft and a ground receiver. One might compensate for this by calculating the total delay between the satellite and ground receiver and then subtracting the delay between the satellite and aircraft. Secondly, the tropospheric delay is calculated as a function of the zenith angle. As these zenith angles go beyond $70 - 80^\circ$ many of the GPS tropospheric models attempt to model the curvature of the Earth and consequently overestimate the delay term [16].

3.3.2 Receiver Noise and Multipath Error. An approximation to the strength of receiver noise is to treat 1% of the signal wavelength as white noise [19]. This noise is due to the processing of the signals by the receiver hardware. For example, the GPS L1 carrier is transmitted at 1573.42 MHz, corresponding to a wavelength of 19cm . Thus, the receiver noise in the carrier-phase L1 measurement can be modeled as white noise with a strength of 1.9mm . Similarly, the code phase frequency is 1.023 MHz resulting in a wavelength of 293m and a receiver noise strength of 2.93m .

Multipath effect is caused by the antenna being exposed to reflected signals, causing interference in the receiver [19]. The effect of multipath is highly dependent upon the geographic and cultural features of the receiver site. Several parameters are used to describe the reflection of a signal off the Earth's surface. These include the dielectric constant (Kr_g), conductivity (σ) and, index of refraction ($n = \sqrt{Kr_g}$). The multipath effect is also dependent upon the elevation angle of the pseudolite, θ_c . Figure 3.2 shows the effect of reflection. The critical elevation angle is defined as the angle below which Snell's law predicts reflection. Using Snell's law, the critical angle (θ_c) is determined as:

$$\theta_a = \sin^{-1}\left(\frac{n_a}{n_g}\right) \quad (3.23)$$

$$\theta_c = 90^\circ - \theta_a \quad (3.24)$$

where n_a is the index of refraction of air and n_g is the index of refraction of the ground. Sandy, dry areas, typical of the desert of New Mexico, have an index of refraction $n_g = 3.2$ [19]. The index of refraction of air is defined as $n_a = 1$. Using (3.23) and (3.24), the critical

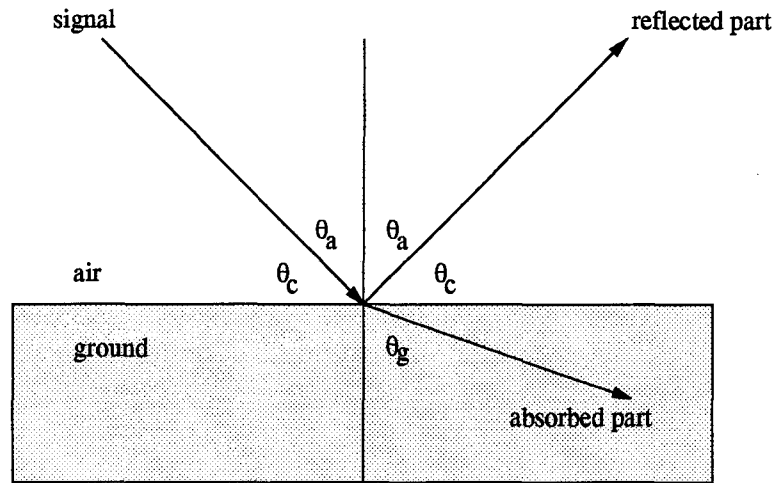


Figure 3.2 Multipath Signal Reflection

elevation angle is determined to be $\theta_c = 71.8^\circ$. Thus, as aircraft flying over the RRS range become closer to the ground and fly farther away from the receivers, they will induce multipath effects at elevation angles less than θ_c . Section 4.2 illustrates the relationship between the flight profile, receiver locations, and geometry concerns (e.g. elevation angles).

3.3.3 Noise Model Implementation. Figure 3.3 is a SIMULINK block diagram of the noise model used in this research. This model outputs the ranging error between a given pseudolite transmitter and receiver. Inputs into the model are a time history of range and elevation angle.

There are three sections of the noise model: the multipath error, receiver noise and tropospheric estimation error. The multipath error and tropospheric estimation error are modeled in this research as first order Markov processes with time constants of 5 seconds and 30 seconds respectively. Receiver noise is customarily modeled as “white” noise. The multipath error model uses the elevation angle as a parameter to scales the multipath range error with the following formula:

$$\begin{cases} 1 - \sin(|\theta_e|), & \text{when } \theta_e \leq 71.8^\circ \\ 0, & \text{when } \theta_e > 90^\circ \end{cases}$$

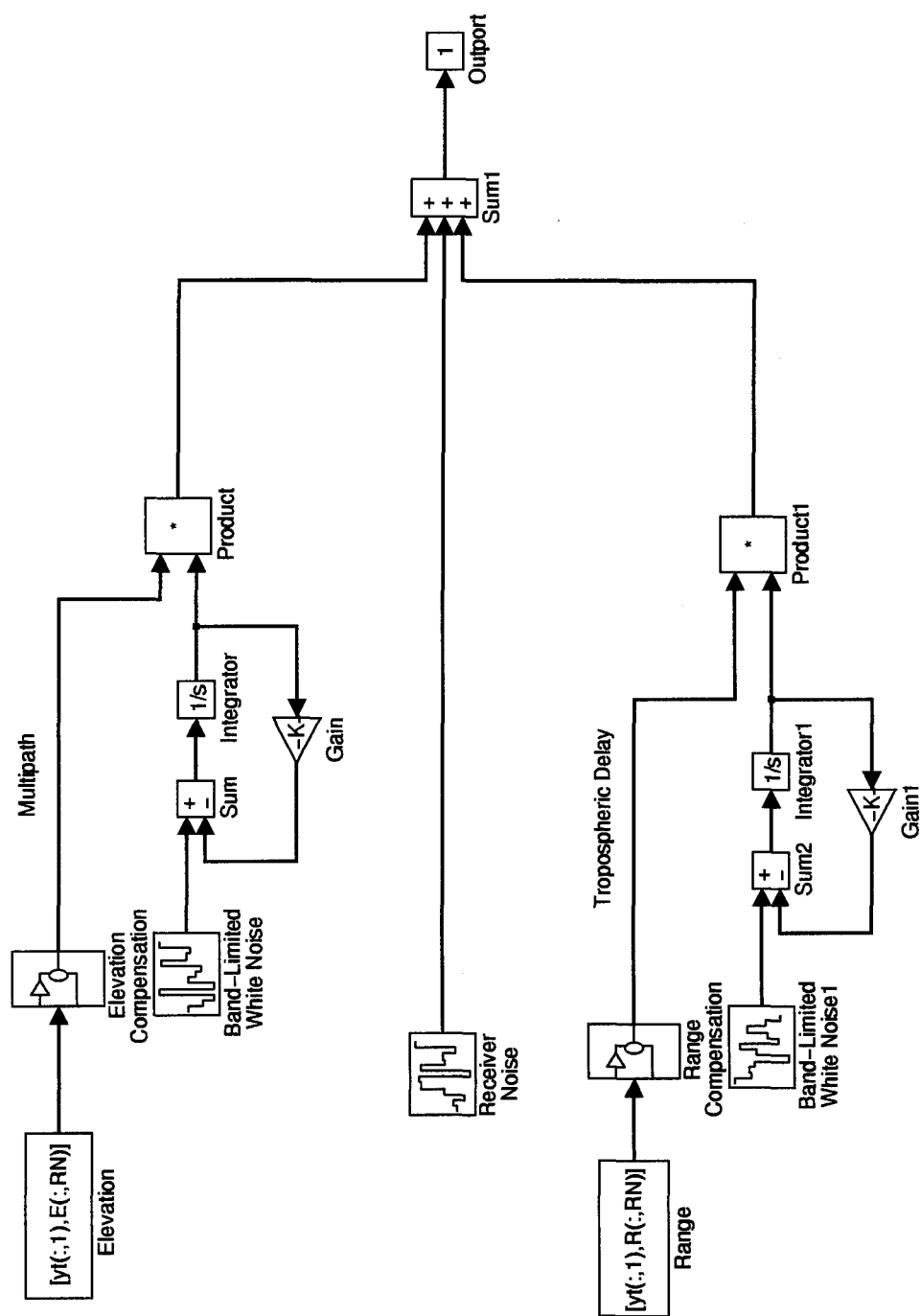


Figure 3.3 Block Diagram of Noise Model

Similarly, the tropospheric estimation error model takes range as a parameter and scales δ_{trop} :

$$\delta_{trop} \cdot \frac{range}{10km} \quad (3.25)$$

such that the error is normalized about the radius of the troposphere, or 10 km.

Two noise models are used in this research. The first model, hereafter referred to as the “colored” noise model, contains tropospheric, multipath and receiver noise error and is described above. The other model is a “white” noise model, where the tropospheric and multipath effects are neglected. The receiver noise strength is increased to achieve an overall 0.1m 3-D RMS position solution.

Fifty realizations of each noise model were generated and saved. This allows both the digital filtering and numerical differentiation approach and Kalman filtering/smoothing approach to share the same noise realizations.

3.4 Digital Filter Design

In this research, the digital filters were synthesized with the use of computer-aided design tools found in MATLAB’s Signal Processing Toolbox. The design procedure involves identifying the following parameters that characterize the performance of a low pass filter:

- R_p = allowed passband loss
- R_s = desired stopband attenuation
- δ_p = allowed passband ripple
- δ_s = allowed stopband ripple
- f_p = desired passband frequency
- f_s = desired stopband frequency

These design parameters are shown in Figure 3.4 The passband includes all positive frequencies up to f_p , the stopband includes all frequencies above f_s , and the transition band is defined as the region between f_p and f_s . For FIR filters, the MATLAB function *remezord* accepts as inputs: f_p , f_s , δ_p and δ_s and returns the parameters required to design the FIR

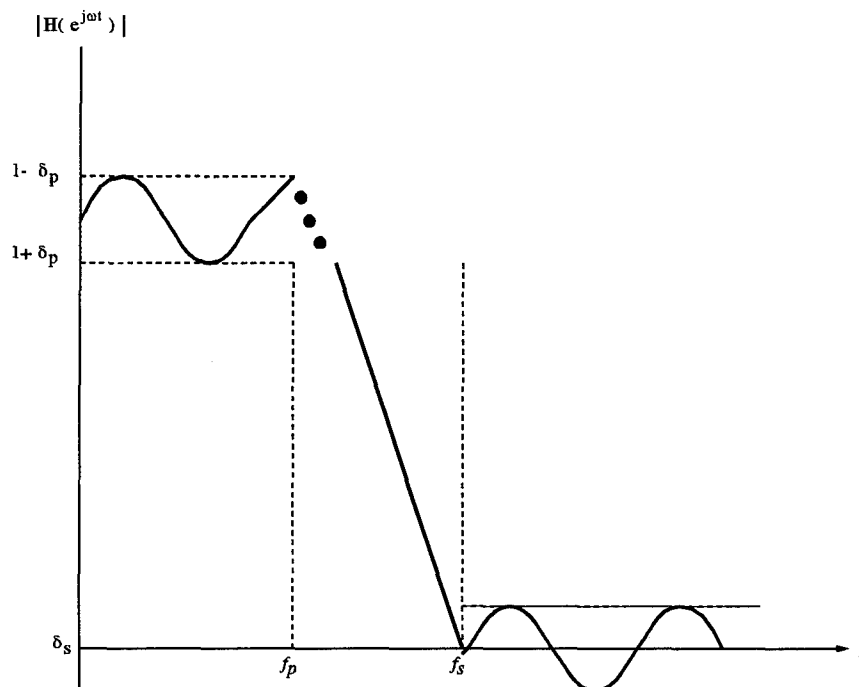


Figure 3.4 Parameters for Filter Design

filter using the well-known Parks-McClellan algorithm. Similarly, IIR filters are designed using MATLAB functions that are capable of generating Butterworth, Chebyshev (I and II) and Elliptic filters. By varying combinations of the parameters R_p , R_s , f_p , f_s , δ_p and δ_s , the filter design is accomplished in an iterative and intuitive manner.

For example, to design the lowest order Chebyshev-I low pass filter whose passband frequency is 0.5, with stopband frequency of 0.8, with no more than 1 dB of loss in the passband, has at least 20 dB attenuation in the stopband, and allows 0.1 dB of passband ripple, one would use the MATLAB commands *cheb1ord* and *cheby1*, as in the following:

```
[N, Wn] = cheb1ord(0.5, 0.8, 1, 20);
[B, A] = cheby1(N, Wn, 0.1);
```

Now the filter is completely described by vectors B and A, representing the numerator and denominator coefficients of the filter transfer function.

IV. Results

4.1 Overview

This chapter presents the results of the development and testing of the two approaches taken in this research: Digital filtering with numeric differentiation and Kalman filtering/smoothing. The chapter begins with a discussion of the aircraft trajectories used in this research.

4.2 Aircraft Trajectory

The software package PROFGEN [32] is used to create the flight profile used in this research. The flight profile is essentially the same used in previous CIGTF-sponsored AFIT thesis research. It is intended to simulate a two-hour mission performed by a high performance multi-role fighter aircraft. Figure 4.1 shows a two dimensional representation of the profile. Figure 4.2 shows the time history of “gees” as experienced by the aircraft, which provides an overall measure of the dynamics of the profile.

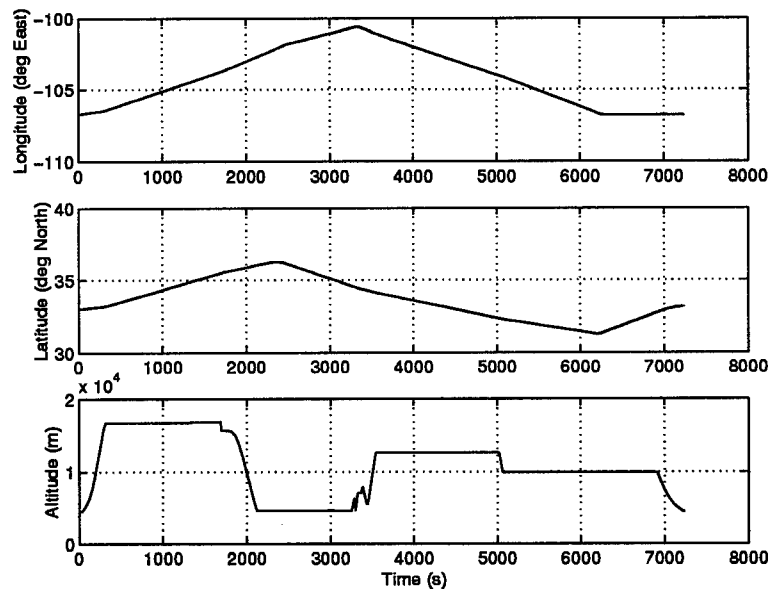


Figure 4.1 2-D View of Flight Profile

Figure 4.3 shows a three-dimensional view of the profile, which is oriented over the CIGTF RRS range. Overlaid on the profile are the locations of the six receiver sites

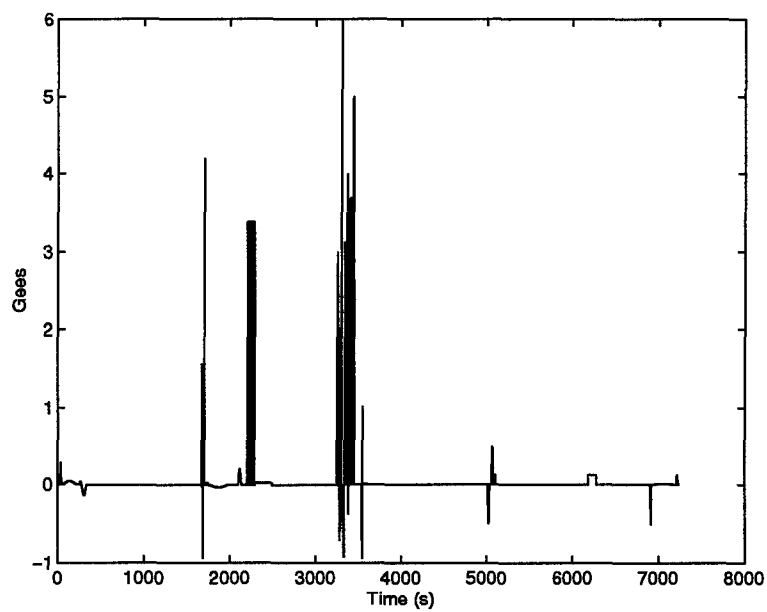


Figure 4.2 Time History of "Gees"

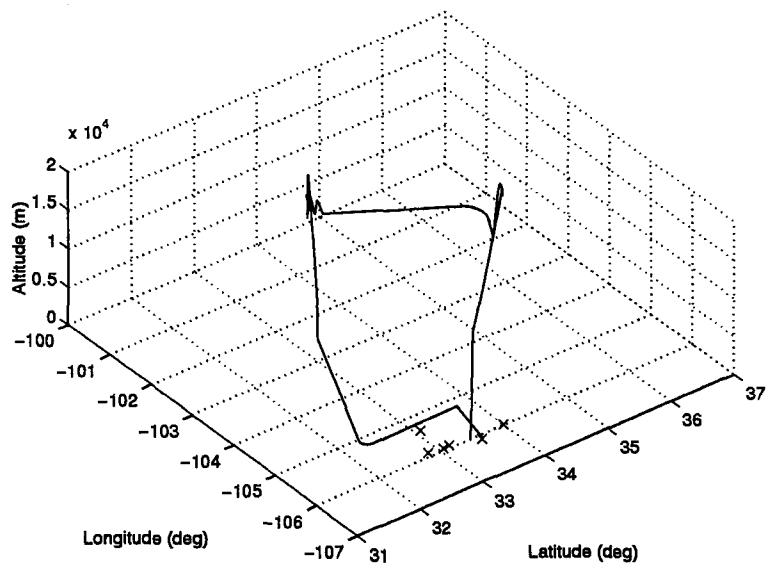


Figure 4.3 3-D View of Flight Profile

considered for this research. Table 4.1 lists the geographic location of the receivers. These receivers are located at existing RRS transponder sites [33], and are not formally optimized for geometry. The position of the receivers relative to the flight profile can also be seen in Figure 4.4.

Table 4.1 Pseudolite Receiver Locations for NRS Simulation

#	Location	Longitude	Latitude	Altitude
R1	Tula PK, NM	33°01.36'	-106°08.20'	1322.53m
R2	TDC, NM	32°55.58'	-106°08.50'	1241.76m
R3	Oscura PK, NM	33°44.58'	-106°22.14'	2417.51m
R4	Salinas, NM	33°17.55'	-106°31.44'	2695.11m
R5	Sac Peak, NM	32°47.16'	-105°49.15'	2804.81m
R6	Twin Buttes, NM	32°42.12'	-106°07.38'	1365.71m

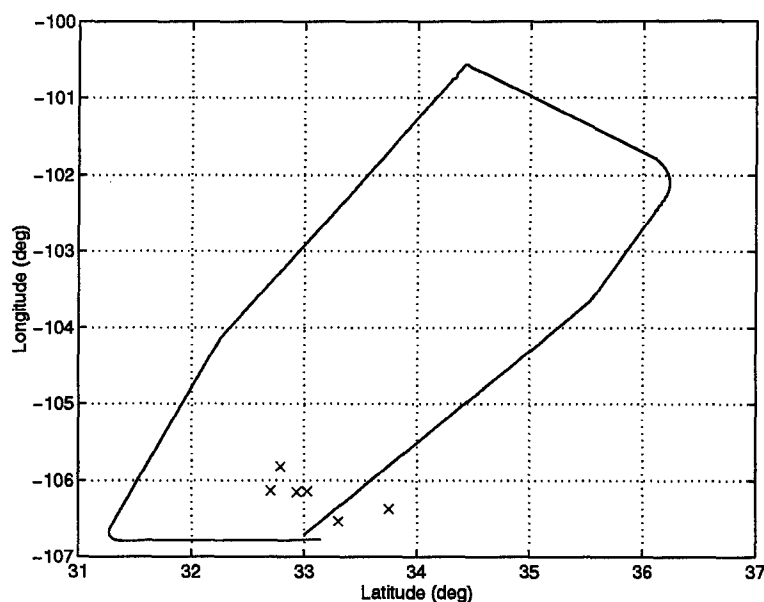


Figure 4.4 Top View of Flight Profile and Receiver Locations

Of concern is the need to keep the configuration of the receivers non-coplanar, to ensure a reasonable three dimensional solution [36]. Furthermore, the ranges and elevation angles between the receivers and the aircraft are of interest, as they effect the tropospheric delay and multipath errors. Figure 4.5 shows the ranges and elevation angles for the flight profile. Notice that the elevation angles are typically below 10 degrees, with the exception

of when the aircraft flies almost directly over the receivers. These low elevation angles are not only good conditions for inducing multipath errors, but also represent an undesirable coplanar receiver configuration.

There is a segment of the trajectory that shows small negative elevation angles. Elevation angle is calculated using a plane tangent to the surface of the Earth as reference. Since altitude is computed as height above the WGS-84 reference ellipsoid, these small negative angles are a result of the aircraft altitude being below the tangent plane extending out over a curved Earth.

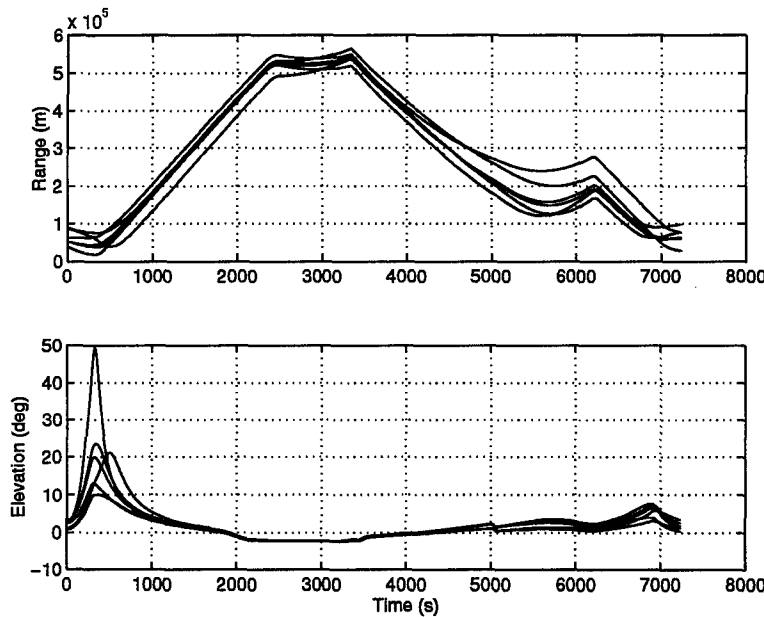


Figure 4.5 Range and Elevation Angles Between Aircraft and Receivers

Another metric for the geometry of receiver locations is to consider the Geometric Dilution of Precision (GDOP). GDOP is a ratio of 3-D position (and time) accuracy to measurement accuracy [18].

GDOP is defined as:

$$GDOP = \sqrt{\text{Tr}\{(A^T \cdot A)^{-1}\}} \quad (4.1)$$

where the matrix A is defined as,

$$A = \begin{bmatrix} Dx_0 & Dy_0 & Dz_0 & Dt_0 \\ Dx_1 & Dy_1 & Dz_1 & Dt_1 \\ \vdots & \vdots & \vdots & \vdots \\ Dx_n & Dy_n & Dz_n & Dt_n \end{bmatrix} \quad (4.2)$$

containing the directional derivatives:

$$Dx_i = \frac{(x_j - x_i)}{\sqrt{(x_j - x_i)^2 + (y_j - y_i)^2 + (z_j - z_i)^2}} \quad (4.3)$$

$$Dy_i = \frac{(y_j - y_i)}{\sqrt{(x_j - x_i)^2 + (y_j - y_i)^2 + (z_j - z_i)^2}} \quad (4.4)$$

$$Dz_i = \frac{(z_j - z_i)}{\sqrt{(x_j - x_i)^2 + (y_j - y_i)^2 + (z_j - z_i)^2}} \quad (4.5)$$

$$Dt_i = 1 \quad (4.6)$$

GDOP is calculated for the entire flight profile using the receiver locations in Table 4.1 and is presented in Figure 4.6. As GDOP grows, the set of equations that must be solved simultaneously to yield position and time become more linearly dependent. Not only does the uncertainty in the solution grow as GDOP becomes large, but in the presence of measurement noise, the existence of a solution is in jeopardy. In practice, acceptable GDOP for a GPS receiver is considered to be an arbitrary value usually below 10. Figure 4.7 shows a portion of the flight segment with reasonable GDOP.

In simulation it is possible to preserve a good GDOP throughout the flight by placing additional receivers along the flight path. A crude, yet effective algorithm was developed to accomplish this. The algorithm monitors GDOP during a flight. If GDOP exceeds a given threshold, a search in a fixed radius around the aircraft locates the site yielding the best improvement in GDOP. The number of receivers used to determine GDOP at one time is fixed, and the addition of a new receiver generally results in the removal of an existing receiver. As receiver sites exceed range or elevation limits, they are removed from consideration as well.

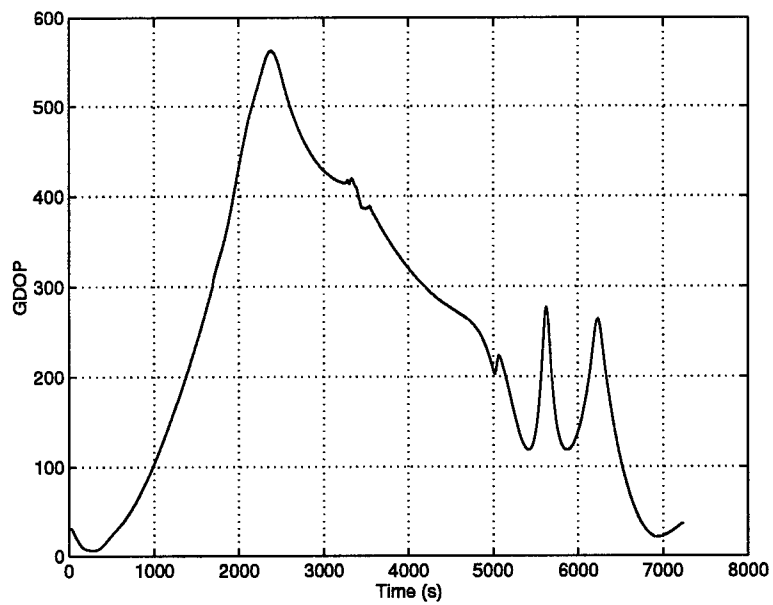


Figure 4.6 GDOP for Entire Flight Profile with Given Receiver Locations

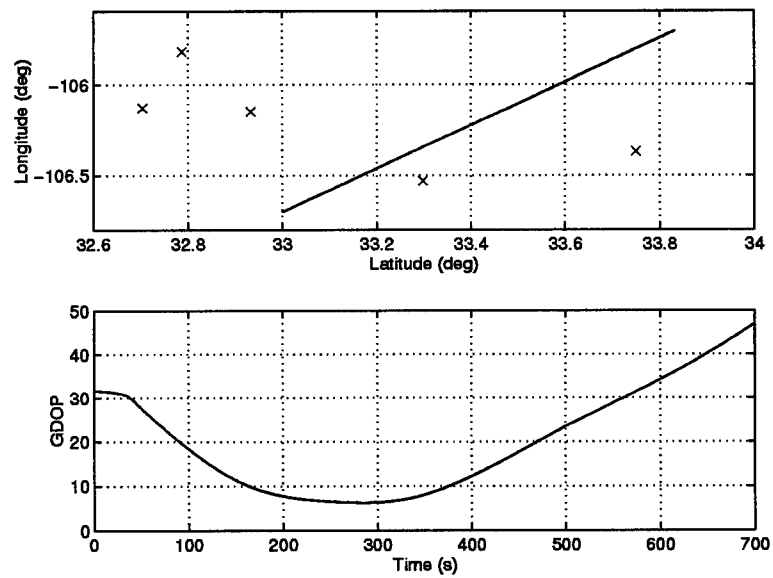


Figure 4.7 Plan View of Flight Profile and GDOP for Truncated Flight Segment

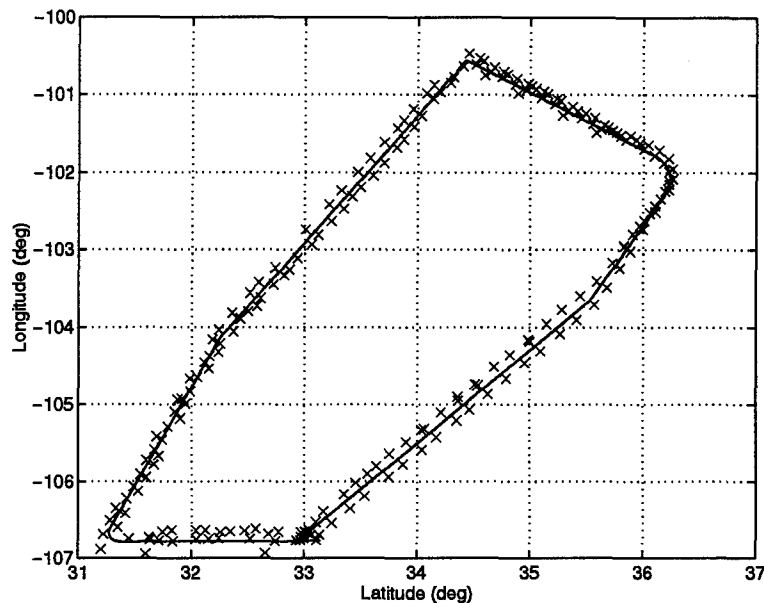


Figure 4.8 Plan View of Receiver Locations Ensuring GDOP < 10

In Figure 4.8 we see the receiver laydown pattern for the entire flight profile. During this flight, receivers were placed such that GDOP was not allowed to exceed 10, as shown in Figure 4.9. The receiver locations are marked with an X. The pattern in Figure 4.8, forms a “racetrack” surrounding the flight profile. The relative proximity of the receiver locations to the flight profile suggests that rather than trying to encompass the entire flight profile with a single set of receivers, a “racetrack” pattern may be a potential strategy for SARS receiver deployment¹. This algorithm is effective in limiting GDOP for simulation purposes yet also provides insight into the real-world geometry problem facing SARS.

4.3 Digital Filtering with Numeric Differentiation

In this section, the validation and results of the digital filtering with numeric differentiation approach are presented. First each of the components of the block diagram are validated for performance. The validation procedure involves benchmarking the compo-

¹The issue of receiver geometry for a realistic flight profile and a reasonable number of receiver sites should be addressed in more detail as an issue of feasibility for the SARS project.

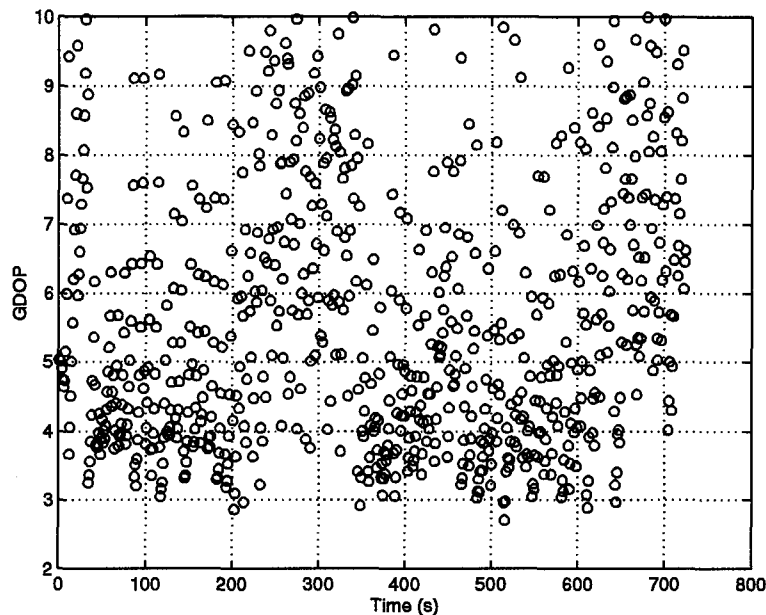


Figure 4.9 GDOP for Entire Flight Profile Using Receiver Locations in Figure 4.8

nents in the absence of noise, in the presence of white noise, and finally in the presence of a more realistic, colored noise.

4.3.1 Analysis of Sampling Rates for Alias Effects. Since the time history of GPS position data is treated as a sampled signal, it is necessary to ensure that the Nyquist sampling criterion is met. A short flight profile was generated that simulated the highest anticipated flight dynamics; minimum radius 9 g s-turns. This flight profile was generated in ECEF coordinates at two sampling rates: 1000 Hz and 10 Hz. The discrete Fourier transform was implemented via MATLAB's built-in Fast Fourier Transform (FFT) routine to examine the frequency spectra of the signal. The flight profile was generated at 1000 Hz to ensure that if any aliasing was present at lower sampling rates, it could be detected.

Figures 4.10 and 4.11 show the frequency spectra for 1000 Hz and 10 Hz respectively. Figure 4.10 verifies that there are no components of the frequency spectra at high frequencies. Similarly at 10 Hz, there is no evidence of frequency components that might suggest aliasing at lower frequencies.

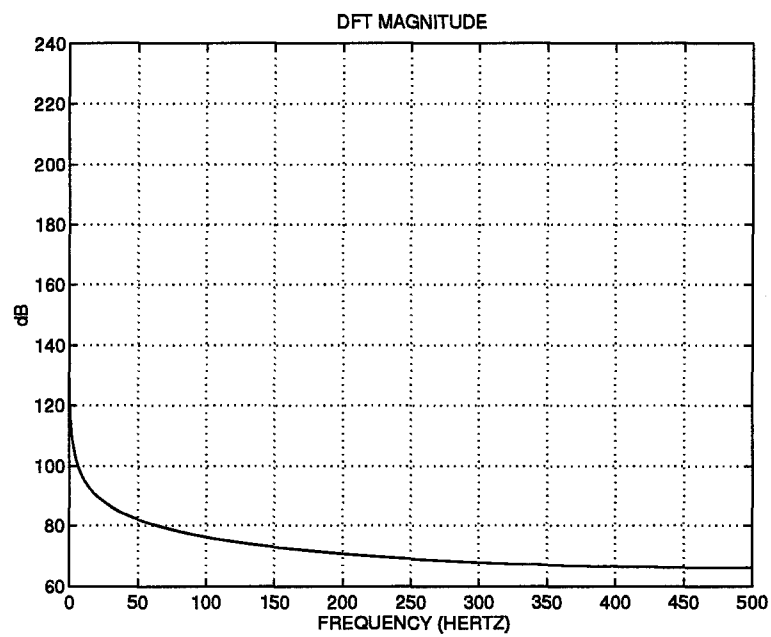


Figure 4.10 Frequency Spectra for Highly Dynamic Flight Trajectory at 1000 Hz

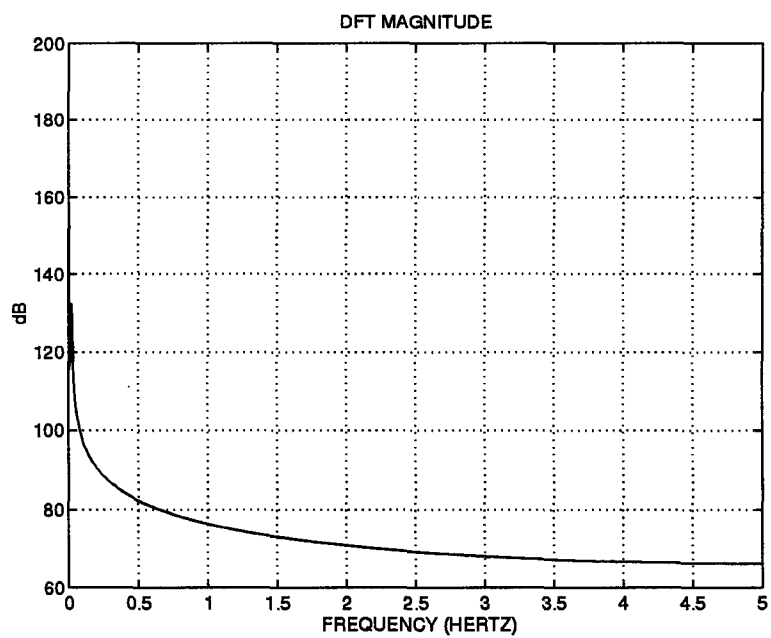


Figure 4.11 Frequency Spectra for Highly Dynamic Flight Trajectory at 10 Hz

4.3.2 Numerical Differentiation Algorithm Performance. Two procedures for determining a numerical derivative were examined. The first procedure involves an extrapolated Taylor's series expansion of the derivative operation as described in Section 2.2.2. The second procedure uses splines to perform a curve fit to the numerical data. An analytical derivative of the equation of the splines, evaluated at the points of interest, gives an approximation to the derivative.

4.3.2.1 Central Difference Equations. The central difference equation approximation for the first derivative is well documented [6,15,22,45] in numerical methods texts. Equations (2.10), (2.11), and (2.12) show the algorithms used in this research.

To test the algorithms, a test signal is defined:

$$r(x) = \sin(x^2), \quad (4.7)$$

which has an exact analytic derivative:

$$r'(x) = 2x \cos(x^2). \quad (4.8)$$

Equations (4.7) and (4.8) are evaluated over the interval $[0, 3\pi]$ at a given sample rate. The numerical derivative is computed and is compared to the exact value determined from (4.8). As expected, (2.12) demonstrates better performance than the other equations in the absence of noise. Figure 4.12 shows the error committed by the first, second and third order central difference equations at a 100 Hz sample rate. We can see from Figure 4.12 that the third order central difference equation shows small errors on the order of 10^{-6} , compared to 10^{-1} and 10^{-3} for the first and second order central difference equations respectively.

The test signal is chosen such that as x increases, the frequency of the test signal sinusoid increases, and the approximation to the derivative worsens. This error is attributed to two factors: the truncation of the higher order terms in the Taylor's series and the nature of the sampled waveform. Truncation establishes the order of magnitude of the error, while the increasing frequency of the signal exposes the error due to sampling.

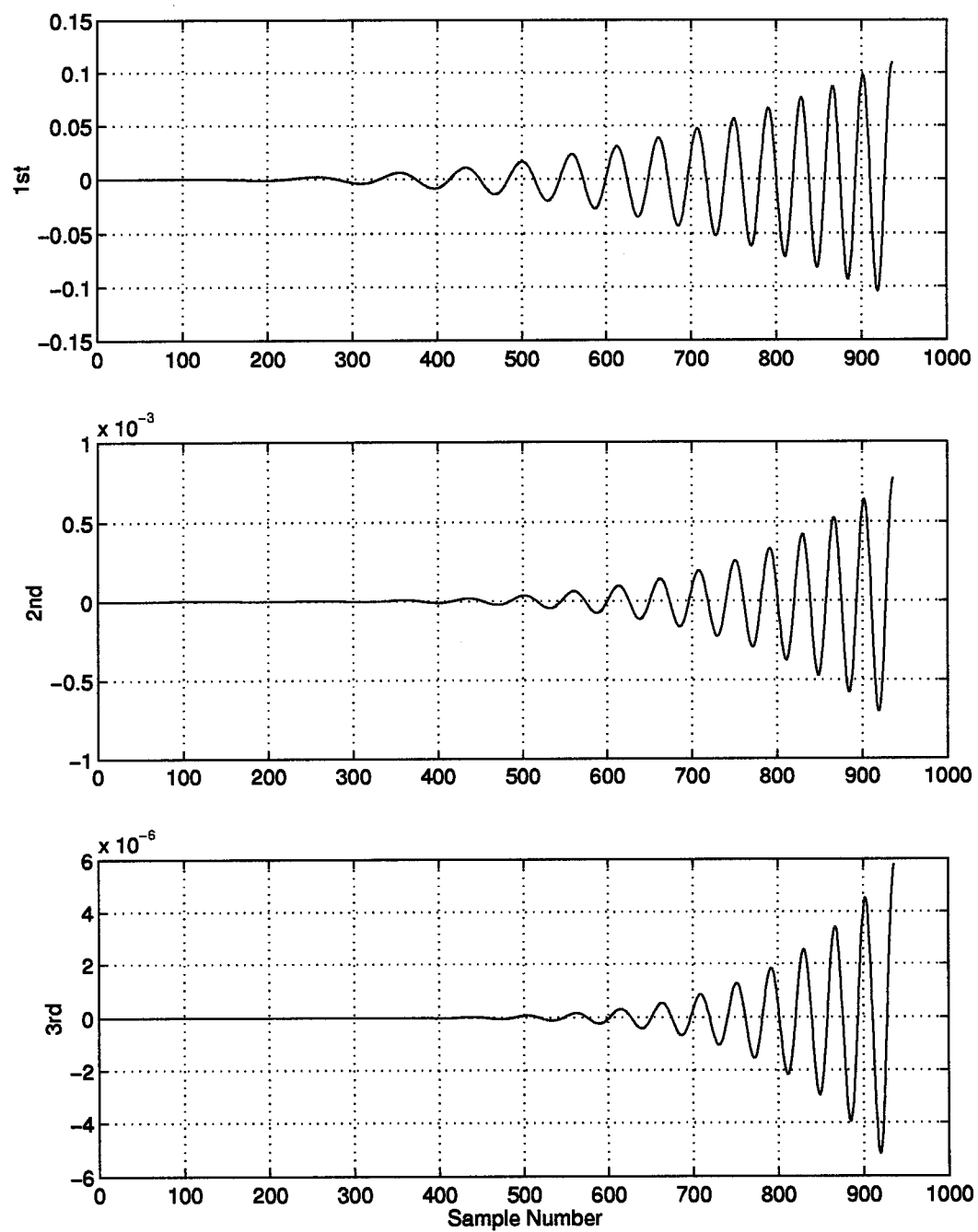


Figure 4.12 Error in Central Difference Approximations in the Absence of Noise

Next we examine the performance of these algorithms under realistic dynamics, as provided by the PROFGEN flight profile. The PROFGEN indicated positions are numerically differentiated using the central difference equations. These computed velocities are compared to the PROFGEN indicated velocities, which are considered to be truth data. See Appendix A for a description of the error metrics used in this research. These results are collected in Table 4.2. As expected, the higher order algorithm provides the best performance at both data rates. Also, as the data rate is increased from 1 Hz to 10 Hz, all of the numerical differentiation algorithms improve.

Direction	Rate	Error (m/s)	1σ (m/s)	Order
3-D RMS	1 Hz	6.125160e-02	4.035006e-01	1st
3-D RMS	1 Hz	1.355792e-02	1.164690e-01	2nd
3-D RMS	1 Hz	8.047649e-03	8.551035e-02	3rd
3-D RMS	10 Hz	6.510429e-04	4.601638e-03	1st
3-D RMS	10 Hz	5.020955e-06	1.171970e-04	2nd
3-D RMS	10 Hz	1.301999e-06	5.134946e-05	3rd

Table 4.2 Performance of Numeric Differentiators Using Flight Profile

Figure 4.13 shows the 3-D RMS error of the third order numerical differentiator for a 10 Hz data rate. This plot shows large “spikes” of error at specific time intervals, which are correlated in time to the highly dynamic portions of the flight trajectory as seen in Figure 4.2. While the magnitudes of the spikes in Figure 4.13 vary for the different numerical differentiation algorithms and data rates, the location of these “spikes” remains consistent.

We would then expect better performance of the numerical differentiation routines during periods of low dynamics. Table 4.3 shows the numeric differentiator performance over a segment of the flight profile with benign dynamics ($t = 0$ to 100 seconds). Comparing Tables 4.2 and 4.3 we see a 93%-98% improvement in 3-D RMS error.

While it is worthwhile to consider the performance of these numerical differentiators in the absence of noise, we can also determine the performance of each algorithm in the presence of corrupting noise. Two types of noise corruption are employed. One is a simulation of “white” Gaussian noise, while the other is a combination of white and time correlated noise, hereafter referred to as “colored” Gaussian noise. The each noise type is

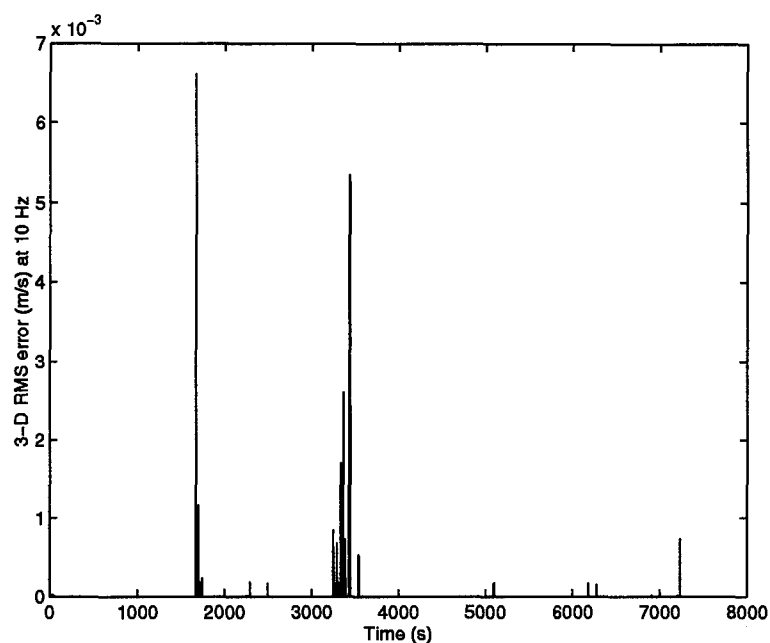


Figure 4.13 Error in 3rd Order Numerical Derivative Using Flight Profile at 10 Hz

Direction	Rate	Mean Error (m/s)	1σ (m/s)	Order
3-D RMS	1 Hz	4.106344e-03	1.386701e-02	1st
3-D RMS	1 Hz	2.907217e-04	3.474643e-03	2nd
3-D RMS	1 Hz	1.330864e-04	2.321516e-03	3rd
3-D RMS	10 Hz	4.145871e-05	1.418019e-04	1st
3-D RMS	10 Hz	2.859088e-07	1.245242e-05	2nd
3-D RMS	10 Hz	1.123711e-07	7.592645e-06	3rd

Table 4.3 Performance of Numeric Differentiators Using Benign Flight Profile

tuned to provide an overall 0.1 *m* 3-D RMS 1σ error in position as described in Section 3.3.3.

Direction	Rate	Mean Error Colored (m/s)	1σ (m/s)	Mean Error White (m/s)	1σ (m/s)	Order
3-D RMS	1 Hz	4.033391e-01	9.760447e-03	4.568517e-01	3.114718e-02	1st
3-D RMS	1 Hz	5.264175e-01	1.240445e-02	5.284405e-01	4.333967e-02	2nd
3-D RMS	1 Hz	5.949750e-01	1.387963e-02	5.467742e-01	5.120870e-02	3rd
3-D RMS	10 Hz	6.300444e-02	4.476222e-03	9.252125e-02	8.219554e-01	1st
3-D RMS	10 Hz	6.256138e-02	5.565853e-03	1.231328e-01	1.114507e+00	2nd
3-D RMS	10 Hz	6.930055e-02	5.707011e-03	1.449810e-01	1.306353e+00	3rd

Table 4.4 Performance of Numeric Differentiators in the Presence of Noise Using Benign Flight Profile

The results in Table 4.4 show the performance of the three central difference equation algorithms in the presence of noise, for a 50 Monte Carlo run simulation. For both the 1 Hz and 10 Hz data rates the benefit of using the higher order differentiators is no longer evident. In fact, at 1 Hz the higher order differentiators show a 14% to 47% increase in 3-D RMS error compared to the first order equation. At 10 Hz, the second order differentiator slightly outperforms the first order algorithm for the case of colored noise. However, in all other cases at 10 Hz, the first order differentiator provides the best performance.

4.3.2.2 Differentiation Using Cubic Splines. Another method of approximating a derivative is to determine a closed form expression for a curve that fits the data to be operated on. An analytic derivative is taken of the curve and then evaluated at the points of interest to generate the derivative approximation. While there are many curve fitting methods available, cubic splines handle large sets of data points well and guarantees continuous derivatives over the entire data set [15,45]. As in the previous section, (4.7) and (4.8) are evaluated for $x = 0$ to 3π at a given sample rate. The derivative is approximated using cubic splines and is compared to the exact value determined from (4.8). Comparing Figures 4.12 and 4.14 shows the cubic spline derivative performing between the second and third order numerical differentiators.

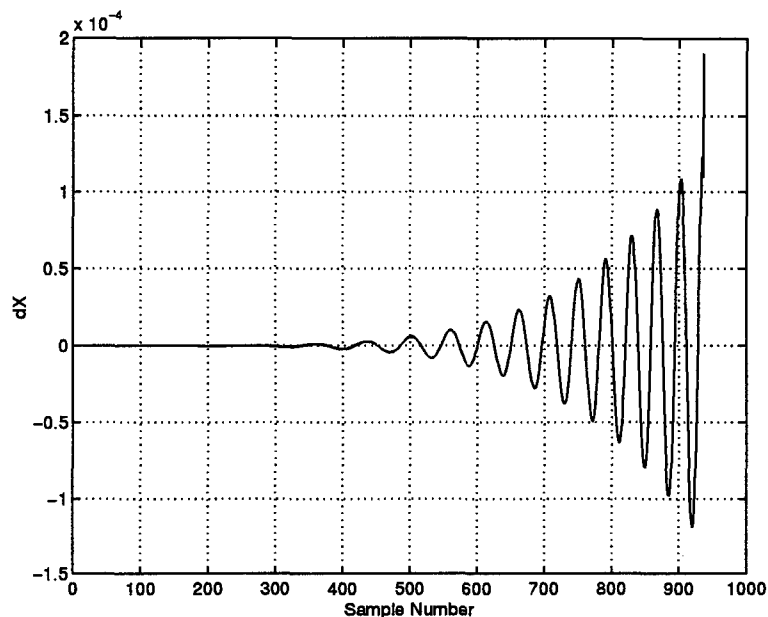


Figure 4.14 Error in Cubic Spline Derivative in the Absence of Noise

As with the numerical differentiators, it is of interest to examine the performance of the cubic spline method under a realistic flight profile. The cubic spline method shows significant improvement in velocity accuracy as the data rate increases from 1 Hz to 10 Hz. Also, under this realistic flight profile, the cubic spline method slightly outperforms the third order numerical differentiator. The results of the cubic spline differentiator are tabulated in Table 4.5. In Figure 4.15 the 3-D RMS error of the cubic spline differentiator for 10 Hz is shown. The location and magnitude of the large spikes compares favorably to what is shown in Figure 4.13 as well as the aircraft dynamics shown in Figure 4.2.

We can also compare the performance of the cubic spline differentiator to the numerical differentiation routine, within the benign portion of the flight profile. The performance advantage of the cubic spline method is easily seen by comparing Tables 4.3 and 4.5. The cubic spline differentiator shows an improvement over the third order central difference equation in 3-D RMS error of 64% and 84% for 1 Hz and 10 Hz data rates respectfully.

Cubic spline differentiation can also be applied to noisy signals. To accommodate noise, a smoothing parameter, $p \in [0 \cdots 1]$, is introduced. For $p = 0$, the cubic spline algorithm performs a least-squares straight line fit to the data. For $p = 1$, the natural

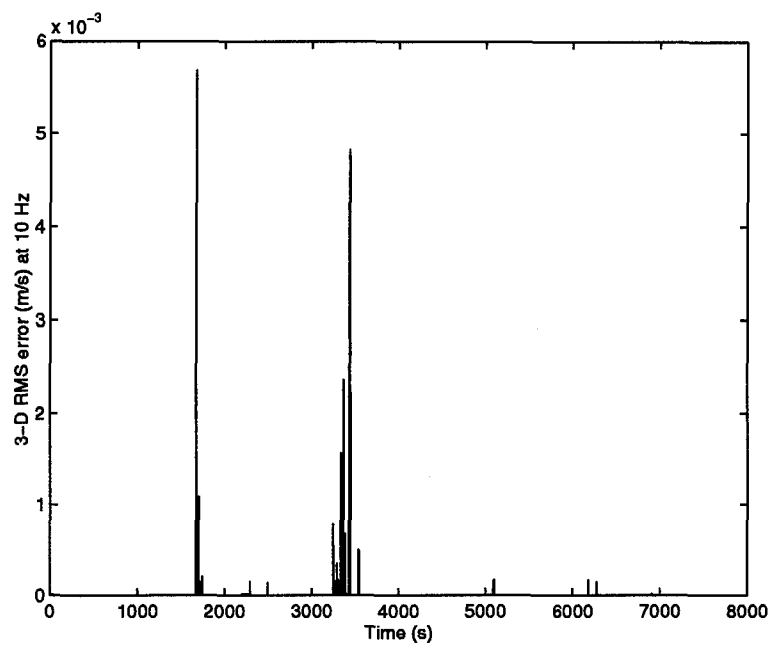


Figure 4.15 Error in Cubic Spline Derivative Using Flight Profile at 10 Hz

Direction	Rate	Mean Error (m/s)	1σ (m/s)	Profile
3-D RMS	1 Hz	7.373304e-03	7.608367e-02	Entire
3-D RMS	10 Hz	1.345184e-06	4.488712e-05	Entire
3-D RMS	1 Hz	4.702409e-05	4.779469e-04	Truncated
3-D RMS	10 Hz	1.767529e-08	1.428987e-07	Truncated

Table 4.5 Performance of Cubic Spline Differentiator in the Absence of Noise

cubic spline fit is performed. As p moves from 0 to 1, the cubic spline algorithm changes from one extreme to the other. The smoothing parameter is in general arbitrarily chosen. In this case, $p = 0.85$ yielded the best performance.

Direction	Rate	Mean Error Colored (m/s)	1σ (m/s)	Mean Error White (m/s)	1σ (m/s)	Smoothing Parameter
3-D RMS	1 Hz	5.241575e-02	4.872613e-03	9.304974e-02	7.544461e-03	0.85
3-D RMS	10 Hz	8.828444e-02	6.173212e-03	8.130258e-02	5.698531e-03	0.85

Table 4.6 Performance of Cubic Smoothing Spline Differentiators in the Presence of Noise Using Benign Flight Profile

Table 4.6 shows the performance of the cubic spline differentiator in the presence of noise. Comparing the cubic spline differentiator results to the central difference equation differentiator results of Table 4.4 favors the cubic spline differentiator. Except for the case of colored noise at 10 Hz, the cubic spline yields lower 3-D RMS errors by 40% to 80%.

4.3.3 Digital Filter Results. In order to validate the performance of the digital filters used in this research, we first examine what penalty, if any, results from their use. For example, filter cutoff frequencies must be chosen to eliminate as much noise as possible, while preserving the true underlying signal. To do this, we apply low pass filters to both noisy and noiseless signals, and observe the results. In both cases, the difference between the original, noiseless signal and the filtered signal is the error we wish to quantify.

4.3.3.1 IIR Filter Performance. Four types of IIR filters were examined: Chebyshev I, Chebyshev II, Butterworth and Elliptic. The filters were evaluated for performance at data rates of 1 Hz and 10 Hz using the truncated flight profile. The filter design parameters were adjusted by trial and error for each filter type to achieve it's "best" performance.

Table 4.7 lists the design parameters and resulting filter order used for each of the filter designs. The passband frequencies (f_p) and stopband frequencies (f_s) are given in normalized frequency (0 to 1), the allowable passband ripple (δ_p) and desired stopband attenuation (δ_s) are given in decibels. These design parameters are used to describe the

desired properties of a low pass filter, which is synthesized using MATLAB as described in Section 3.4.

Type	$R_p(dB)$	$R_s(dB)$	f_p	f_s	δ_p (dB)	δ_s (dB)	order
Chebyshev-I	1e-07	40	0.55	0.8	1e-07	-	9
Chebyshev-II	1e-07	20	0.55	0.75	-	1e-07	8
Butterworth ²	1e-07	30	0.55	0.8	-	-	13
Elliptical	1e-07	40	0.55	0.8	1e-07	-	7

Table 4.7 IIR Filter Design Parameters and Resulting Filter Order

The Butterworth filter designed using parameters similar to the other IIR filters was unstable. Since the Chebyshev (I and II) and Elliptic filters would provide better performance than a reduced order Butterworth, the Butterworth filter was removed from consideration. Table 4.8 shows the results of applying the three types of filters to noiseless position data at 1 Hz and 10 Hz rates respectively. The Elliptic filter trails the performance of the Chebyshev filters, with the Chebyshev-II filter yielding the best performance.

Direction	Filter Type	Rate	Mean Error (m)
3-D RMS	Chebyshev-I	1 Hz	4.112376e-02
3-D RMS	Chebyshev-II	1 Hz	1.058158e-03
3-D RMS	Elliptic	1 Hz	9.470536e-02
3-D RMS	Chebyshev-I	10 Hz	3.677020e-04
3-D RMS	Chebyshev-II	10 Hz	1.521616e-04
3-D RMS	Elliptic	10 Hz	8.528341e-04

Table 4.8 Performance of IIR Filters in the Absence of Noise

The performance of the IIR filters in the presence of noise is displayed in Table 4.9. Tests were performed at 1 Hz and 10 Hz data rates with both white noise and colored noise models. Although the Chebyshev-II filter gave the best results in the absence of noise, the Chebyshev-I filter outperformed all other filters except for the case of colored noise at 1 Hz. The fact remains, however, that the prefilter is unable to significantly reduce the amount of noise in the position signal before numerical differentiation takes place.

²Unstable filter

Direction	Filter Type	Rate	Mean Error (m)	Noise
3-D RMS	Chebyshev-I	1 Hz	1.387863e-01	White
3-D RMS	Chebyshev-II	1 Hz	1.432184e-01	White
3-D RMS	Elliptic	1 Hz	1.810501e-01	White
3-D RMS	Chebyshev-I	10 Hz	1.173286e-01	White
3-D RMS	Chebyshev-II	10 Hz	1.368191e-01	White
3-D RMS	Elliptic	10 Hz	1.190525e-01	White
3-D RMS	Chebyshev-I	1 Hz	1.883719e-01	Colored
3-D RMS	Chebyshev-II	1 Hz	1.692749e-01	Colored
3-D RMS	Elliptic	1 Hz	2.291981e-01	Colored
3-D RMS	Chebyshev-I	10 Hz	1.384984e-01	Colored
3-D RMS	Chebyshev-II	10 Hz	1.413331e-01	Colored
3-D RMS	Elliptic	10 Hz	1.390585e-01	Colored

Table 4.9 Performance of IIR Filters in the Presence of Noise

4.3.3.2 FIR Filter Performance. While the IIR prefilter was able to reduce the overall error, albeit slightly, an FIR filter could not be designed to meet the performance requirements. The MATLAB routine *remezord* was used to implement an FIR filter with the characteristics seen in Table 4.10. Comparing Tables 4.7 and 4.10, the order of the FIR

Type	$R_p(dB)$	$R_s(dB)$	f_p	f_s	$\delta_p(dB)$	$\delta_s(dB)$	order
FIR	1e-07	-	0.55	0.8	-	1e-07	68
FIR	1e-07	-	0.55	0.75	-	1e-07	85

Table 4.10 FIR Filter Design Parameters and Resulting Filter Order

filter is extremely high compared to that of the IIR filter. This high filter order results in an unacceptable transient response as the filter requires as many as 85 samples to reach it's optimal performance. For this reason the FIR filter was dismissed as a potential prefilter or postfilter candidate.

4.3.4 Post-Filter Design. Considering the results of Section 4.3.3, the Post-Filter was designed as a Chebyshev-I low pass filter. Since the Chebyshev-I showed only a marginally better improvement over other IIR filter types for the prefilter, an extensive analysis was not completed for the postfilter. The following parameters for the Chebyshev-I filter were found to give the best results for the overall system: The results for the overall

Type	f_p	f_s	δ_p (dB)	δ_s (dB)	order	Data rate
Chebyshev-I	0.25	0.55	1e-04	80	10	1 Hz
Chebyshev-I	0.04	0.13	1e-04	80	10	10 Hz

Table 4.11 IIR Post-Filter Design Parameters and Resulting Filter Order

system follow in Section 4.3.5

4.3.5 Overall Results. In this section, results are presented for the overall numerical methods and digital filtering approach. Figure 4.16 depicts the overall approach involving a prefiltering stage, a numerical differentiator and a postfiltering stage. The

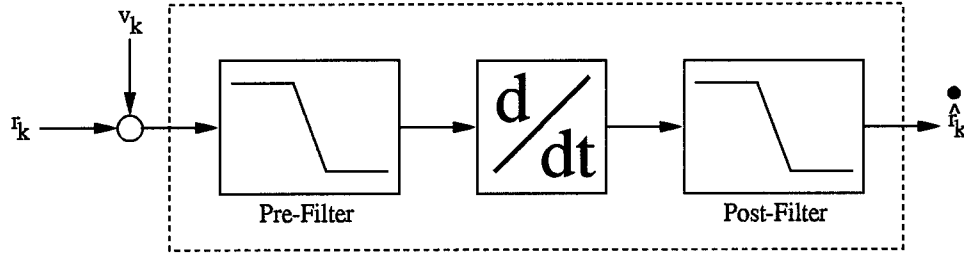


Figure 4.16 Overall Block Diagram for Digital Filtering Approach

prefilter and numerical differentiator performance has been validated in Sections 4.3.3 and 4.3.2. Based upon these results, the overall system is implemented using the Chebyshev-I low pass filter and the cubic smoothing spline differentiator. The post filter design parameters are presented in Table 4.11.

Direction	Rate	Mean Error Colored (m/s)	1σ (m/s)	Mean Error White (m/s)	1σ (m/s)	Order
3-D RMS	1 Hz	6.972119e-02	6.267176e-03	5.336845e-02	1.080036e-02	1st
3-D RMS	1 Hz	6.982697e-02	6.256767e-03	5.354084e-02	1.079336e-02	2nd
3-D RMS	1 Hz	7.859507e-02	1.151028e-02	7.456002e-02	2.329147e-02	3rd
3-D RMS	1 Hz	6.841166e-02	6.844996e-03	6.943656e-02	6.512700e-03	Cubic
3-D RMS	10 Hz	6.608933e-02	4.165794e-03	7.414128e-02	5.083268e-03	1st
3-D RMS	10 Hz	6.015083e-02	5.208232e-03	7.061738e-02	5.517326e-03	2nd
3-D RMS	10 Hz	6.239051e-02	5.323950e-03	7.479032e-02	6.179847e-03	3rd
3-D RMS	10 Hz	5.262775e-02	4.734819e-03	6.263966e-02	5.993183e-03	Cubic

Table 4.12 Overall Performance in the Presence of Noise Using Benign Flight Profile

The overall performance of the approach of digital filtering with numeric differentiation is summarized in Table 4.12. The results show a slight advantage with the higher data rate of 10 Hz. The cubic spline algorithm demonstrates the best overall performance, including meeting the specifications of 0.005 m/s 3-D RMS 1σ for the case of colored noise at 10 Hz.

4.4 Kalman Filtering/Smoothing

This section presents the results of the Kalman Filtering/Smoothing approach. Three different filter models are examined: a constant velocity model, a constant acceleration model and a constant acceleration with noise modeled as a first order Markov process. Each model is run at 1 Hz and 10 Hz. The benefits of smoothing as opposed to just filtering are presented.

The flight profile used is the same benignly dynamic trajectory used for the digital filtering and numeric differentiation approach. The trajectory shows the initial climb to altitude associated with a takeoff. The ECEF X,Y, and Z velocities are shown in Figure 4.17. After 50 seconds, the aircraft levels off and assumes a true constant velocity in all

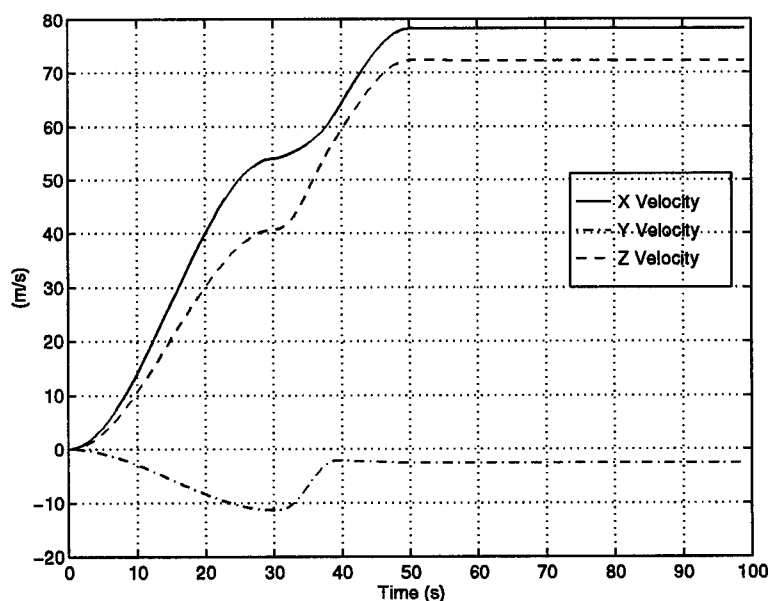


Figure 4.17 X, Y, and, Z Velocities for Benign Flight Trajectory

directions. Performance is evaluated for the entire 100 second segment as well as for the last 45 seconds which guarantees a true constant velocity.

4.4.1 Constant Velocity Model. The results of the Constant Velocity Kalman filter/smoothing model described in Section 3.2.1 are shown in Tables 4.13 and 4.14. Table 4.13 shows the 3-D RMS error and 1σ of the Kalman filter/smoothing in the truncated flight segment. It is interesting to see that the Kalman filter and smoother showed better results at 1 Hz rather than 10 Hz.

Direction	Rate	Error (m/s)	1σ (m/s)	Filter Type	Noise Type
3-D RMS	1 Hz	1.513682e-02	1.519563e-02	Filter	White
3-D RMS	1 Hz	8.156500e-03	6.732130e-03	Smoother	White
3-D RMS	1 Hz	9.072810e-03	7.198723e-03	Filter	Colored
3-D RMS	1 Hz	6.706086e-03	4.728951e-03	Smoother	Colored
3-D RMS	10 Hz	4.502794e-01	1.226147e-01	Filter	White
3-D RMS	10 Hz	2.784655e-02	2.200576e-02	Smoother	White
3-D RMS	10 Hz	2.307511e-01	3.527986e-01	Filter	Colored
3-D RMS	10 Hz	3.682011e-02	2.988482e-02	Smoother	Colored

Table 4.13 Constant Velocity Model Using Truncated Flight Profile

When considering the entire benign trajectory we must “open up the bandwidth” of the filter. Essentially the non-constant velocities of the input data result in the kinematic model being invalid. To tell the filter to rely more on the measurements than its internal model, we increase the magnitude of the dynamics driving noise, Q . In this case, the results for the 1 Hz and 10 Hz data are very similar. Tuning plots for the position and velocity states are shown in Appendix B.

4.4.2 Constant Acceleration Model. The results of the constant acceleration Kalman filter/smoothing model described in Section 3.2.2 are shown in Tables 4.15 and 4.16. Table 4.15 shows the 3-D RMS error and 1σ of the Kalman filter/smoothing in the truncated flight segment.

As with the constant velocity model, the Kalman filter dynamics driving noise is increased to compensate for the dynamics model inadequacies. These results are shown in Table 4.16. Tuning plots for the position and velocity states are shown in Appendix C.

Direction	Rate	Error (m/s)	1σ (m/s)	Filter Type	Noise Type
3-D RMS	1 Hz	2.902978e-01	5.130680e-01	Filter	White
3-D RMS	1 Hz	6.008015e-02	4.753936e-02	Smoother	White
3-D RMS	1 Hz	1.212918e-01	1.302018e-01	Filter	Colored
3-D RMS	1 Hz	2.813343e-02	2.249046e-02	Smoother	Colored
3-D RMS	10 Hz	9.530139e-01	1.982058e+00	Filter	White
3-D RMS	10 Hz	2.477768e-02	2.267867e-02	Smoother	White
3-D RMS	10 Hz	8.852748e-01	1.393025e+00	Filter	Colored
3-D RMS	10 Hz	3.682874e-02	2.981835e-02	Smoother	Colored

Table 4.14 Constant Velocity Model Using Entire Benign Flight Profile

Direction	Rate	Error (m/s)	1σ (m/s)	Filter Type	Noise Type
3-D RMS	1 Hz	3.372428e-02	2.795790e-02	Filter	White
3-D RMS	1 Hz	1.079198e-02	9.758075e-03	Smoother	White
3-D RMS	1 Hz	2.198128e-02	1.742112e-02	Filter	Colored
3-D RMS	1 Hz	1.077930e-02	8.012129e-03	Smoother	Colored
3-D RMS	10 Hz	1.041561e-02	1.172789e-02	Filter	White
3-D RMS	10 Hz	3.921000e-03	4.031051e-03	Smoother	White
3-D RMS	10 Hz	2.585014e-02	1.957010e-02	Filter	Colored
3-D RMS	10 Hz	1.389758e-02	9.936714e-03	Smoother	Colored

Table 4.15 Constant Acceleration Model Using Truncated Flight Profile

Direction	Rate	Error (m/s)	1σ (m/s)	Filter Type	Noise Type
3-D RMS	1 Hz	1.618147e-01	1.582101e-01	Filter	White
3-D RMS	1 Hz	4.853251e-02	3.832201e-02	Smoother	White
3-D RMS	1 Hz	7.861218e-02	7.368700e-02	Filter	Colored
3-D RMS	1 Hz	2.681462e-02	2.147360e-02	Smoother	Colored
3-D RMS	10 Hz	2.361016e-01	5.188239e-01	Filter	White
3-D RMS	10 Hz	1.518371e-02	1.315073e-02	Smoother	White
3-D RMS	10 Hz	1.180761e-01	1.284944e-01	Filter	Colored
3-D RMS	10 Hz	3.151422e-02	2.514358e-02	Smoother	Colored

Table 4.16 Constant Acceleration Model Using Entire Flight Profile

4.4.3 *Constant Acceleration with Markov Process Model.* The results of the constant acceleration Kalman filter/smoothing model with noise modeled as a 1st order Markov process described in Section 3.2.3 are shown in Tables 4.17 and 4.18. Table 4.17 shows the 3-D RMS error and 1σ of the Kalman filter/smoothing in the truncated flight segment.

Direction	Rate	Error (m/s)	1σ (m/s)	Filter Type	Noise Type
3-D RMS	1 Hz	1.438570e-02	1.443129e-02	Filter	White
3-D RMS	1 Hz	7.010042e-03	6.366674e-03	Smoothing	White
3-D RMS	1 Hz	1.051723e-02	8.653171e-03	Filter	Colored
3-D RMS	1 Hz	7.704391e-03	5.347301e-03	Smoothing	Colored
3-D RMS	10 Hz	5.640125e-03	8.993274e-03	Filter	White
3-D RMS	10 Hz	2.622584e-03	3.179606e-03	Smoothing	White
3-D RMS	10 Hz	1.125054e-02	8.307786e-03	Filter	Colored
3-D RMS	10 Hz	9.955190e-03	6.872084e-03	Smoothing	Colored

Table 4.17 Constant Acceleration Model with Markov Process Using Truncated Flight Profile

As with the previous models, the dynamics driving noise, Q , is increased in order to achieve satisfactory performance. Tuning plots for the position and velocity states are shown in Appendix D.

Direction	Rate	Error (m/s)	1σ (m/s)	Filter Type	Noise Type
3-D RMS	1 Hz	1.964303e-01	2.241990e-01	Filter	White
3-D RMS	1 Hz	4.448769e-02	3.508846e-02	Smoothing	White
3-D RMS	1 Hz	1.205297e-01	1.247135e-01	Filter	Colored
3-D RMS	1 Hz	2.643877e-02	2.122642e-02	Smoothing	Colored
3-D RMS	10 Hz	3.652743e-01	8.777798e-01	Filter	White
3-D RMS	10 Hz	1.626416e-02	1.427469e-02	Smoothing	White
3-D RMS	10 Hz	1.244843e-01	1.315372e-01	Filter	Colored
3-D RMS	10 Hz	3.386609e-02	2.725365e-02	Smoothing	Colored

Table 4.18 Constant Acceleration Model with Markov Process Using Entire Flight Profile

4.5 Summary

This chapter presented the results of two distinct approaches to calculating a reference velocity from discrete, noisy position data: a digital filtering and numeric differentiation approach and a Kalman filtering/smoothing approach. Performance for each approach is measured at data rates of 1 Hz and 10 Hz, with a white noise model and a “colored” noise model.

The results of these simulations are encouraging. The performance specification of 0.005 m/s 3-D RMS 1σ was achieved by both approaches, although not for every case. The digital filtering and numeric differentiation method tolerated changes in dynamics better than the Kalman filter/smoother, while the latter showed excellent performance when its internal dynamics model was well matched with the incoming data.

V. Conclusions and Recommendations

5.1 Overview

This chapter presents the conclusions derived from this thesis research concerning two different approaches to determining velocity for an inverted pseudolite-based navigation reference system: a digital filtering with numeric differentiation approach and a kinematic Kalman filter/smoothing approach. Also presented are recommendations for future research topics stemming from this research.

5.2 Conclusions

5.2.1 Digital Filtering and Numerical Methods. In this research, two methods of performing numerical differentiation are developed. The first method is based upon a Taylor's series approximation to the derivative. In the absence of noise, the higher order differentiation algorithms provide better performance. When noise is added to the position data, however, there is no benefit to using higher order numerical differentiation algorithms.

The second method uses cubic splines to describe a curve that fits the position data. The expression for the curve is differentiated analytically and evaluated at the points of interest. In the absence of noise, this method performs slightly better than a second order numerical differentiator. In the presence of noise, the performance of the cubic spline is comparable to the Taylor's series-based numerical differentiators.

These numerical differentiation algorithms were tested with data at 1 Hz and 10 Hz rates. Both the Taylor's series and cubic spline differentiation algorithms are more accurate at the higher rate of 10 Hz.

The data processed by the numerical differentiation algorithm is low pass filtered before and after the operation. When performing a numerical differentiation, it is beneficial to remove as much noise as possible from the signal before differentiating. The prefilter, however, was not found to be particularly effective. Since the differentiation procedure loses accuracy in the presence of noise, improving the prefilter performance is essential to improving the effectiveness of this approach.

Both the prefilter and postfilter were designed as IIR filters. FIR filter designs were not able to meet the performance requirements, especially in the area of allowable passband loss. The IIR filters were run forward and backwards through the data, allowing the filter to achieve a linear phase response, crucial to the accurate reconstruction of the position data. Given that the FIR filters were unable to meet performance standards and that the IIR filters were non-causal, it is unlikely that this digital filtering and numerical methods approach would be able to support real time operation¹.

The biggest disadvantage to this method is that it's development used and required knowledge of the truth data. The low pass filters were designed to eliminate as much noise as possible without corrupting the data, and this was accomplished with knowledge of the truth data. Similarly, the smoothing parameter used in the cubic smoothing spline algorithm was chosen such that it minimized the difference between the estimated velocity and true velocity. In a real world application, it would not be possible to "tune" these parameters so exactly. Certainly simulation would be an aid to determining these parameters, however it remains to be seen whether the same performance levels can be reached.

In spite of these disadvantages, this method was able to meet the required specification of 0.005 m/s 3-D RMS 1σ in simulation. While this research may have created more questions than it answered, these results are encouraging, and show that the SARS concept may be feasible navigation reference system.

5.2.2 Kalman Filtering/Smoothing. In contrast with the digital filtering with numeric differentiation method, the Kalman filter/smoother did not demonstrate better performance at the higher data rate of 10 Hz. The overall performance of the Kalman filter/smoother fell below the desired accuracy of 0.005m/s 3-D RMS 1σ for a segment of the trajectory containing benign dynamics. The Kalman filter/smoother performance was hindered greatly by the inadequacy of the model assumptions. During the portions of the flight profile that matched the model assumptions, the Kalman filter/smoother performed well.

¹Real time support is not required for the SARS concept. In this post processing environment it is prudent to take advantage of non-causal filters.

One way to improve the performance of Kalman filter would be to lower the measurement noise. Since the position accuracy of 0.1 m is given in the problem statement, it may not be directly possible to lower the measurement noise. However, one could alter the Kalman filter models to accept ranging measurements. In this manner, ranging error terms such as tropospheric delay and multipath could be estimated and potentially reduced. Since the ranging equations are non-linear, an extended Kalman filter formulation or other compensation may be required.

To exploit the availability of past and future measurements in the Kalman filter, a fixed interval Kalman smoother was implemented. While there was a benefit to the smoothing operation, it was not enough to completely overcome the inherent model inadequacy. The Fraser smoothability criteria indicates that the kinematic models used in this research are not very smoothable when the dynamics driving noise is low (i.e. the internal dynamics model matches the observations) and this is reflected in the results. When Q is increased to compensate for an inadequate model, the benefit of smoothing is greater.

While the performance objectives were not met using the Kalman filter/smoothener approach for the entire benign trajectory, there are advantages to this method. Foremost is that this method is less reliant upon knowledge of the truth data in order to "tune" the system, as long as one has confidence in the dynamics model. Since the Kalman filter/smoothener showed promise when the model was well matched to the measurement data, it still may be a useful research avenue for SARS.

5.3 Recommendations

The following are just a few of the many possible research topics for future consideration. The recommendations presented represent research areas most important to proving the feasibility of the SARS concept.

5.3.1 Receiver Geometry. As was exhibited in this research, proper receiver location is essential to maintaining good geometry (e.g. DOP) over the course of a flight. Since the accuracy of the solution to the GPS ranging equations worsens as the receiver locations become more coplanar, it is likely that there exists a limit on what the acceptable

DOP is to maintain a position accuracy of 0.1 m. If this DOP limit can be found, it may be possible to determine an "optimal" placement of pseudolite receivers that maintains good geometry throughout a flight profile.

5.3.2 Flight Profiles. Flight profiles used to test navigation systems are typically 2-3 hour missions involving a combination of benign and high dynamic segments [39]. This research also showed that such flight profiles will have to be modified to maintain good receiver geometry. It may be necessary to consider the problem of determining appropriate flight profiles and optimizing receiver placement simultaneously.

5.3.3 Error Modeling. For the unique inverted pseudolite concept of SARS, creating SARS-specific tropospheric and multipath models could increase positioning accuracy, and subsequently increase velocity accuracy. Using empirical data it may be possible to quantify and model the tropospheric delay and multipath error terms, given the relatively consistent climate of the New Mexico desert, as well as *apriori* knowing the receiver locations.

5.3.4 Adaptive Kalman Filtering. This research shows the potential for a kinematic Kalman filter based solution if the underlying filter model adequately describes the dynamics of the trajectory. While one Kalman filter may not be able to meet the accuracy needed by SARS, it may be worthwhile to consider an adaptive filtering technique. For example, a Multiple Model Adaptive Estimation (MMAE) [25] technique could be used to set up a bank of Kalman filters which run in parallel. Using residual monitoring techniques the outputs of these Kalman filters can be multiplexed and/or blended in an attempt to achieve better performance than that of a single Kalman filter.

Appendix A. Calculation of RMS Error

The objective of this appendix is to illustrate the error metrics used in this thesis research. A scalar metric, the Root Mean Square (RMS), is used to describe the error of a vector of computed values from the true values. Typically these vectors are a time history of position or velocity.

Consider a time history of three dimensional position expressed as three vectors, X , Y and Z , as well as the estimates of position \hat{X} , \hat{Y} and \hat{Z} , all of length k . The 3-D RMS error metric is given by:

$$\text{RMS} = \frac{1}{k} \cdot \sum_{i=1}^k \sqrt{(X(t_i) - \hat{X}(t_i))^2 + (Y(t_i) - \hat{Y}(t_i))^2 + (Z(t_i) - \hat{Z}(t_i))^2} \quad (\text{A.1})$$

In the case of data from more than one simulation (Monte Carlo analysis), it is also useful to compute the following mean and standard deviation statistics:

$$\text{mRMS} = \frac{1}{n} \cdot \sum_{i=1}^n \text{RMS}(i) \quad (\text{A.2})$$

$$1\sigma_{\text{mRMS}} = \sqrt{\frac{1}{n-1} \cdot \sum_{i=1}^n (\text{RMS}(i) - \text{mRMS})^2} \quad (\text{A.3})$$

where mRMS denotes the mean RMS error, $1\sigma_{\text{mRMS}}$ denotes the standard deviation in RMS error and n represents the number of simulation runs performed.

Appendix B. Constant Velocity Kalman Filter Results

This appendix contains the tuning plots for the Constant Velocity Kalman filter. A legend for the plots is presented below:

Table B.1 Legend for Filter Tuning Plots

Symbol	Definition
— Solid Line	Mean Error
... Dotted Line	Mean Error \pm True Sigma
- - Dashed Line	\pm Filter Predicted Sigma

Kalman Filter

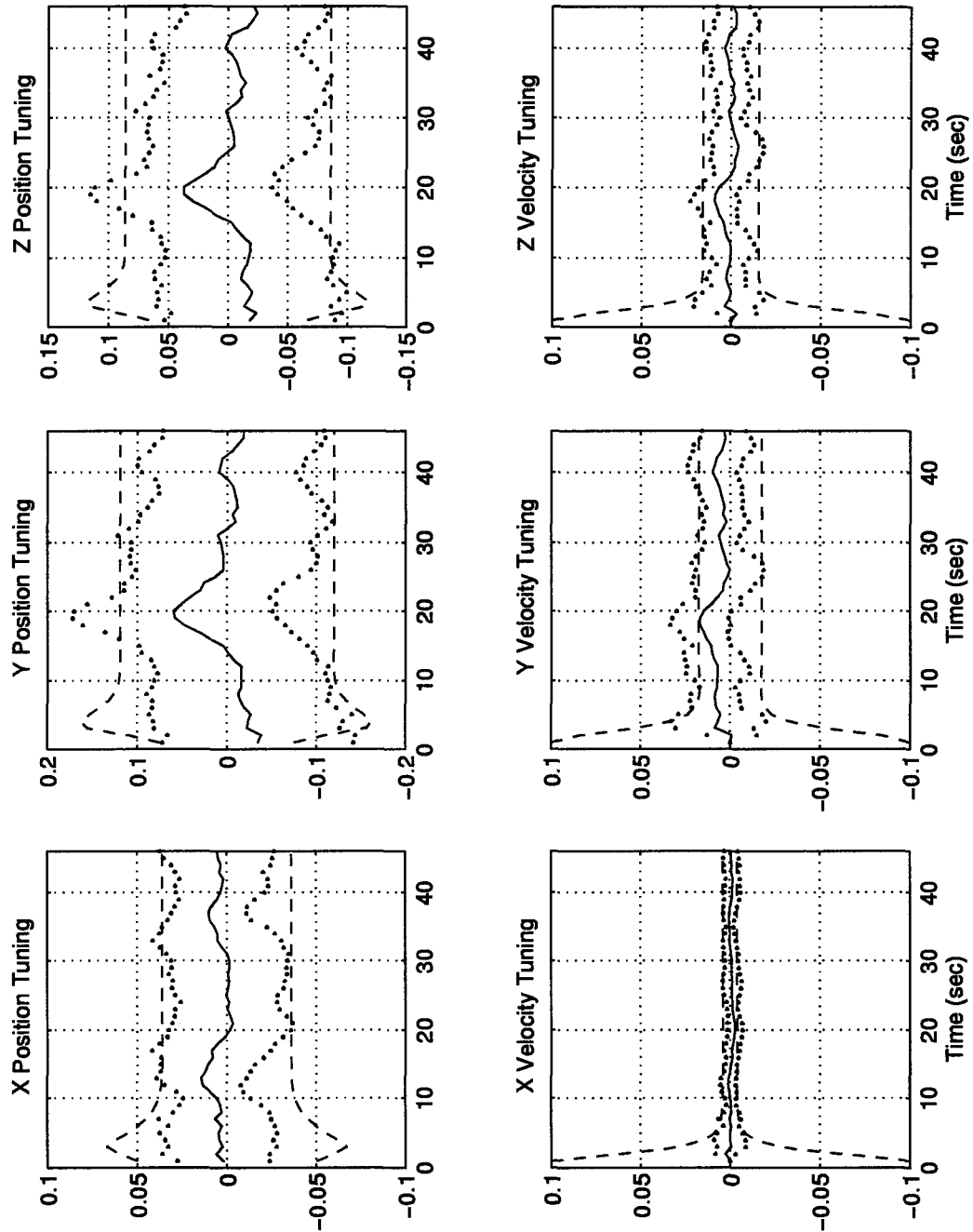


Figure B.1 Colored Noise at 1 Hz, Proper Model

Kalman Filter

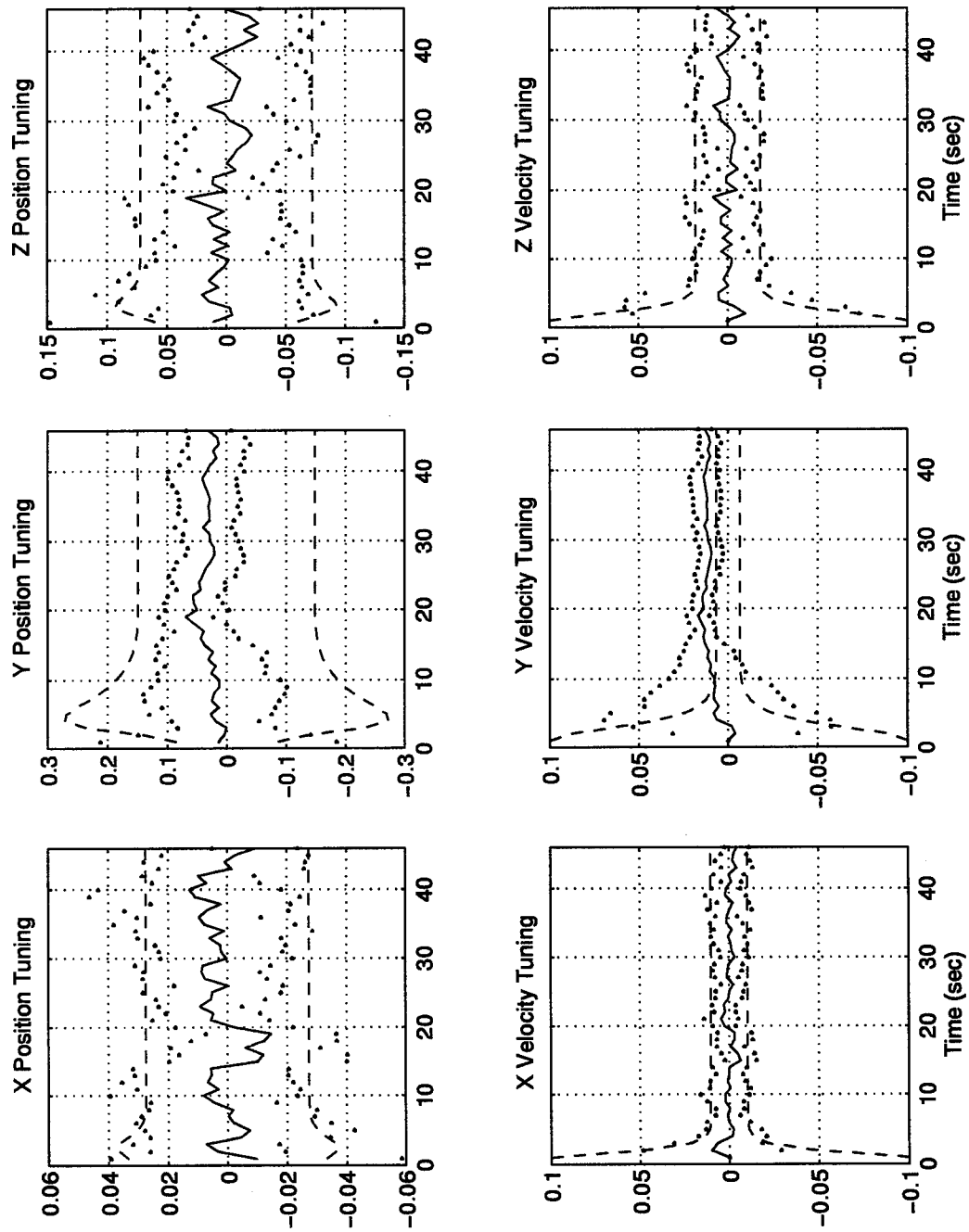


Figure B.2 White Noise at 1 Hz, Proper Model

Kalman Filter

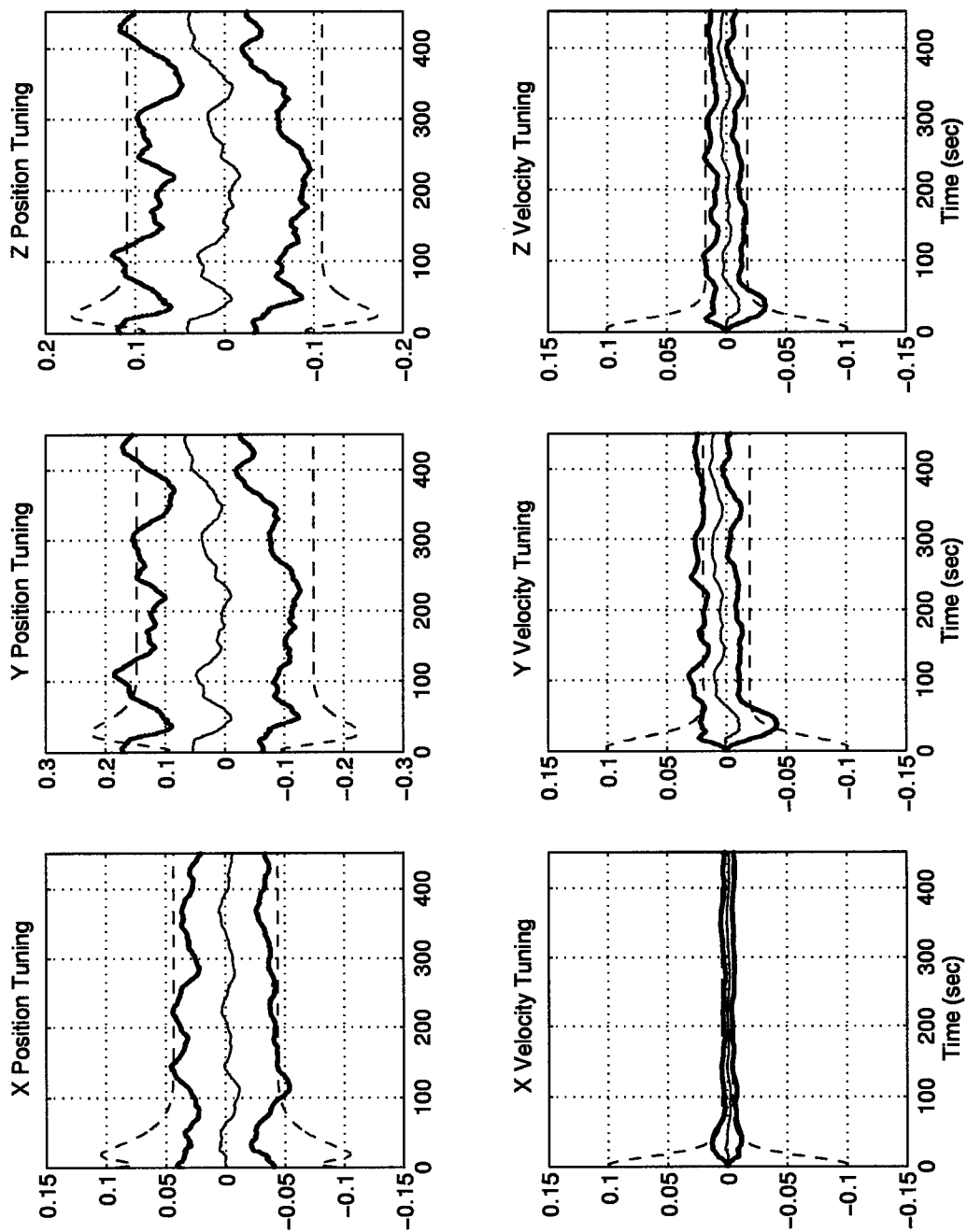


Figure B.3 Colored Noise at 10 Hz, Proper Model

Kalman Filter

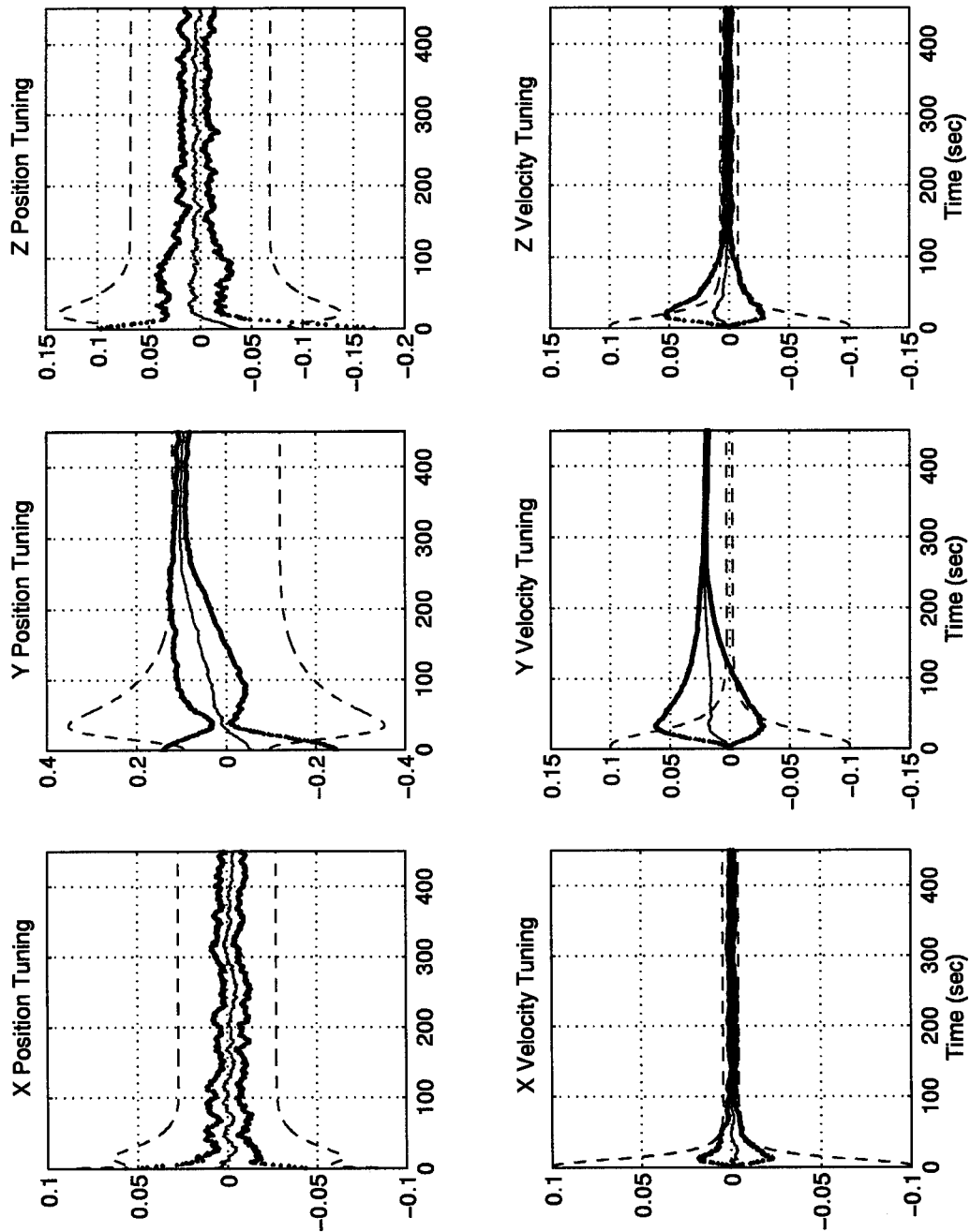


Figure B.4 White Noise at 10 Hz, Proper Model

Kalman Filter

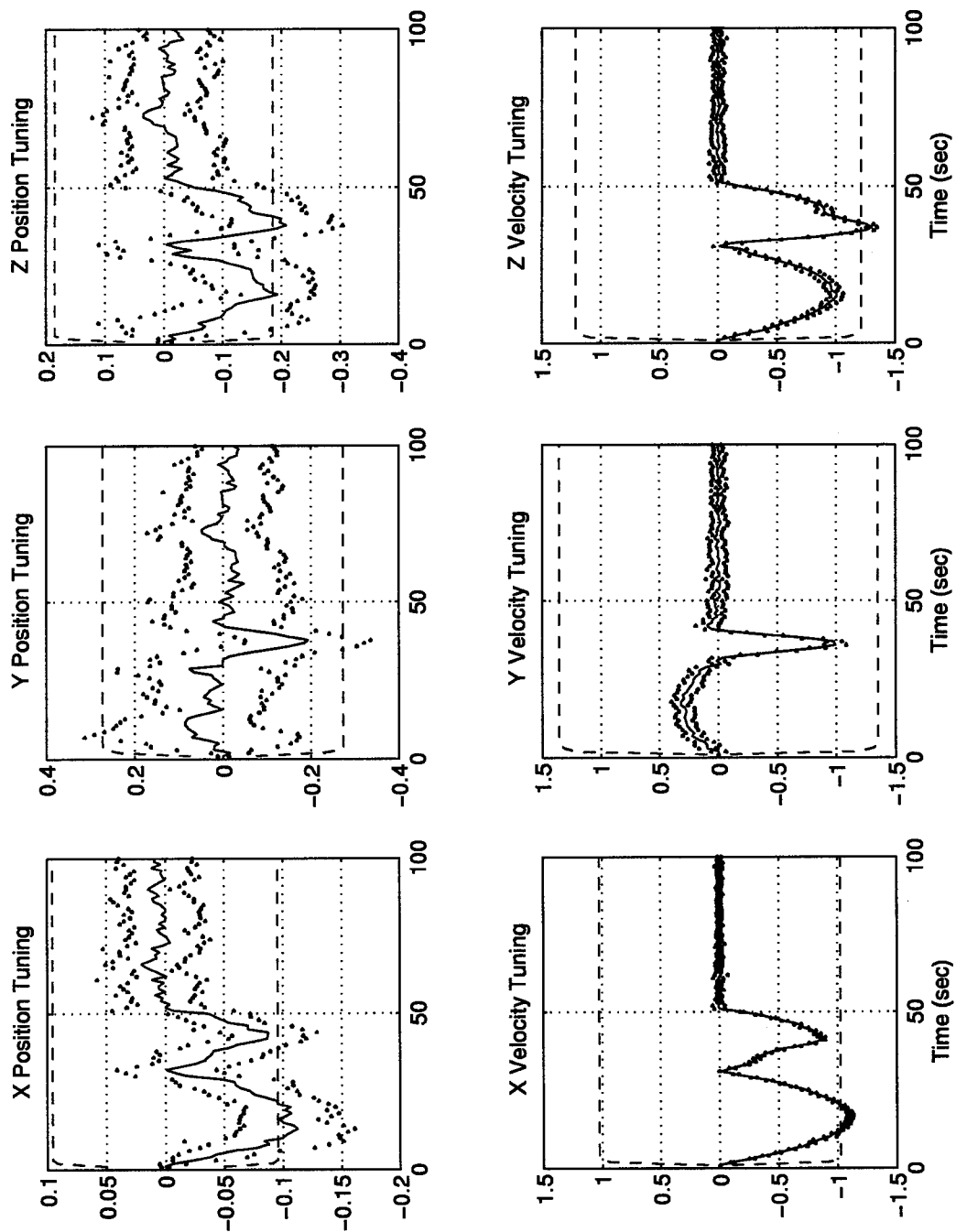


Figure B.5 Colored Noise at 1 Hz, Improper Model

Kalman Filter

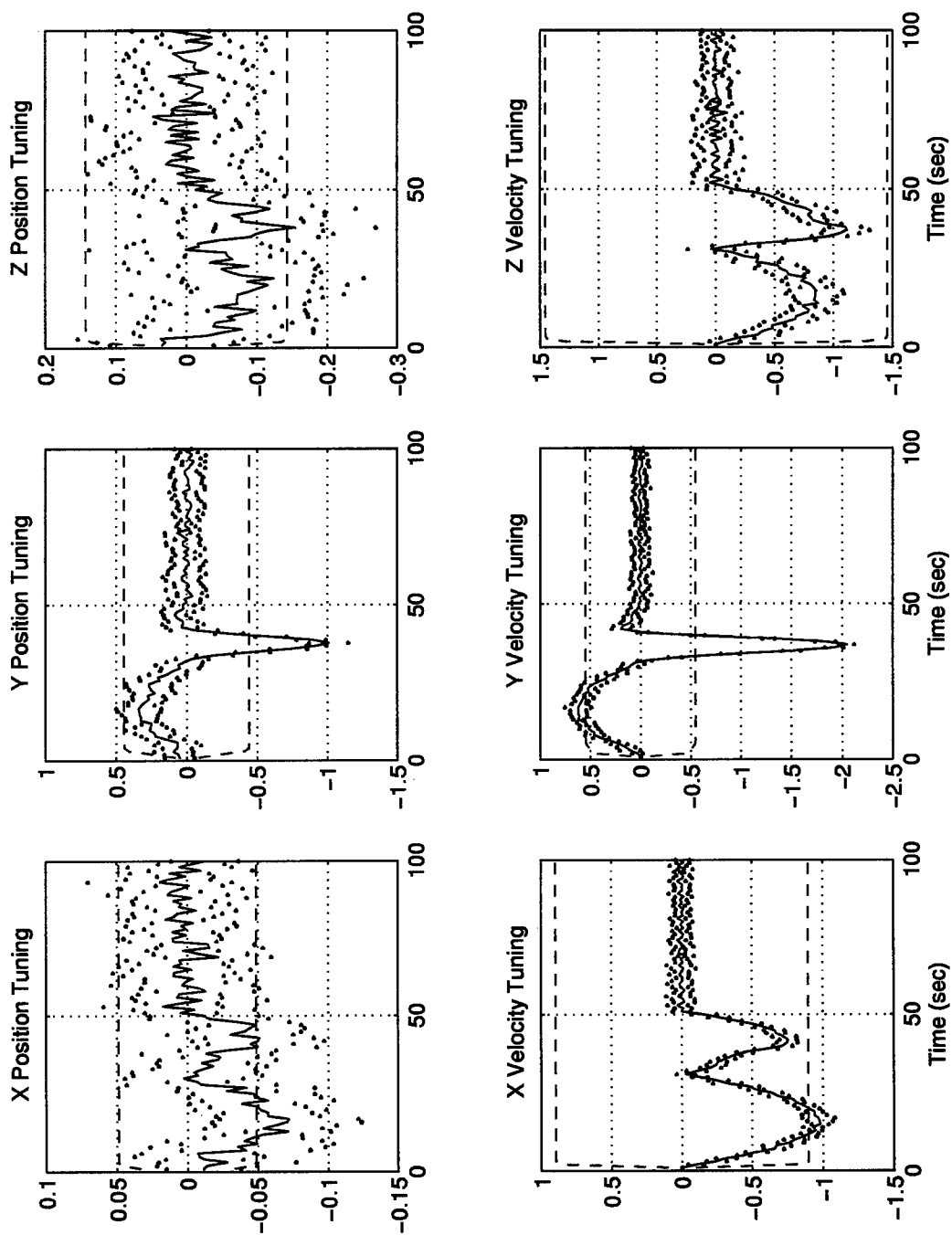


Figure B.6 White Noise at 1 Hz, Improper Model

Kalman Filter

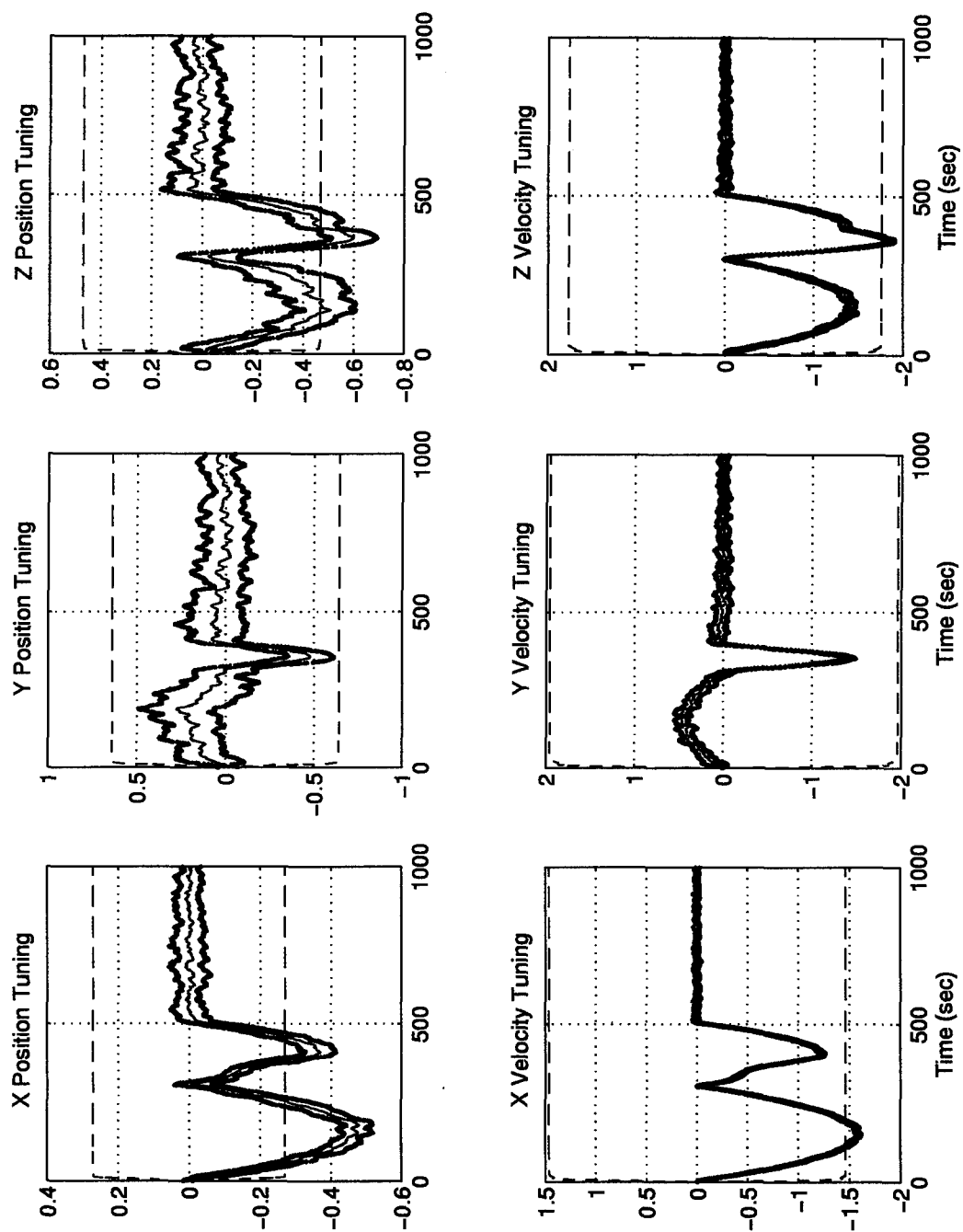


Figure B.7 Colored Noise at 10 Hz, Improper Model

Kalman Filter

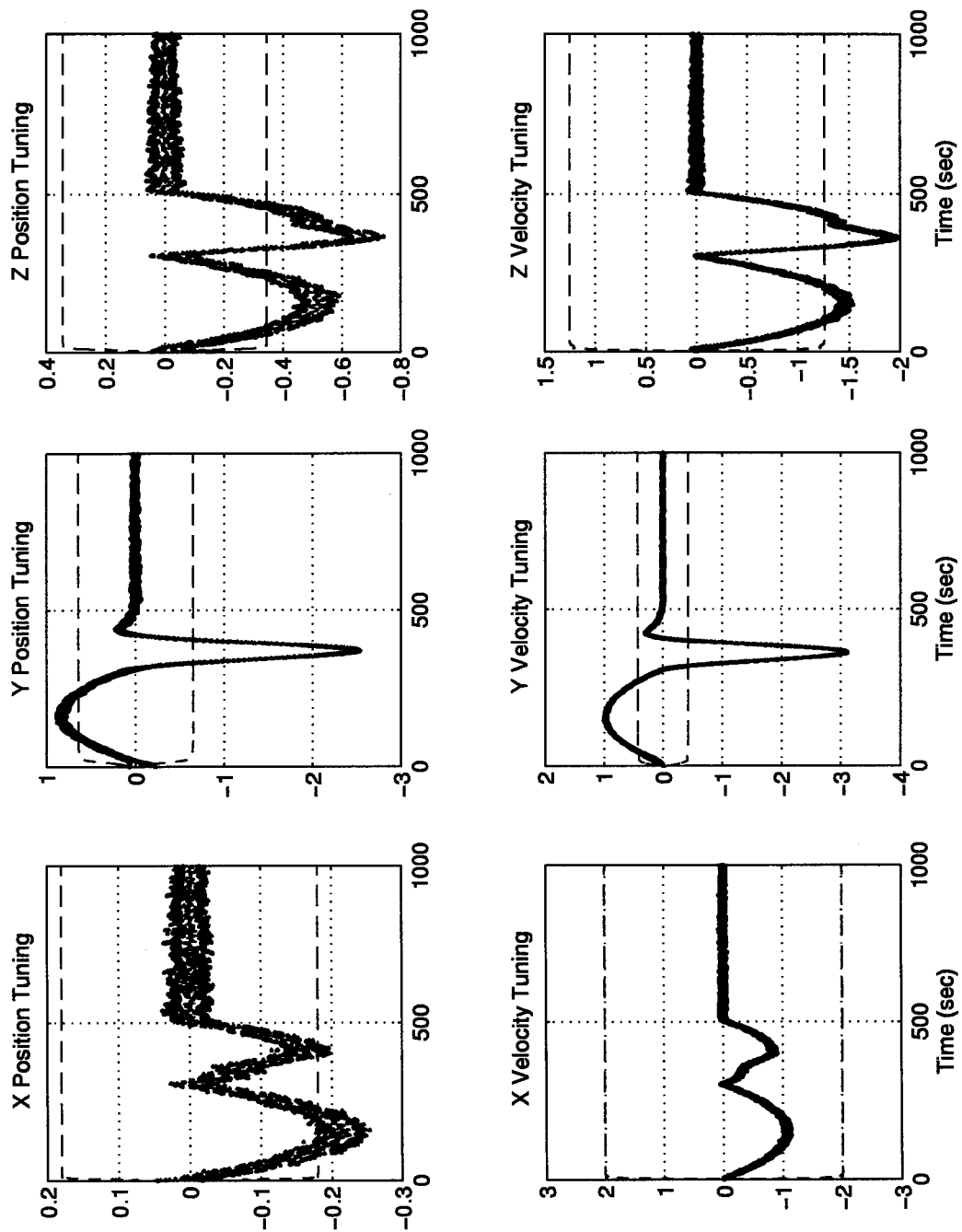


Figure B.8 White Noise at 10 Hz, Improper Model

Appendix C. Constant Acceleration Kalman Filter Results

This appendix contains the tuning plots for the Constant Velocity Kalman filter. A legend for the plots is presented below:

Table C.1 Legend for Filter Tuning Plots

Symbol	Definition
— Solid Line	Mean Error
... Dotted Line	Mean Error \pm True Sigma
-- Dashed Line	\pm Filter Predicted Sigma

Kalman Filter

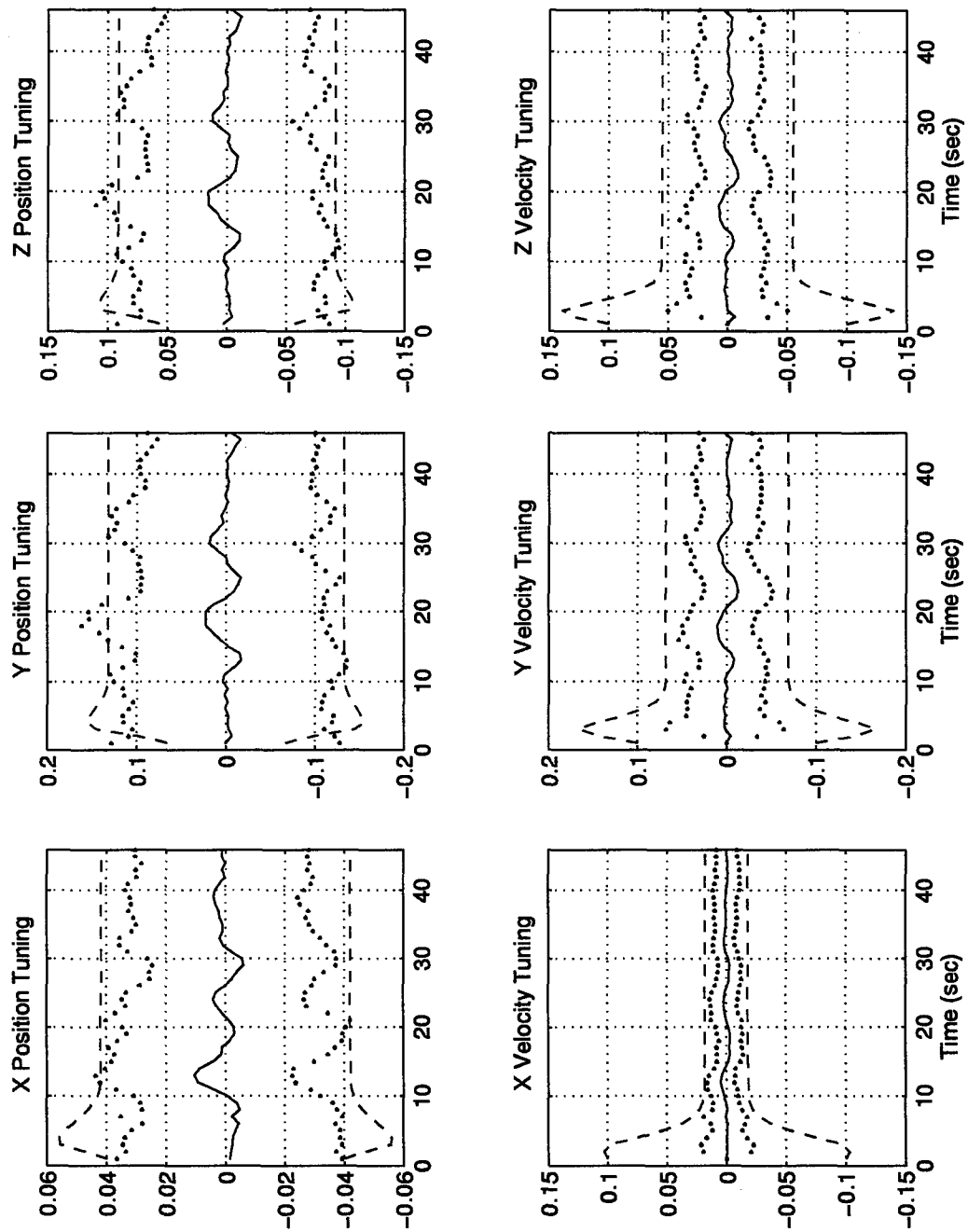


Figure C.1 Colored Noise at 1 Hz, Proper Model

Kalman Filter

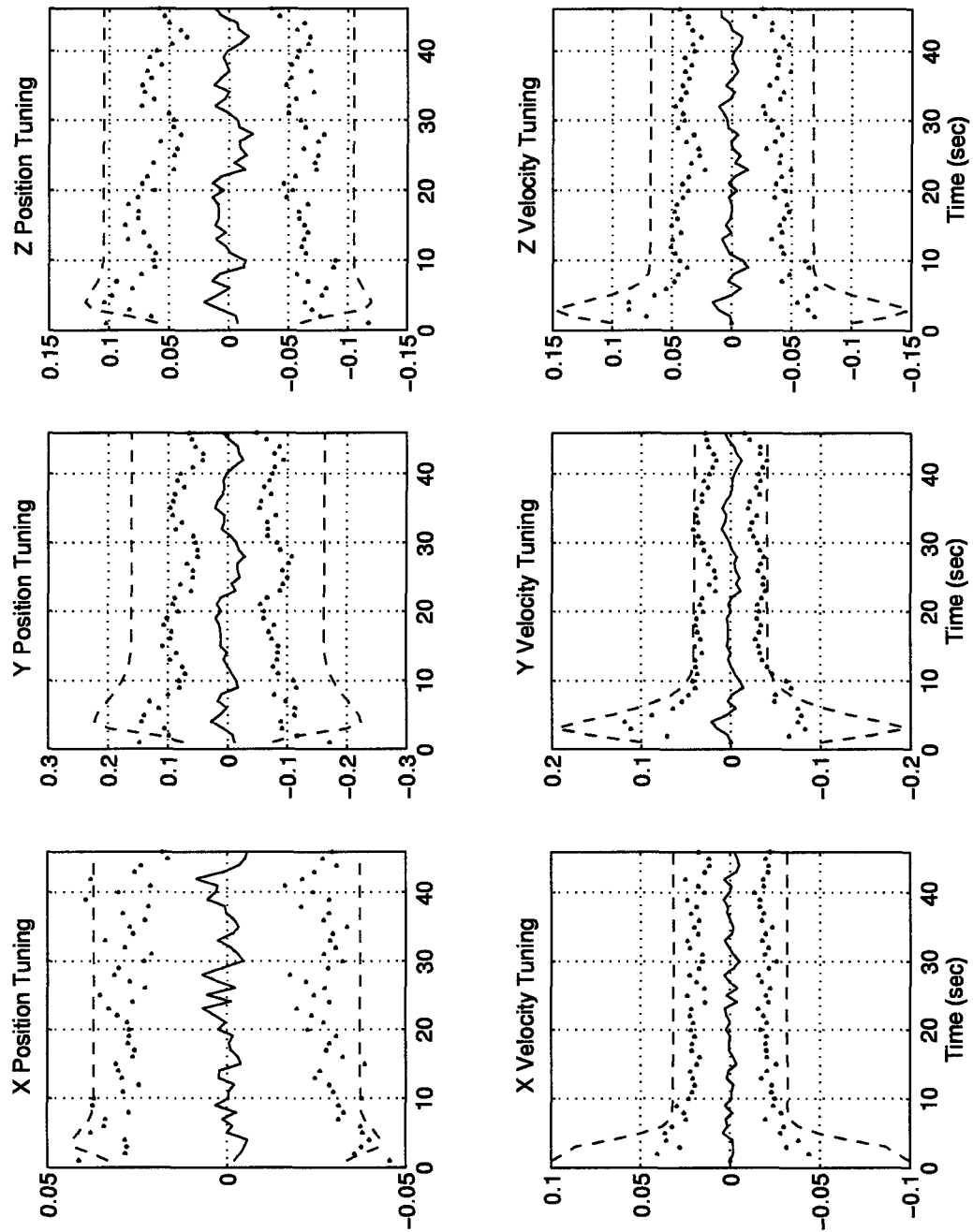


Figure C.2 White Noise at 1 Hz, Proper Model

Kalman Filter

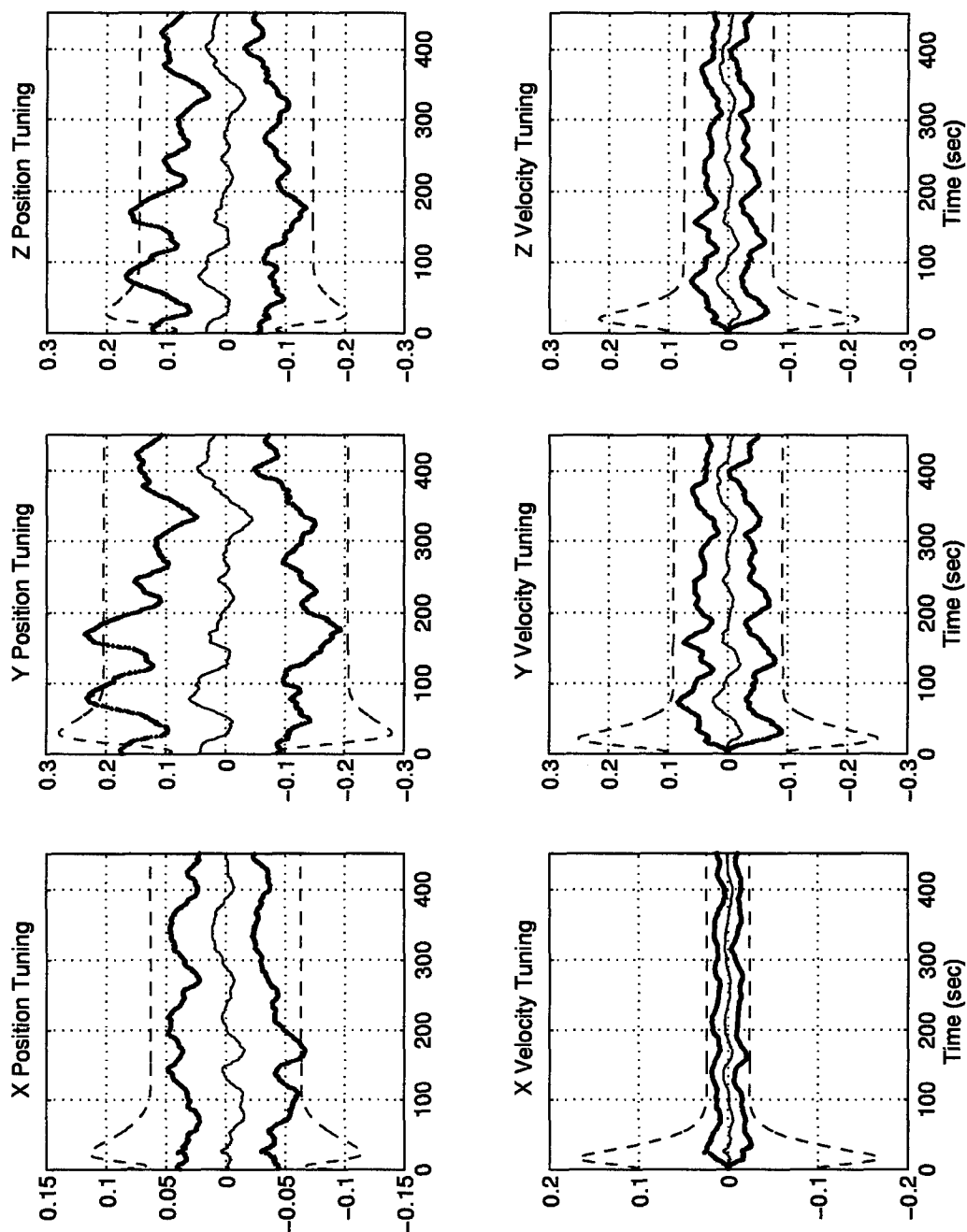


Figure C.3 Colored Noise at 10 Hz, Proper Model

Kalman Filter

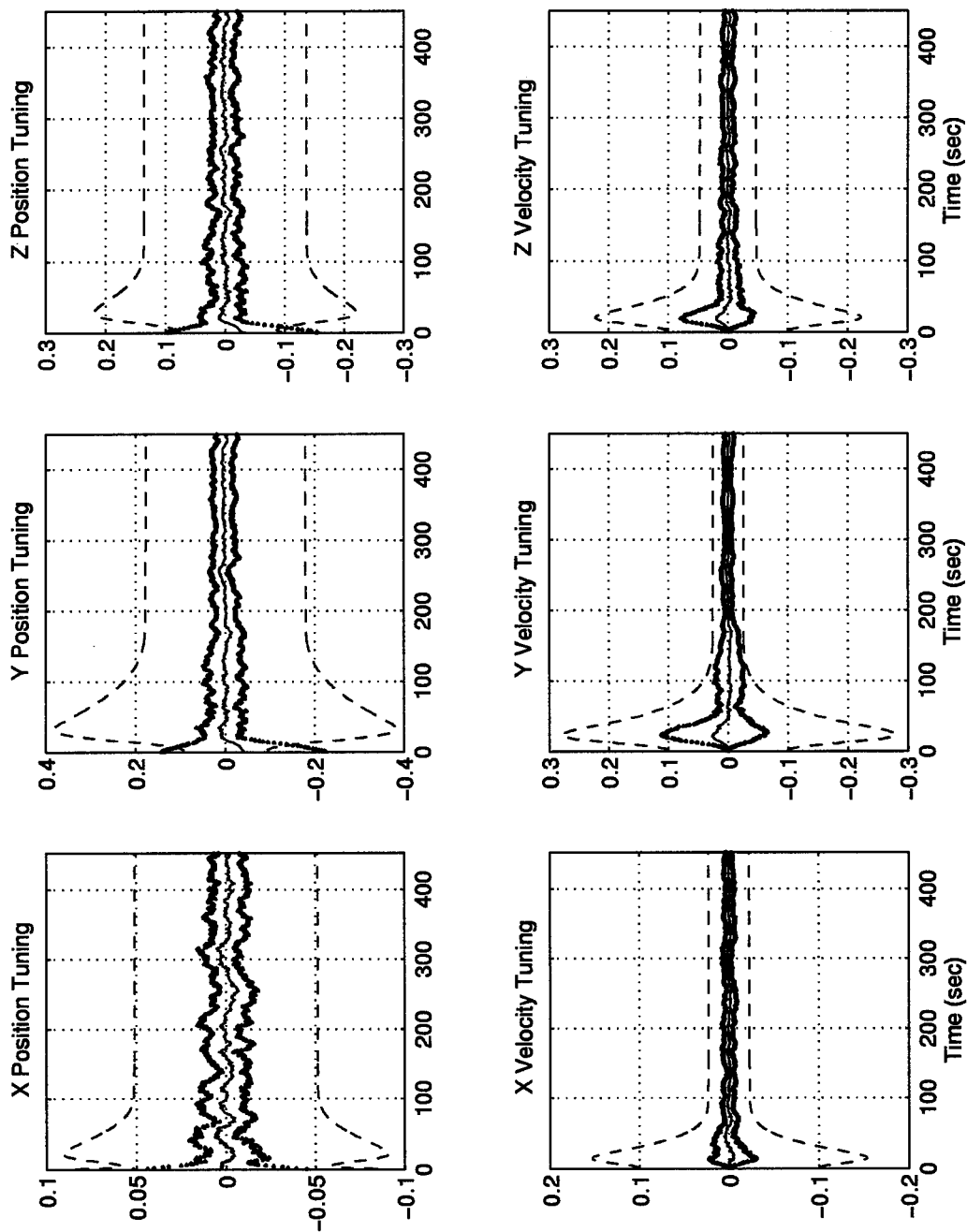


Figure C.4 White Noise at 10 Hz, Proper Model

Kalman Filter

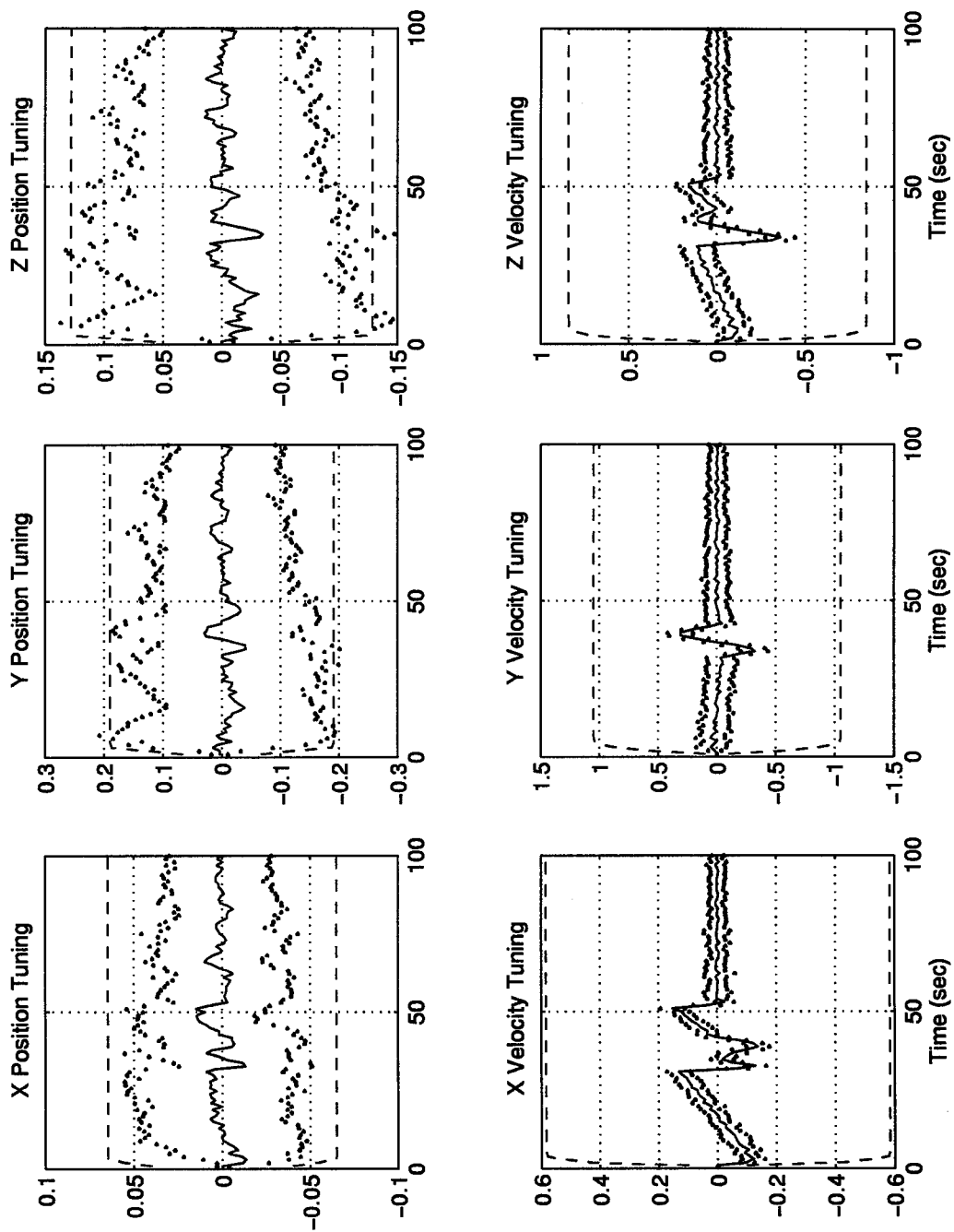


Figure C.5 Colored Noise at 1 Hz, Improper Model

Kalman Filter

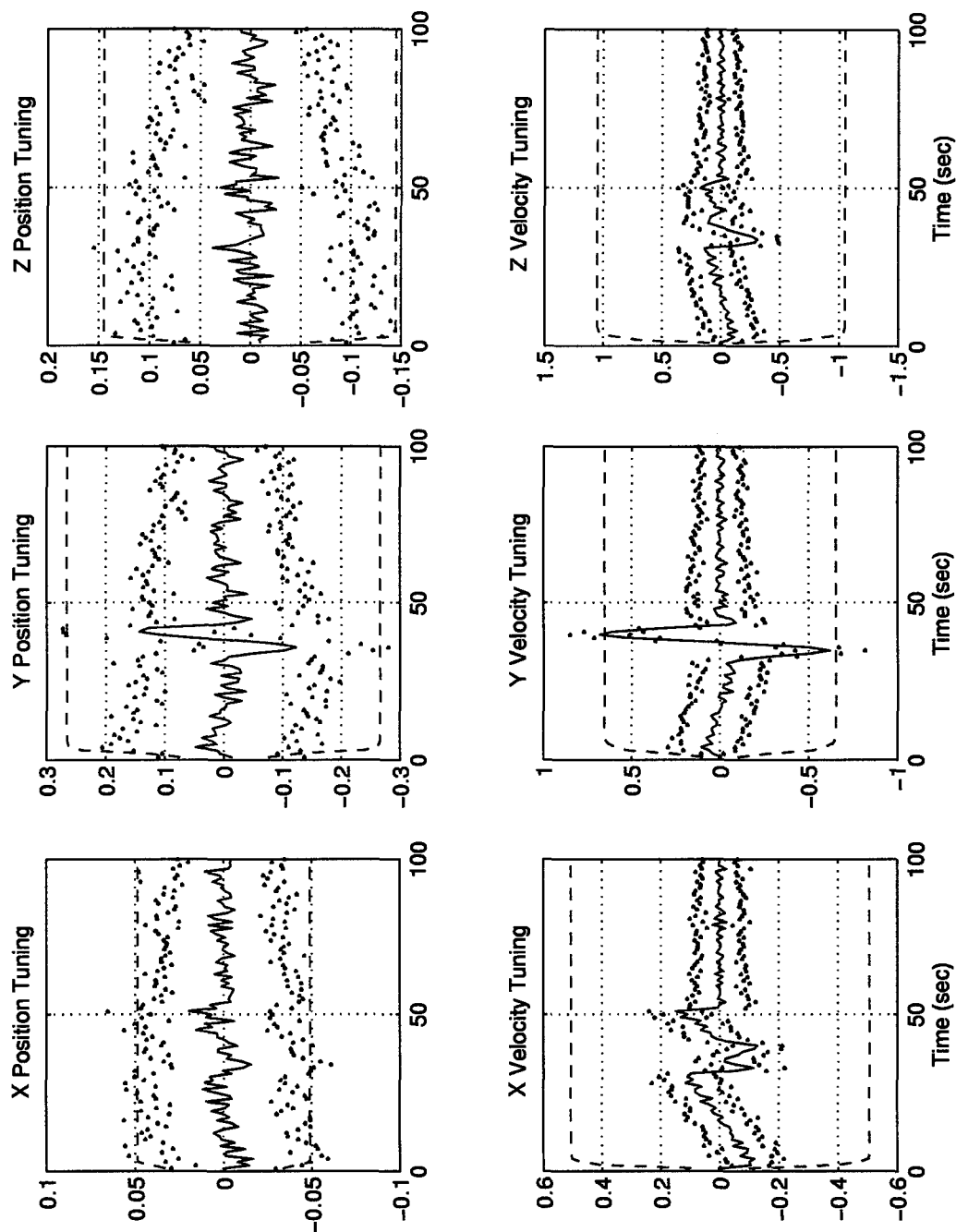


Figure C.6 White Noise at 1 Hz, Improper Model

Kalman Filter

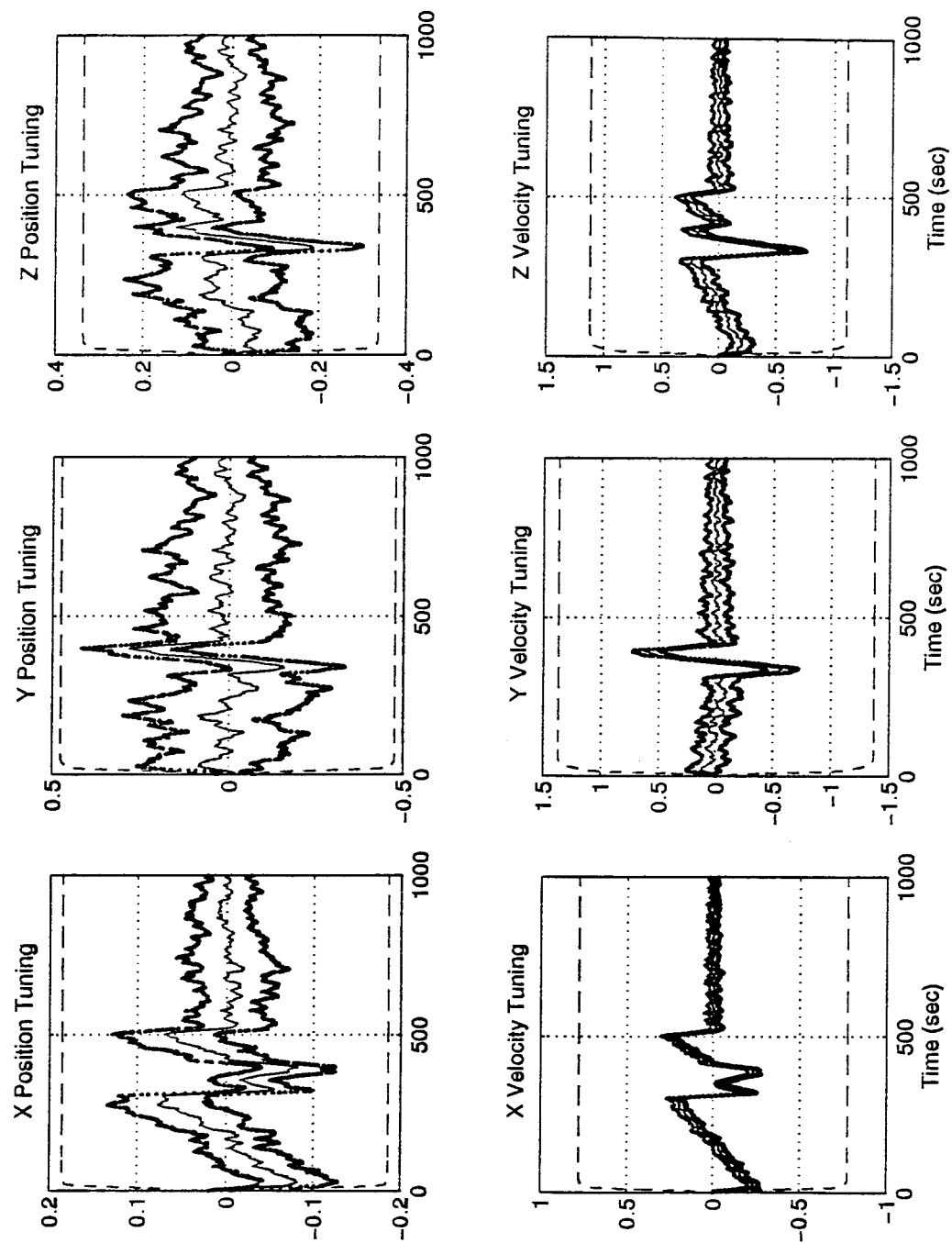


Figure C.7 Colored Noise at 10 Hz, Improper Model

Kalman Filter

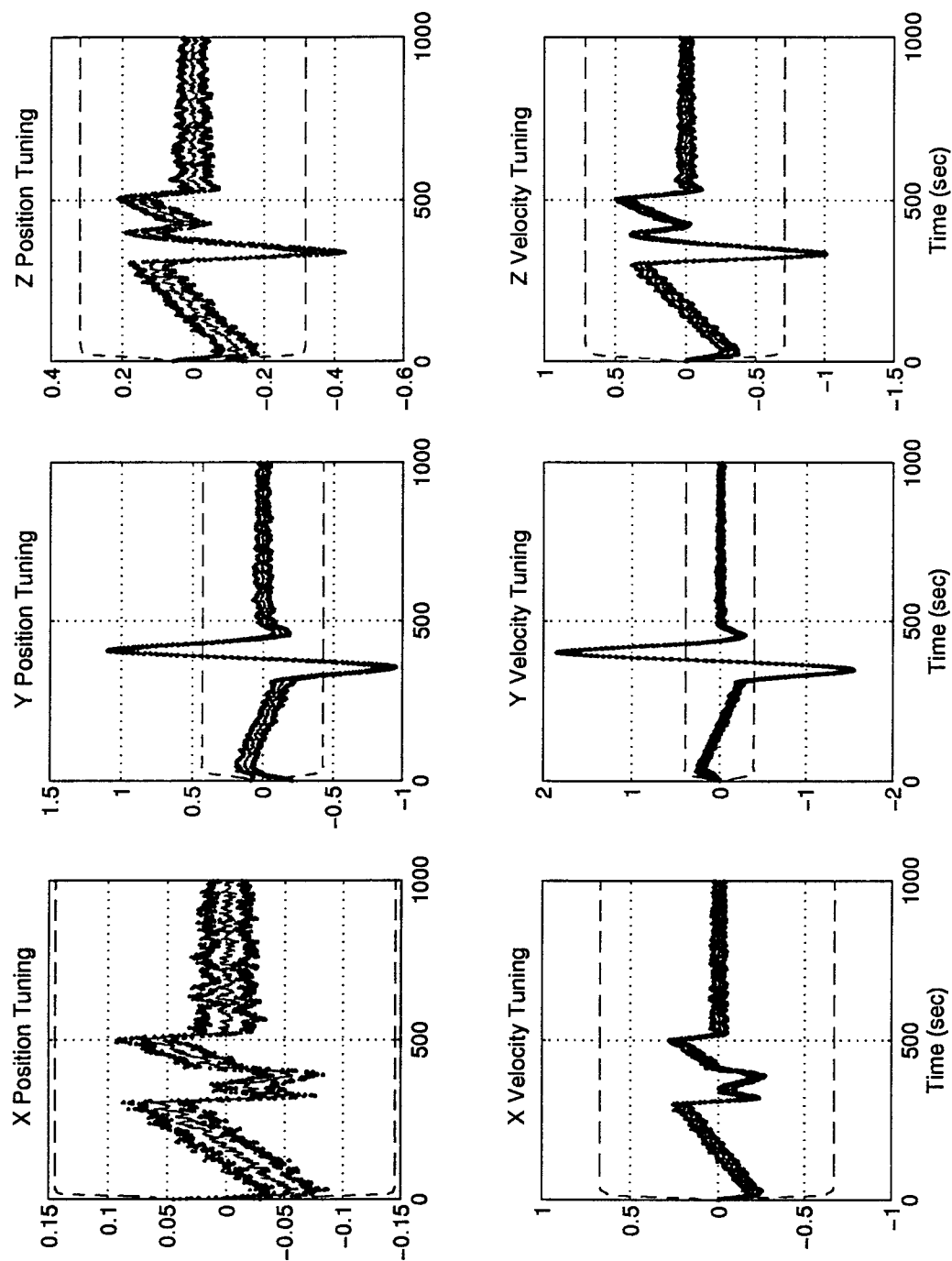


Figure C.8 White Noise at 10 Hz, Improper Model

Appendix D. Constant Acceleration, 1st Order Markov Kalman Filter Results

This appendix contains the tuning plots for the Constant Velocity Kalman filter. A legend for the plots is presented below:

Table D.1 Legend for Filter Tuning Plots

Symbol	Definition
— Solid Line	Mean Error
... Dotted Line	Mean Error \pm True Sigma
- - Dashed Line	\pm Filter Predicted Sigma

Kalman Filter

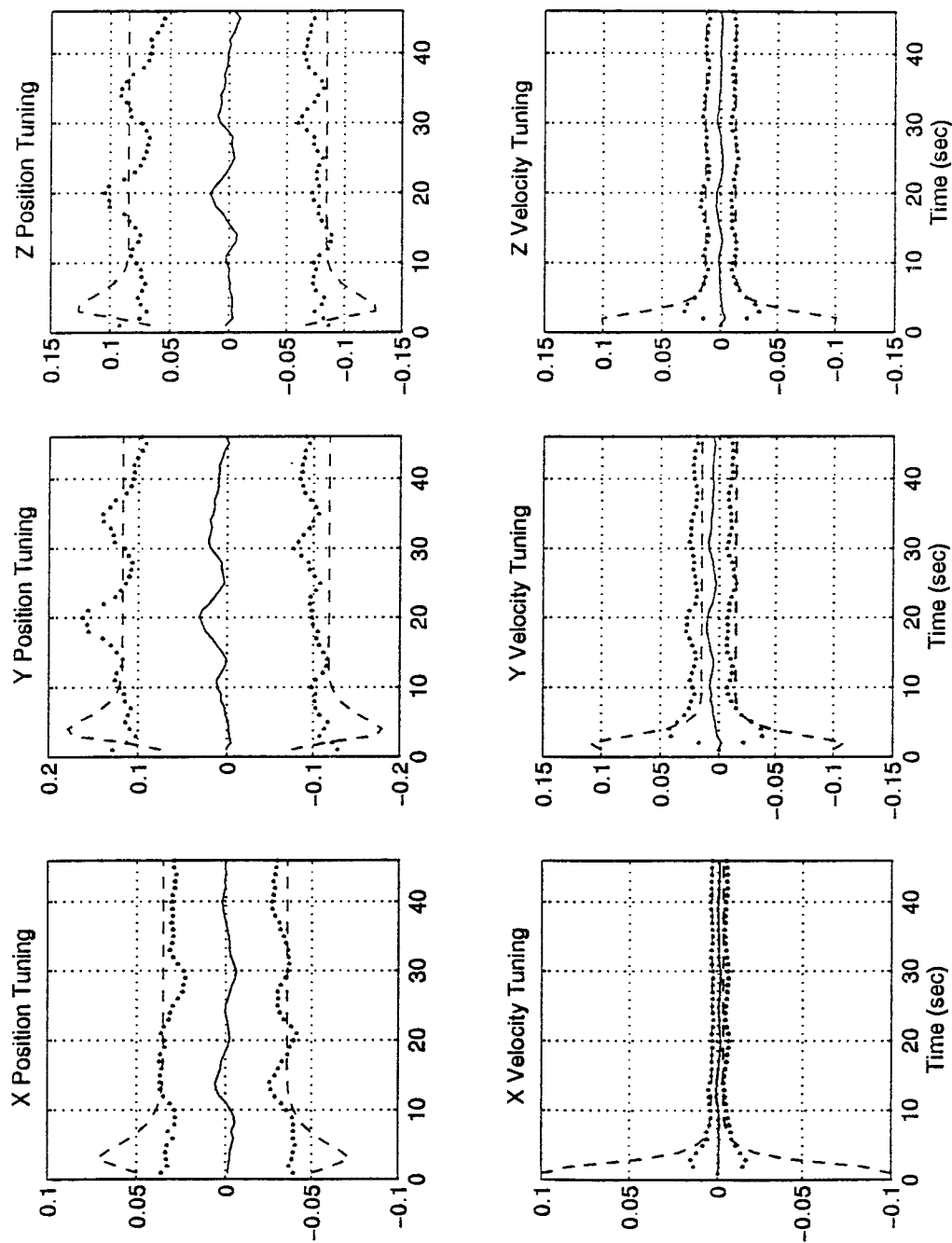


Figure D.1 Colored Noise at 1 Hz, Proper Model

Kalman Filter

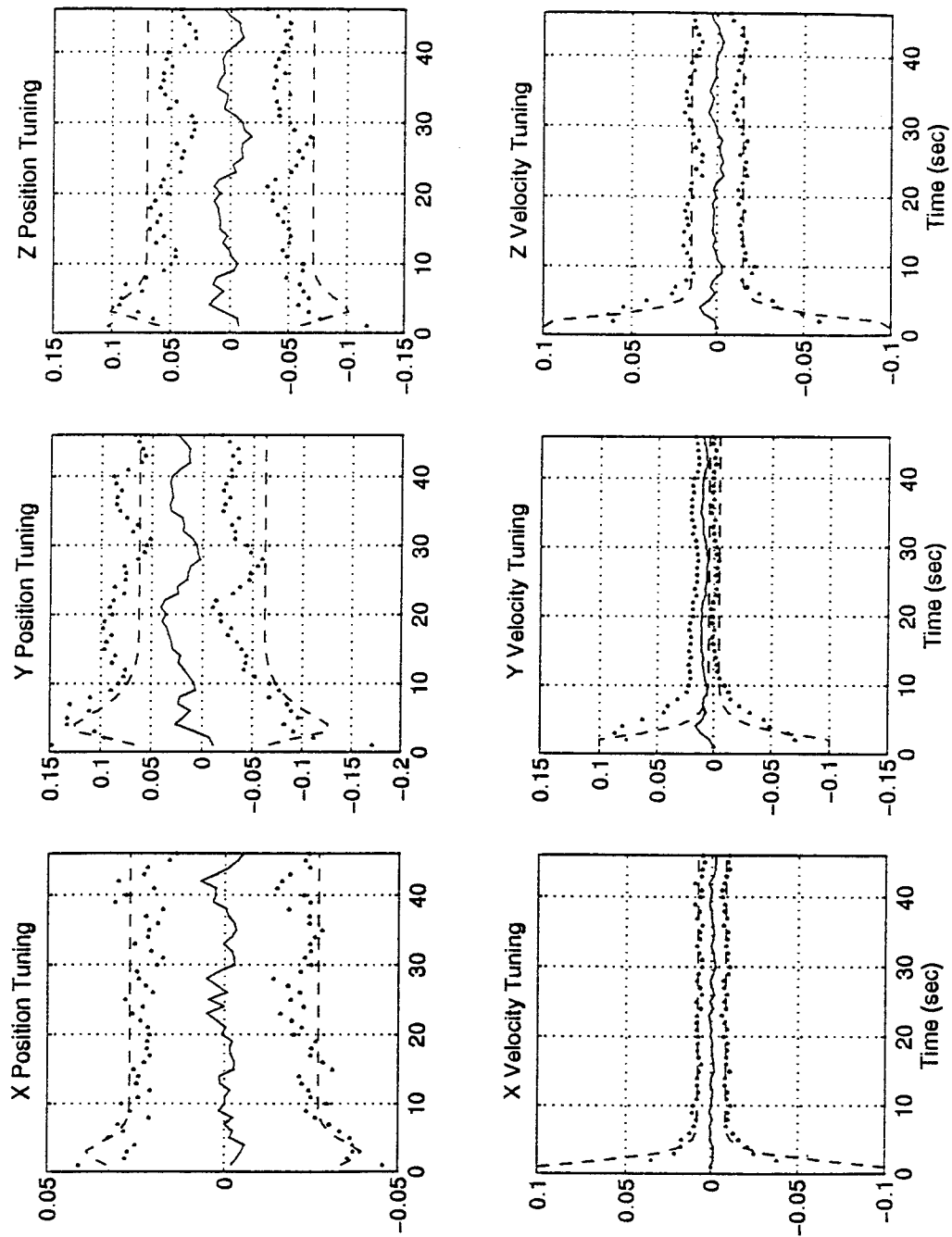


Figure D.2 White Noise at 1 Hz, Proper Model

Kalman Filter

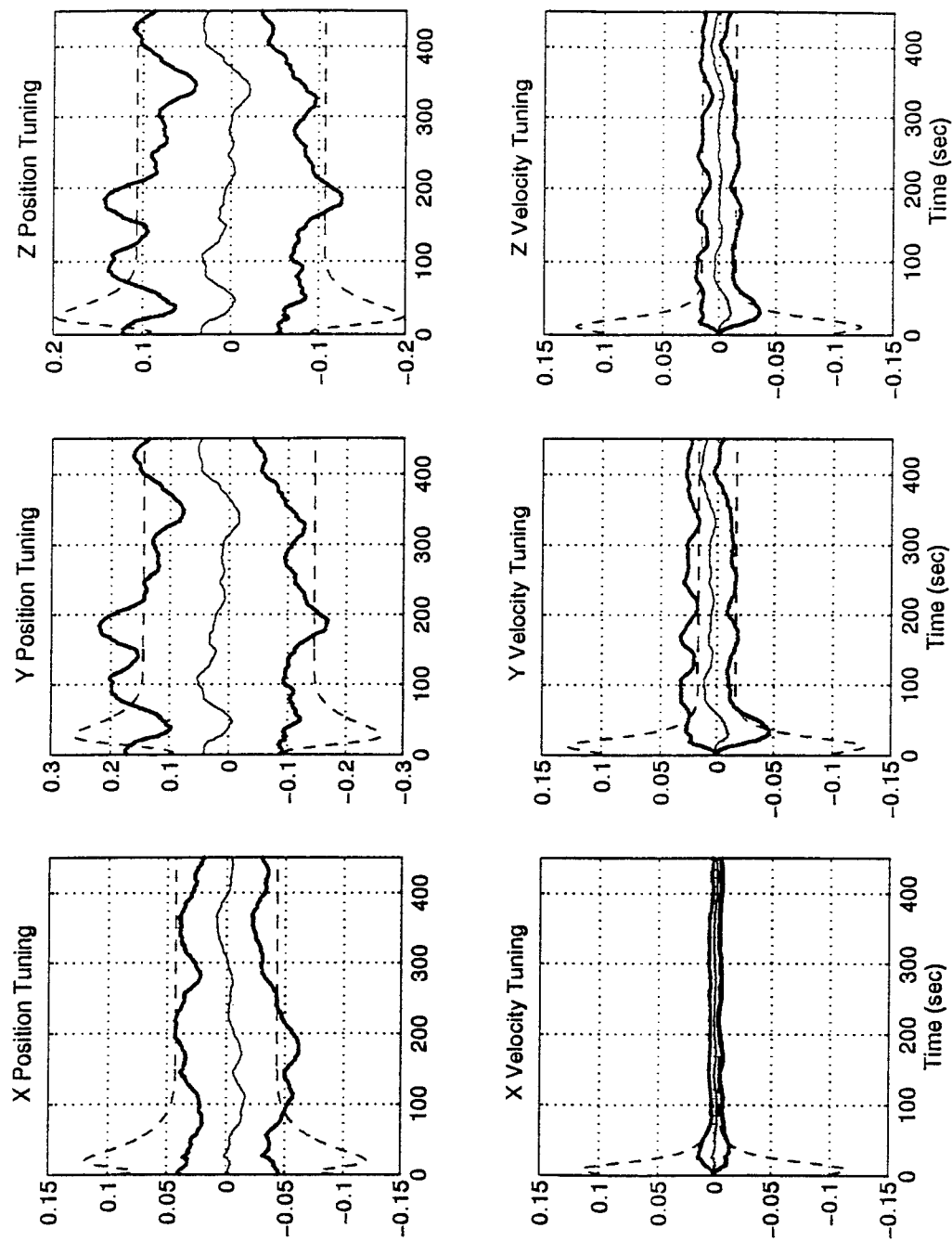


Figure D.3 Colored Noise at 10 Hz, Proper Model

Kalman Filter

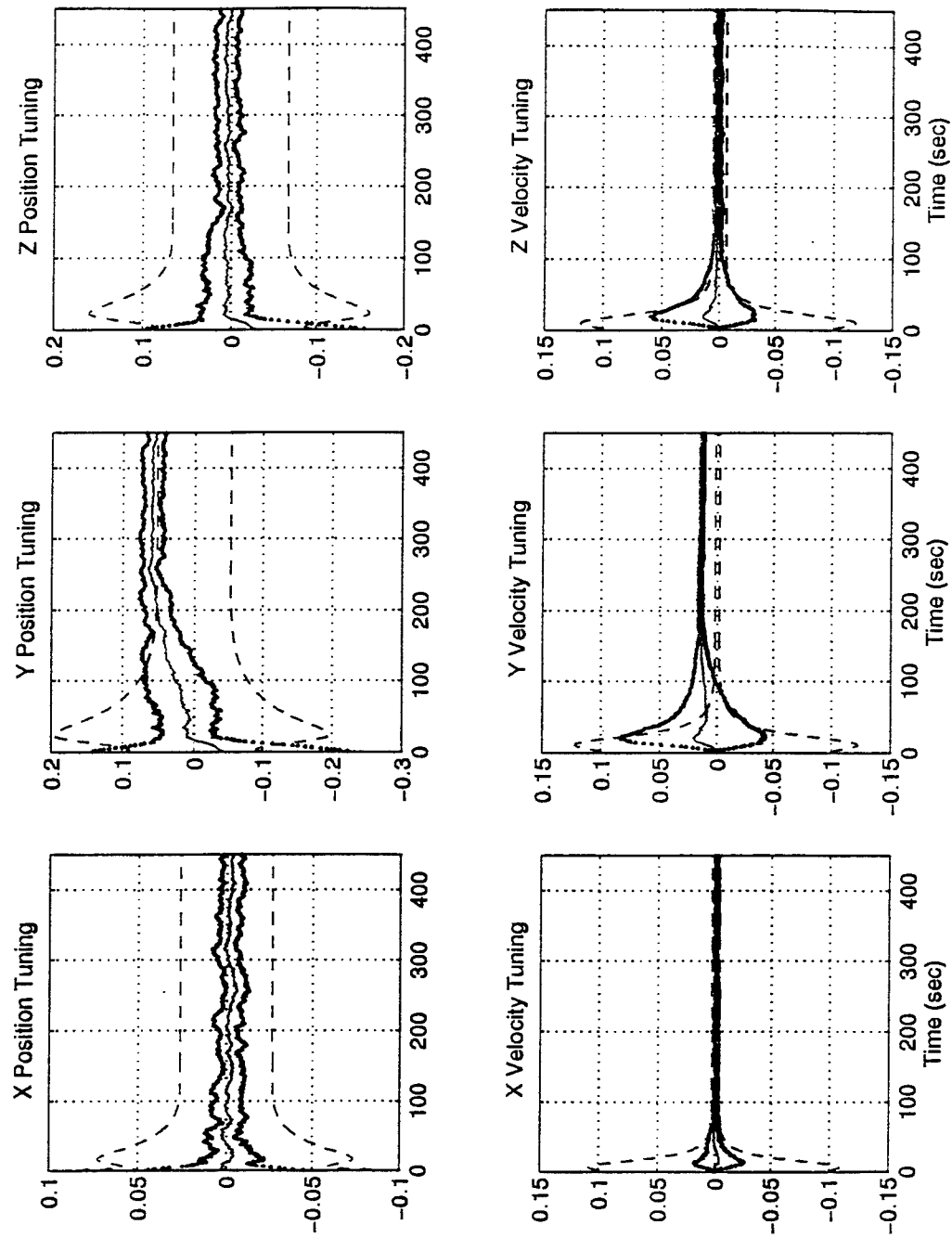


Figure D.4 White Noise at 10 Hz, Proper Model

Kalman Filter

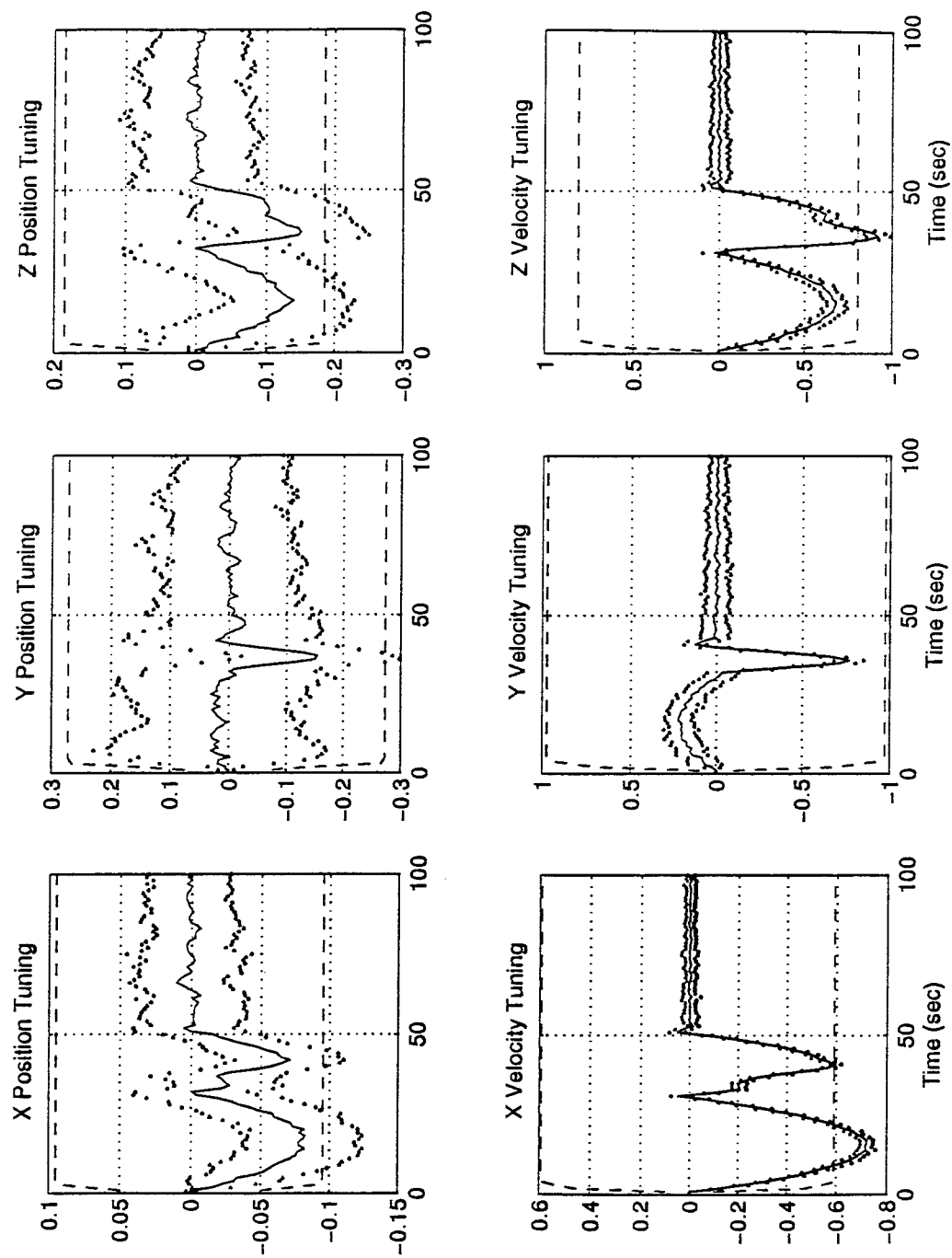


Figure D.5 Colored Noise at 1 Hz, Improper Model

Kalman Filter

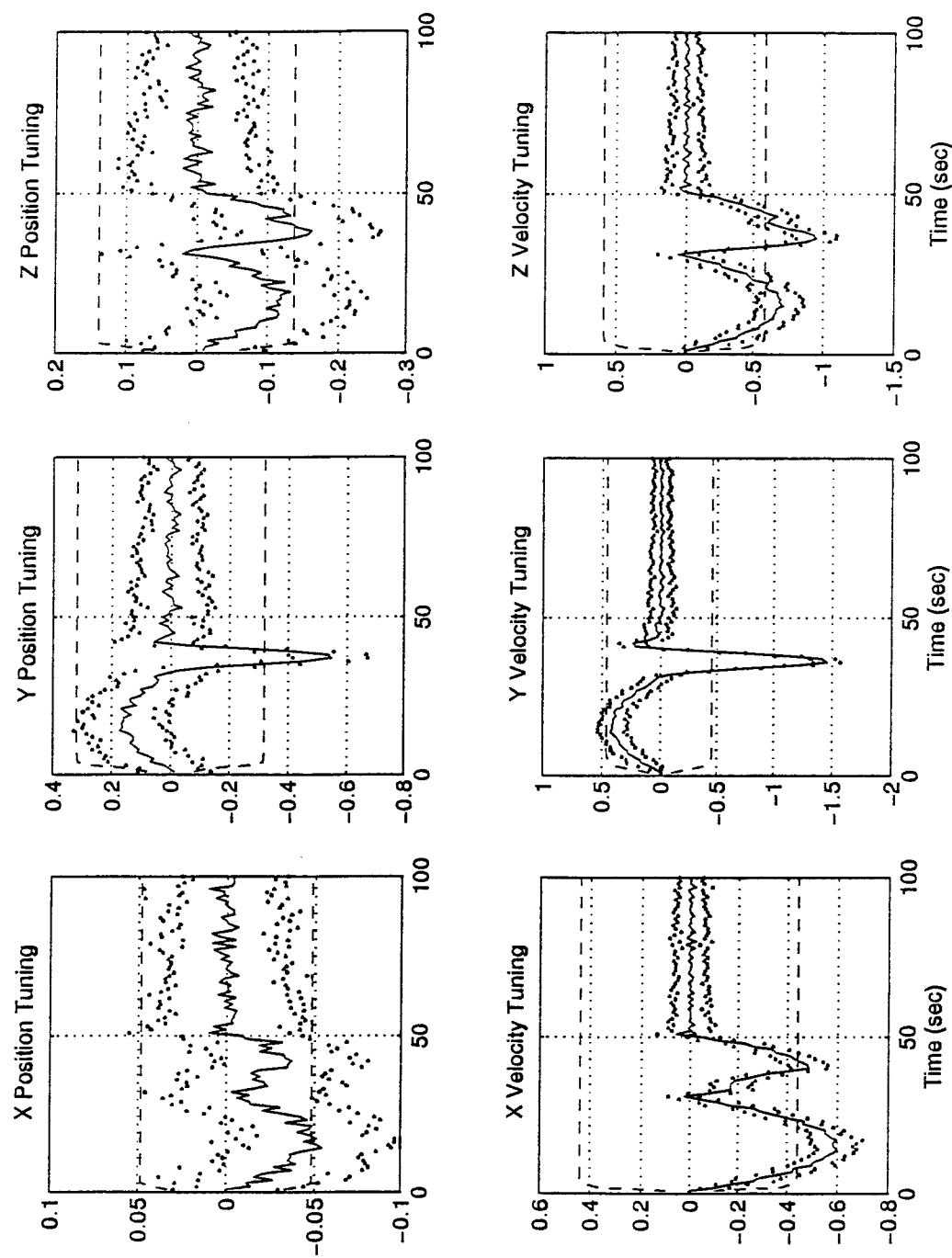


Figure D.6 White Noise at 1 Hz, Improper Model

Kalman Filter

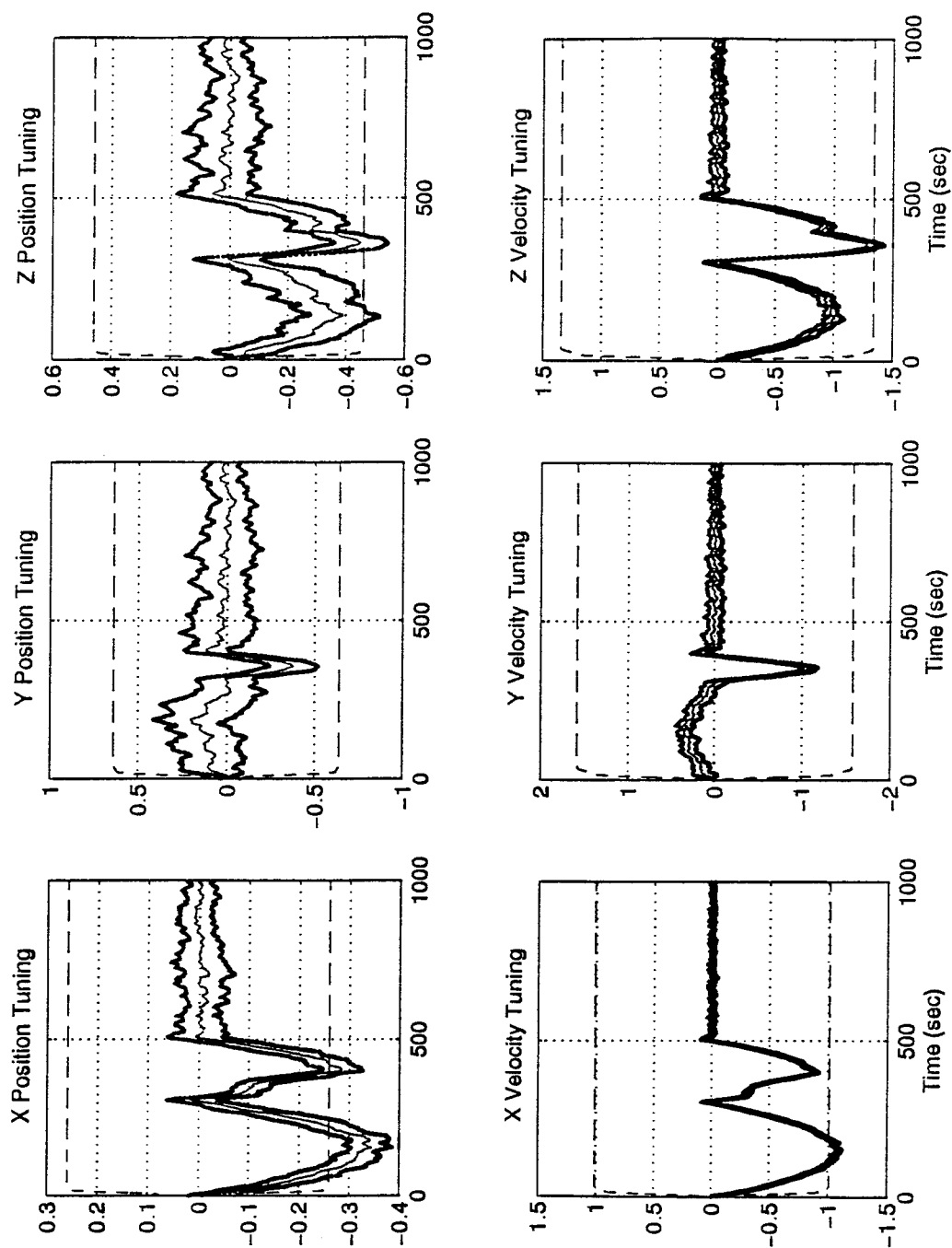


Figure D.7 Colored Noise at 10 Hz, Improper Model

Kalman Filter

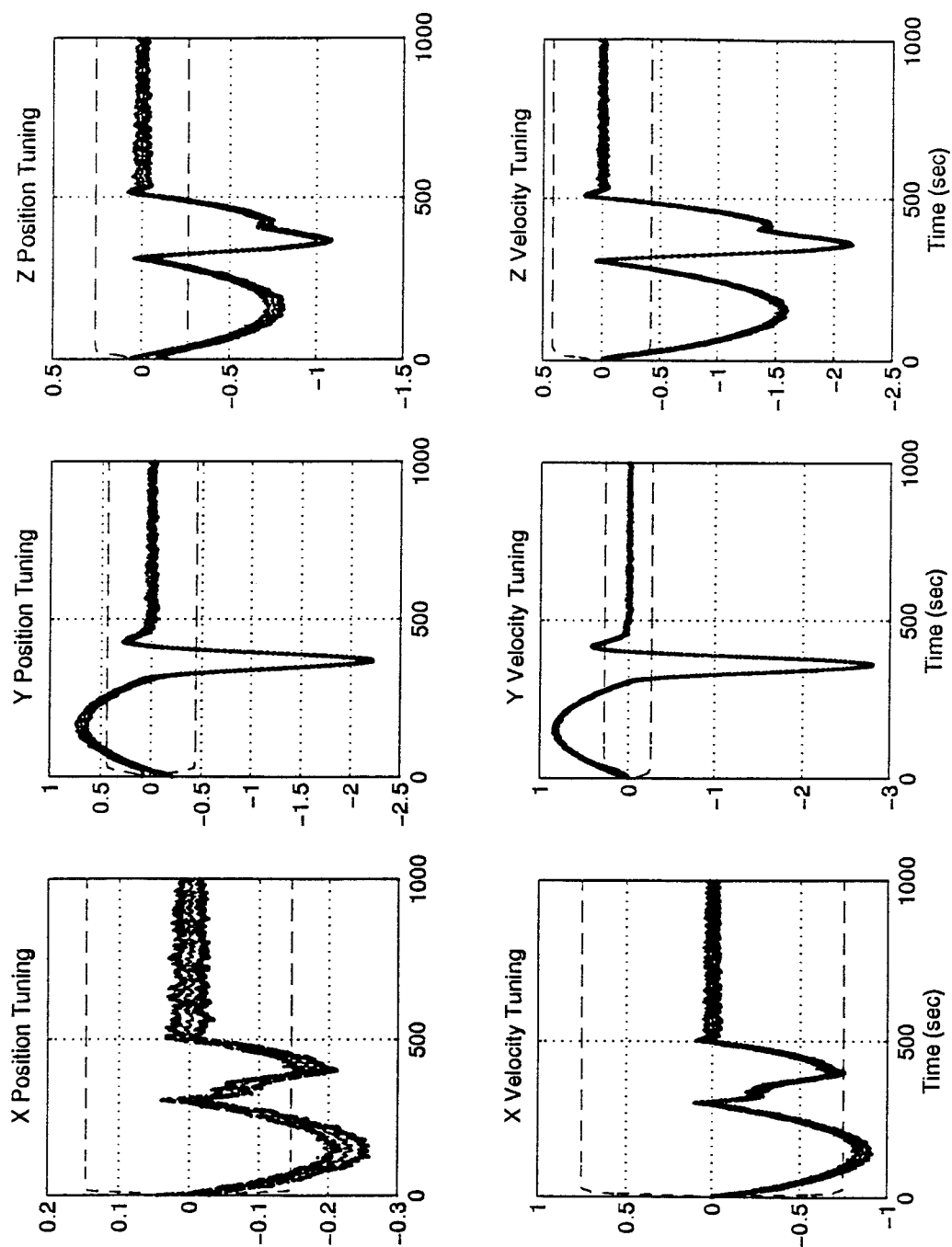


Figure D.8 White Noise at 10 Hz, Improper Model

Bibliography

1. Bach, R. E., Paielli, B. McNally, D. and Warner, David N. "Including Deltarange Measurements in GPS-Aided Navigation Systems," *The Institute of Navigation, National Technical Meeting* (January 1993).
2. Bohenek, Brian J. *The Enhanced Performance of an Integrated Navigation System in a Highly Dynamic Environment*. MS Degree Thesis, AFIT/GE/ENG/94D-01. School of Engineering, Air Force Institute of Technology (AU), Wright-Patterson AFB OH. December 1994.
3. Brown, R. Grover and McBurney, Paul W. "Proper Treatment of the Delta-range Measurement in an Integrated GPS/Inertial System," *The Institute of Navigation, National Technical Meeting* (January 1987).
4. Brown, Alison "Extended Differential GPS," *Global Positioning System*. Papers Published in *Navigation*, Volume IV:107-127, The Institute of Navigation, Alexandria, VA 22314. 1993.
5. Chang, Chaw-Bing and Tabaczynski, John A. "Application of State Estimation to Target Tracking". *IEEE Transactions on Automatic Control*, Volume AC-29, No. 2:98-109. 1984.
6. Beyer, William H. *Standard Mathematical Tables and Formulae, 29th Edition*. Boca Raton, Florida: CRC Press, Inc., 1991.
7. DeFatta, David J. et al. *Digital Signal Processing: A System Design Approach*. New York: John Wiley and Sons, Inc., 1988.
8. Dougherty, John J. and El-Sherief, Hossny and Hohman, David S. "The Use of GPS for Evaluating Inertial Measurement Errors," *Proceedings of the AIAA Guidance, Navigation and Control Conference* (August 1993).
9. Galijan, Randal C. and Gilkey, James Y. "Providing Highly Accurate Velocity Data for an Airborne Platform Using Differential GPS Velocity Corrections from a Non-Surveyed Reference Receiver." *The Institute of Navigation, ION GPS-95* (September 1995).
10. Canadian GPS Associates, *Guide to GPS Positioning*. ISBN: 0-920-114-73-3, Fredericton, New Brunswick: University of New Brunswick Graphic Services, May 1987.
11. Hansen, Neil P. *Incorporation of Carrier Phase Global Positioning System Measurements into the Navigation Reference System for Improved Performance*. MS Degree Thesis, AFIT/GE/ENG/93D-40. School of Engineering, Air Force Institute of Technology (AU), Wright-Patterson AFB OH, December 1993 (AD-A274136).
12. Honeywell Military Avionics. *Honeywell H-764G System Description*. Honeywell Document: 0385-1180. St Petersburg, Florida, May 1995.
13. Hooser, Dr. Mike. "Proposed AFIT Thesis Topic," 746th Guidance Test Squadron, Holloman AFB, NM. Personal Correspondance. 23 December 1994.

14. Hwang, Patrick Y.C. "Kinematic GPS for Differential Positioning: Resolving Integer Ambiguities on the Fly," *Global Positioning System*. Papers Published in *Navigation*, Volume IV:205-219. The Institute of Navigation, Alexandria, VA 22314. 1993.
15. James, M.L. and Smith, G.M. and Wolford, J.C., *Applied Numerical Methods for Digital Computation with FORTRAN and CSMP* New York: Harper & Row Publishers, Inc., 1977.
16. Janes, H.W. and Langley, R.B. and Newby, S.P., "Analysis of Tropospheric Delay Prediction Models: Comparisons with Ray-Tracing and Implications for GPS Relative Positioning", *Bulletin Géodésique*, Volume 65:3, 1991.
17. Kruczynski, L.R., et al, "Global Positioning System Differential Navigation Tests at the Yuma Proving Ground", *Global Positioning System*. Papers Published in *Navigation*, Volume III:160-172, The Institute of Navigation, Alexandria, VA 22314, 1986.
18. Lachapelle, Gerard, M. E. Cannon and G. Lu. "High-Precision GPS Navigation with Emphasis on Carrier Phase Ambiguity Resolution," *Marine Geodesy*, Volume 15. 253-269. 1992.
19. Lachapelle, Gerard. *High Accuracy GPS Positioning: Course Notes*. Arlington, VA: Navtech Seminars, Inc., 1994.
20. Maher, Robert A. "A Comparison of Multichannel, Sequential and Multiplex GPS Receivers for Air Navigation", *Global Positioning System*. Papers Published in *Navigation*, Volume III:3-18, The Institute of Navigation, Alexandria, VA 22314, 1986.
21. Mahmood, Sultan and Simpson, Charles "Integrated DGPS/Inertial TSPI for DOD Ranges:RAJPO Equipment Test Results," *The Institute of Navigation, ION GPS-95* (September 1995).
22. Mathews, John H. *Numerical Methods for Mathematics, Science and Engineering*. Second Edition. New Jersey: Prentice Hall, Inc., 1992.
23. May, Marvin and Nyguen, Khien and Tanju, Bereket "On GPS Velocity," *Proceedings of the Institute of Navigation, 46th National Meeting* June 1989.
24. Maybeck, Peter S. *Stochastic Models, Estimation, and Control*. Volume 1. New York: Academic Press, Inc., 1979.
25. Maybeck, Peter S. *Stochastic Models, Estimation, and Control*. Volume 2. New York: Academic Press, Inc., 1982.
26. Maybeck, Peter S. *Stochastic Models, Estimation, and Control*. Volume 3. New York: Academic Press, Inc., 1982.
27. *MATLAB*. Version 4.2. Computer software. The MathWorks, Inc. 24 Prime Park Way, Natick, MA 01760. March 1994.
28. McGowan, Joseph "Velocity Accuracy Measurement of GPS User Equipment," *AGARD: Advances in Guidance and Control Systems and Technology*, July 1987.
29. Mosie, William B. *Detection, Isolation, and Recovery of Failures in an Integrated Navigation System*. MS Degree Thesis, AFIT/GE/ENG/93D-28. School of Engineering, Air Force Institute of Technology (AU), Wright-Patterson AFB OH, December 1993 (AD-A274056).

30. Moya, David C. and Elchynski, Joseph J. *Evaluations of the World's Smallest Integrated Embedded GPS/INS, the H-764G*. IEEE Position, Location, and Navigation Symposium, 1994.
31. Oppenheim, A.V and Schafer, R.W., *Discrete-Time Signal Processing*, Prentice Hall, Englewood Cliffs, NJ, 1989.
32. Musick, Stanton H. *PROFGEN - A Computer Program for Generating Flight Profiles*. Technical Report, Air Force Avionics Laboratory, Wright-Patterson AFB OH. November 1976. AFAL-TR-76-247, DTIC ADA034993.
33. Nash, Capt Anthony. Project Officer of the CIGTF Advanced Reference System. 746th Guidance Test Squadron, Holloman AFB, NM. Telephone Interview. 7 March 1995.
34. Nash, Capt Anthony. Project Officer of the CIGTF Advanced Reference System. 746th Guidance Test Squadron, Holloman AFB, NM. Electronic Mail, 16 May 1995.
35. Negast, William Joseph. *Incorporation of Differential Global Positioning System Measurements Using an Extended Kalman Filter for Improved Reference System Performance*. MS Degree Thesis. AFIT/GE/ENG/91D-41. School of Engineering, Air Force Institute of Technology (AU), Wright-Patterson AFB OH, December 1991 (AD-A243742).
36. Raquet, Capt. John, et al, "Development and Testing of a Mobile Pseudolite Concept for Precise Positioning," *The Institute of Navigation, ION GPS-95* (September 1995).
37. Robbins, James E. "Reference Trajectories from GPS Methods," *The Institute of Navigation, Technical Meeting*, September 1987.
38. Roecker, J.A. and McGillem, C.D. *IEEE Transactions on Aerospace and Electronic Systems*, Volume 25, No. 6:836-843, 1989.
39. Snodgrass, Capt. Britt and Raquet, Capt. John "The CIGTF High Accuracy Post-Processing Reference System (CHAPS)," *The Institute of Navigation, International Technical Meeting*, (September 1994).
40. Snodgrass, Faron Britt. *Continued Development and Analysis of a New Extended Kalman Filter for the Completely Integrated Reference Instrumentation System (CIRIS)*. MS Thesis, AFIT/GE/ENG/90M-5. School of Engineering, Air Force Institute of Technology (AU), Wright-Patterson AFB OH, March 1990 (AD-A220106).
41. Solomon, Joseph K. *Development of the Extended Kalman Filter for the Advanced Completely Integrated Reference Instrumentation System (CIRIS)*. MS Degree Thesis, AFIT/GE/ENG/89M-08. School of Engineering, Air Force Institute of Technology (AU), Wright-Patterson AFB OH, March 1989 (AD-A206083).
42. Schwartz, K.P., et al. "A Comparison of GPS Kinematic Models for the Determination of Position and Velocity along a Trajectory," *Manuscripta Geodaetica*, 14:345-353, 1989.
43. Stacey, Richard D. *A Navigation Reference System (NRS) Using Global Positioning System (GPS) and Transponder Aiding*. MS Degree Thesis. AFIT/GE/ENG/91M-04. School of Engineering, Air Force Institute of Technology (AU), Wright-Patterson AFB OH. March 1991 (AD-A238890).

44. Tang, Wang, et al. "A Kinematic Carrier Phase Tracking System for High Precision Trajectory Determination," *The Institute of Navigation, ION GPS-94*, (September 1994).
45. Thompson, William J. *Computing for Scientists and Engineers: A Workbook of Analysis, Numerics, and Applications* New York: John Wiley and Sons, Inc., 1992.
46. Tobin, David M. *A Multiple Model Adaptive Tracking Algorithm for a High Energy Laser Weapon System*. MS Degree Thesis, AFIT/GE/ENG/86D-37. School of Engineering, Air Force Institute of Technology (AU), Wright-Patterson AFB OH, December 1986 (AAJ-2510).
47. Vasquez, Juan R. *Detection of Spoofing, Jamming, or Failure of a Global Positioning System (GPS)*. MS Degree Thesis, AFIT/GE/ENG/92D-37. School of Engineering, Air Force Institute of Technology (AU), Wright-Patterson AFB OH, December 1992 (AD-A259023).

Vita

Captain Jeffrey M. Hebert [REDACTED]

[REDACTED] Upon graduation from Grafton Memorial Senior High School in 1986, Jeff enrolled at Worcester Polytechnic Institute (WPI) under an Air Force ROTC scholarship. Jeff received his B.S. with Distinction from WPI and was commissioned into the United States Air Force on 17 May 1990. On 19 May 1991 Jeff reported to Wright Laboratory, Wright-Patterson AFB, Ohio, for his first assignment. Jeff "cut his teeth" at the Control, Integration and Assessment Branch (WL/FIGD) of the Flight Control Division, Flight Dynamics Directorate where he served as an electrical and computer systems engineer. In May of 1994, Jeff entered the Air Force Institute of Technology (AFIT) to pursue a Master of Science in Electrical Engineering (M.S.E.E.) degree, specializing in navigation, guidance and control. Upon graduation from AFIT in December of 1995, Jeff reports to the 746th Test Squadron, Holloman AFB, New Mexico. Jeff is married to the former Catherine Graw of Dayton, Ohio, and has a son, Timothy. Jeff is a member of the Institute of Navigation (ION).

[REDACTED]

VITA-1

REPORT DOCUMENTATION PAGEForm Approved
OMB No. 0704-0188

Public reporting burden for this collection of information is estimated to average 1 hour per response, including the time for reviewing instructions, searching existing data sources, gathering and maintaining the data needed, and completing and reviewing the collection of information. Send comments regarding this burden estimate or any other aspect of this collection of information, including suggestions for reducing this burden, to Washington Headquarters Services, Directorate for Information Operations and Reports, 1215 Jefferson Davis Highway, Suite 1204, Arlington, VA 22202-4302, and to the Office of Management and Budget, Paperwork Reduction Project (0704-0188), Washington, DC 20503.

1. AGENCY USE ONLY (Leave blank)**2. REPORT DATE**
December 1995**3. REPORT TYPE AND DATES COVERED**
Master's Thesis**4. TITLE AND SUBTITLE**
VELOCITY DETERMINATION FOR AN INVERTED
PSEUDOLITE NAVIGATION REFERENCE SYSTEM**5. FUNDING NUMBERS****6. AUTHOR(S)**
Jeffrey M. Hebert**7. PERFORMING ORGANIZATION NAME(S) AND ADDRESS(ES)**
Air Force Institute of Technology, WPAFB OH 45433-6583**8. PERFORMING ORGANIZATION
REPORT NUMBER**
AFIT/GE/ENG/95D-06**9. SPONSORING / MONITORING AGENCY NAME(S) AND ADDRESS(ES)**
746th Test Squadron
1644 Vandergrift Rd.
Holloman AFB, NM 88330-7850**10. SPONSORING / MONITORING
AGENCY REPORT NUMBER****11. SUPPLEMENTARY NOTES****12a. DISTRIBUTION / AVAILABILITY STATEMENT**

Distribution Unlimited

12b. DISTRIBUTION CODE**13. ABSTRACT (Maximum 200 words)****Abstract**

As navigation systems continue to improve in performance and features, the Air Force must develop better Navigation Reference Systems (NRS) to keep pace with technology. Specifically, with the advent of enhanced, integrated Global Positioning System (GPS) and Inertial Navigation System (INS) navigators, emphasis is placed on the measuring performance in the presence of GPS jamming. To meet these needs, a new NRS, dubbed the Sub-Meter Accuracy Reference System (SARS), is being developed by the 746th Test Squadron, Holloman AFB, New Mexico. SARS uses a unique, inverted GPS pseudolite positioning system to determine a reference trajectory. This research investigates two post-processing methods of determining velocity from a discrete position data at a constant data rate. The first method employs numerical differentiation along with digital filters to provide noise reduction. The second method uses kinematic model-based Kalman filtering and smoothing to determine the reference velocity.

14. SUBJECT TERMS
Pseudolite, Velocity, Global Positioning System, GPS,
Navigation Reference System, SARS, Velocity Determination**15. NUMBER OF PAGES**
118**16. PRICE CODE****17. SECURITY CLASSIFICATION
OF REPORT**
UNCLASSIFIED**18. SECURITY CLASSIFICATION
OF THIS PAGE**
UNCLASSIFIED**19. SECURITY CLASSIFICATION
OF ABSTRACT**
UNCLASSIFIED**20. LIMITATION OF ABSTRACT**
UL